Title
Deterministic Magnetization Control by Magnetoelastic Anisotropy and its Dependence on Geometry and Scale

Author
Hockel, Joshua Leon

Publication Date
2013

Peer reviewed|Thesis/dissertation

UNIVERSITY OF CALIFORNIA

Los Angeles

Deterministic Magnetization Control by Magnetoelastic Anisotropy and its Dependence on Geometry and Scale

A dissertation submitted in partial satisfaction of the
requirements for the degree Doctor of Philosophy
in Mechanical Engineering

by

Joshua Leon Hockel

2013

ABSTRACT OF THE DISSERTATION

Deterministic Magnetization Control by Magnetoelastic Anisotropy
and its Dependence on Geometry and Scale

by

Joshua Leon Hockel

Doctor of Philosophy in Mechanical Engineering

University of California, Los Angeles, 2013

Professor Gregory P. Carman, Chair

The recent interest in non-volatile memory and logic devices has encouraged the scientific community to develop improved magnetic control mechanisms. In the present work, the control of magnets by magnetoelastic anisotropy is investigated within the context of magnetoelectric (ME) heterostructures of different geometry and scale. The ME heterostructure is an artificial multiferroic material which exhibits both a coexistence and coupling of ferromagnetic and ferroelectric ordering. This device architecture provides a route to control magnetism with electric fields via interfacial mechanical stress. In the present work, the initial magnetization morphology and behavior under mechanical stress is investigated for bulk laminate composites, thin film heterostructures, patterned single domain nanostructures, and ring shaped nanostructures. Significant differences were observed in the magnets' response to magnetoelastic anisotropy depending on the scale and or geometry of the magnetic material. Generally speaking, as the scale and aspect ratio of a magnetic system is reduced, the intrinsic magnetostatic and shape anisotropy energies are also reduced thus increasing the relative magnitude (and influence) of magnetoelastic anisotropy. The unambiguous control of a magnet's

easy axis is here called *deterministic* control and this is achieved experimentally in single domain and ring shaped magnets. The magnetization of these nanostructures is shown to rotate 90° with an applied electric field, an important proof of concept for the proposed strain-based magnetic writing devices. The experimental results are confirmed by multiple characterization techniques including magnetic force microscopy (MFM), magneto optic Kerr effect (MOKE), photo emission electron microscopy (PEEM), and Lorentz transmission electron microscopy (TEM). This work thus provides significant evidence of the viability of magnetoelastic anisotropy as a means to control magnetoelectric heterostructures in future spintronic device research.

The dissertation of Joshua Leon Hockel is approved.

Christopher S. Lynch

Kang L. Wang

Pei-Yu Chiou

Gregory P. Carman, Committee chair

University of California, Los Angeles

2013

For my parents,

George and Kimiko Hockel

TABLE OF CONTENTS

TABLE OF FIGURES

VITA

Education

2011	M.S. - Mechanical Engineering *University of California, Los Angeles*
2009	B.S. - Mechanical Engineering *University of California, Riverside*

Employment history

2009-2013	Graduate Student Researcher Active Materials Lab *University of California, Los Angeles*
2006-2009	Engineer Performance Assessment Department *Naval Surface Warfare Center, Corona CA*

Publications and conference presentations

Joshua L. Hockel, Shawn Pollard, Tao Wu, Kyle Wetzlar, Yimei Zhu, and Gregory P. Carman, "Electrically Controlled Reversible and Hysteretic Magnetic Domain Evolution in Nickel Film/ $Pb(Mg_{1/3}Nb_{2/3})O_3]_{0.68}$-$[PbTiO_3]_{0.32}$ (011) Heterostructure" APPLIED PHYSICS LETTERS, accepted (2013)

Hyungsuk K.D. Kim, Laura T. Schelhas, Scott Keller, **Joshua L. Hockel**, Sarah H. Tolbert, and Gregory P. Carman, "Magnetoelectric Control of Superparamagnetism", NANOLETTERS 13, 3 (2013)

M. Buzzi, R.V. Chopdekar, **J. L. Hockel**, A. Bur, T. Wu, N. Pilet, P. Warnicke, G. P. Carman, L. J. Heyderman, and F. Nolting, "Single Domain Spin Manipulation by Electric Fields in Strain Coupled Artificial Multiferroic Nanostructures" PHYSICAL REVIEW LETTERS 111, 027204 (2013)

Joshua L. Hockel, Kin Wong, Pedram Khalili, Juan Alzate, Kang Wang, and Gregory P. Carman, "90-Degree Bistable Switching and Barrier Energy Control in Single Domain Magnetoelectric Nickel/PMNPT heterostructures", The 12th Joint MMM-Intermag Conference, Jan 14-18 2013, Chicago, Illinois, USA

Joshua L. Hockel, Alexandre Bur, Tao Wu, Kyle P. Wetzlar, and Gregory P. Carman, "Electric field induced magnetization rotation in patterned Ni ring/Pb(Mg1/3Nb2/3)O3](120.32)-[PbTiO3]0.32 heterostructures" APPLIED PHYSICS LETTERS 100, 022401 (2012)

Chin-Jui Hsu, **Joshua L. Hockel**, and Gregory P. Carman, "Magnetoelectric manipulation of domain wall configuration in thin film Ni/[Pb(Mn1/3Nb2/3)O3]0.68-[PbTiO3]0.32 (001) heterostructure" APPLIED PHYSICS LETTERS 100, 092902 (2012)

Joshua L. Hockel, Tao Wu, Alexandre Bur, Kyle Wetzlar, and Gregory P. Carman, "Nanoscale Magnetoelectric Motor", IEEE Magnetics Summer School, Jul 22-27 2012, Chennai, India

Mingqiang Bao, Guodong Zhu, Kin L. Wong, **Joshua L. Hockel**, Mark Lewis, Jing Zhao, Tao Wu, Pedram Khalili Amiri, and Kang L. Wang, "Magneto-electric tuning of the phase of propagating spin waves" APPLIED PHYSICS LETTERS 101, 022409 (2012)

J. G. Alzate, P. Upadhyaya, M. Lewis, J. Nath, Y. T. Lin, K. Wong, S. Cherepov, P. Khalili Amiri, K. L. Wang, **J. L. Hockel**, G. P. Carman, *UCLA;* J. Zhu, Y-J Chen, I. N. Krivorotov**, "**Spin Wave Nanofabric Update" IEEE/ACM International Symposium on Nanoscale Architectures (NANOARCH 2012), Jul 4-6, 2012 Amsterdam, The Netherlands

Guodong Zhu, Kin. L. Wong, J. Zhao, Pedram K. Amiri, Kang L. Wang, **Joshua L. Hockel**, Gregory P. Carman, J. Zhu, and I. Krivorotov, "The influence of in-plane ferroelectric crystal orientation on electrical modulation of magnetic properties in Co60Fe20B20/SiO2/(011) xPb(Mg1/3Nb2/3)O3-(12x)PbTiO3 heterostructures" JOURNAL OF APPLIED PHYSICS 112, 033916 (2012)

Joshua L. Hockel, Alexandre Bur, Tao Wu, Kyle Wetzlar, Chin-Jui Hsu, Hyungsuk Kim, and Gregory P. Carman, "Planar Magnetization Control in Patterned Nanostructures" The 56th Conference on Magnets and Magnetic Materials (IEEE MMM) Oct 30-Nov 3 2011, Scottsdale, Arizona, USA

S. Cherepov, P. Khalili Amirir, J.G. Alzate, K. Wong, M. Lewis, P. Upadhyayam J. Nath, M. Bao, **J. L. Hockel**, A.T. Wu, G.P. Carman, A. Khitun, and K.L. Wang, "Electric Field Induced Spin Wave Generation Using Multiferroic Magnetoelectric Cells" The 56th Conference on Magnets and Magnetic Materials (IEEE MMM) Oct 30-Nov 3 2011, Scottsdale, Arizona, USA

Alexandre Bur, Tao Wu, **Joshua L. Hockel**, Chin-Jui Hsu, Hyungsuk K. D. Kim, Tien-Kan Chung, Kin Wong, Kang L. Wang, and Gregory P. Carman, "Strain-induced magnetization change in patterned ferromagnetic nickel Nanostructures" JOURNAL OF APPLIED PHYSICS 109, 123903 (2011)

Tao Wu, Alexandre Bur, **Joshua L. Hockel**, Kin Wong, Tien-Kan Chung, and Gregory P. Carman, "Electrical and Mechanical Manipulation of Ferromagnetic Properties in Polycrystalline Nickel Thin Film" IEEE MAGNETICS LETTERS, Volume 2 (2011)

Tao Wu, Alexandre Bur, Kin Wong, **Joshua L. Hockel**, Chin-Jui Hsu, Hyungsuk K. D. Kim, Kang L. Wang, and Gregory P. Carman, "Electric-poling-induced magnetic anisotropy and electric-field-induced magnetization reorientation in magnetoelectric Ni/(011) [Pb(Mg1/3Nb2/3)O3](1-x)-[PbTiO3]x heterostructure" JOURNAL OF APPLIED PHYSICS 109, 07D732 (2011)

Tao Wu ,Ping Zhao, Mingqiang Bao, Alexandre Bur, **Joshua L. Hockel**, Kin Wong, Kotekar P. Mohanchandra, Christopher S. Lynch, and Gregory P. Carman, "Domain engineered switchable strain states in ferroelectric (011) [Pb(Mg1/3Nb2/3)O3](12x)-[PbTiO3]x (PMN-PT, x_0.32) single crystals" JOURNAL OF APPLIED PHYSICS 109, 124101 (2011)

Joshua L. Hockel, Tao Wu, and Gregory P. Carman, "Voltage bias influence on the converse magnetoelectric effect of PZT/terfenol-D/PZT laminates" JOURNAL OF APPLIED PHYSICS 109, 064106 (2011)

Joshua L. Hockel, Tao Wu, and Gregory P. Carman, "Influence of DC Voltage Bias on the Converse Magnetoelectric Effect Response in PZT/Terfenol-D/PZT Laminate Composites" ASME 2010 Conference on Smart Materials, Adaptive Structures and Intelligent Systems, Sept 28–Oct 1, 2010, Philadelphia, Pennsylvania, USA

Chapter 1: INTRODUCTION

1.1 Future magnetic devices

Magnetic materials and devices are fundamental components of modern computer hardware and thus our everyday lives. While some magnetic technologies are already quite familiar such as the hard disk drive (HDD), the future portends many new and exotic applications of magnetic phenomena. Recently,[1,2] researchers have proposed a new type of random access memory (RAM) based on magnetic materials, where the bit information is stored in magnetization rather than capacitive charge or metal oxide semiconductor field effect transistors (MOSFET) as in traditional SRAM and DRAM. The key advantage of this *magnetic* RAM (MRAM) technology is that the information is recorded in the intrinsic magnetization of the material and is thus *non-volatile*. Since much of the energy consumption in traditional RAM devices is exhausted to refresh the lost charge from leakage currents, it's not hard to imagine new MRAM devices that use only a fraction of the energy of traditional devices. The steady interest in MRAM research is certainly fueled by the recent demand for mobile devices and the need for low-power memory components. Advancements in MRAM research are made possible by a holistic interpretation of magnetism's many dependent energies. For example, the dependence of magnetization behavior on mechanical stress has been recently studied for applications in *magnetoelectric* random access memory (ME-RAM.)[3,4,5] Here the magnetic material is viewed not as a fixed material property but as an actively controllable device (i.e. through applied electric field or mechanical stress). Many researchers today are taking advantage of this active view of magnetism, leading to new and exciting designs for voltage and mechanically controlled memory, antennas, and sensors, just to name a few.

1.2 Note regarding structure of this work

This work is divided into 7 chapters organized by theme. Chapter 1 provides an overview of concepts relevant to magnetic materials and magnetoelastic control. In addition, the characterization and fabrication techniques used in this work are introduced which will help contextualizing the results in the following chapters. Chapters 2, 3, 4, and 5 examine magnetoelastic control in bulk/macro scale magnetoelectric laminates, thin film heterostructures, single domain nanomagnets, and ring-shaped nanomagnets, respectively. Each chapter begins with a discussion of related phenomena and the current research progress from the literature. Each chapter contains one or more experimental works related to the theme of the chapter, and each experimental work contains its own set of introductions and conclusions. The chapter themes are ordered such that the magnetostatic energy in each successive chapter is reduced by a reduction in either scale or shape anisotropy. Chapter 6 summarizes some of the overarching themes in this work and Chapter 7 is a list of referenced work.

1.3 Strain coupled magnetoelectric effect

Magnetic behavior is dependent on many external inputs including but not limited to thermal energy, electric potential, and mechanical energy. Research continues to advance in all areas of magnetic control; however some control mechanisms may be more interesting than others from a device standpoint. In the previously mentioned example of ME-RAM, rapid magnetic writing is accomplished by electrically generated mechanical stress from a ferroelectric. This electric field device structure may offer a technical advantage over other proposed methods which rely on magnetic induction through wires. As shown in Table 1 is a comparison of current and proposed RAM devices, including ME-RAM. Note the excessive energy consumption of the inductive magnetic field based approach in standard MRAM. By comparison, the popular SRAM

platform clearly offers significant advantages in writing and reading speed and energy due to the well-developed MOSFET technology. However, the attractive feature of ME-RAM is its best-in-class write energy of .16 fJ, due in part to the scaling effect of electric fields and the efficiency of strain mediated magnetoelectric transduction. This significant reduction in write energy may offer key advantages, especially for mobile device applications, and may be a driving factor for continuing ME-RAM research. In summary, if we consider just the energy and switching speed specifications of the various devices, ME-RAM stands out by offering substantial advantages over traditional devices. However, successful development of ME-RAM will require a complete understanding of the role of interfacial mechanical stress in magnets. Unfortunately, many aspects of this *magnetoelastic* behavior remain unknown and undemonstrated, such as its dependence on device geometry, domain structure, and especially scale.

Table 1: Comparison of proposed RAM technologies

	SRAM	MRAM	STT-RAM	ME-RAM
Write time (ns)	1	20	3-10	1-10
Read time (ns)	1	10	10	1-10
Energy/bit (fJ)	100	70,000	100	.16
Non-Volatile?	No (leakage)	Yes	Yes	Yes

Data adopted from J.-M. Hu *et al.* N. Comms. **533** (2011) 1564 and
K.L. Wang *et al.* J. Phys. D: Appl. Phys. **46** (2013) 074003

1.3 Magnetization, magnetoelasticity and scale

Before we can understand the role of mechanical stress in magnets at different scales (i.e. macro or bulk scale, thin film, and nanostructures,) we must first study the *emergent* magnetic properties that come from scaling. We may expect magnetic materials to behave very differently at different scales due to magnetostatics and the tendency of magnetic materials to form

morphologies with flux closure. As we alter the geometry or scale of the magnetic material, we can expect the balance of magnetic anisotropies and magnetostatics to shift leading to unique magnetic behavior and perhaps unique magnetoelastic coupling behavior as well. A well known example of this magnetic scaling behavior is the single domain magnet which represents a domination of magnetostatic shape anisotropy over other magnetic anisotropies and typically develops below a critical dimension of about 500nm. As shown in Figure 1, bulk magnets are composed of multiple magnetic *domains*, which can be broken down further into groups of the aforementioned single domains. Analytical models exist to predict the occurrence and behavior of these single domain nanomagnets under mechanical load[6], however detailed experimental data of small-scale magnetoelasticity remains nonexistent. Indeed, an experimental study of magnetoelastic effects spanning magnetic devices of *all scales* has never been carried out. A study of this scope may reveal new information about the efficacy of mechanically controlled magnetism as a function of scale, and may even yield new devices based on these principles. Therefore, the scope of the present work must encompass all device scales with a goal of identifying unique attributes of magnetoelastic effects at each scale. In addition, the present work will develop techniques to achieve unambiguous (i.e. deterministic) control of magnetization in magnetic devices by magnetoelastic means.

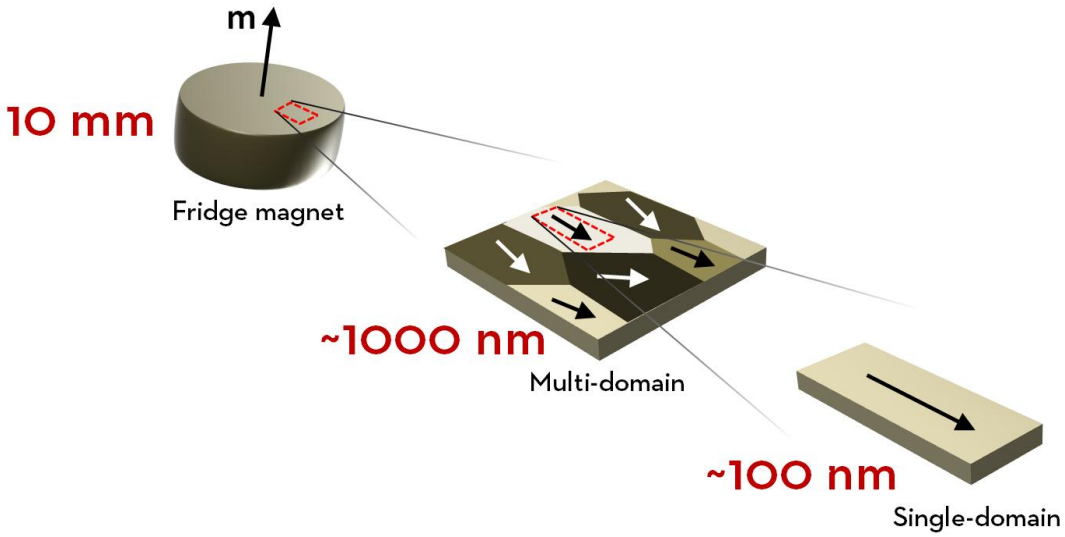

Figure 1: Schematic of magnetic structure with decreasing geometry. Listed size regimes are approximate and the magnetization directions are only illustrative.

While even small mechanical perturbations of magnetism are of technological interest, a complete and *deterministic* control of magnetization is ultimately desired. By deterministic control we mean the direction and rotation of the magnetization and magnetic domain walls may be predictably and repetitively controlled. This presents a challenge as many competing magnetic energies complicate these systems and may only simplify at the nanoscale. As shown in Figure 2, we may think of magnetic devices as a continuum of decreasing size and progressively improving deterministic magnetization control. At the macro or *bulk* scale, competing domains and complex magnetocrystalline energy presents an impediment toward complete magnetization control. For one, the magnitude of energy available by magnetoelastic means is simply insufficient to achieve deterministic control although magnetization process can still be modified as will be shown later. If we then take the bulk material and reduce its thickness to the nanoscale then we would obtain a *thin film*. These films may contain multiple magnetic domains, however we may eliminate some energies such as magnetocrystalline anisotropy

through a variety of fabrication techniques. Also, the magnetization of thin films is confined by magnetostatics and geometry to lie in-plane leading to an improvement in deterministic control. Still, domain walls within thin films often form along imperfections in the film, and controlling the location and density of these imperfections is a challenge. Continuing on to smaller structures, if we pattern the thin film and shape individual *islands* of material on the micron scale then we may obtain multidomain or single domain elements with stable and predictable magnetizations determined by shape-induced anisotropy. However, controlling such magnets by magnetoelastic means may still be improbable due to insufficient mechanical energy. Fortunately, through careful design of the magnet geometry we may achieve structures with very low magnetic shape anisotropy. Such structures may be controlled deterministically by magnetoelastic means, and this is an ongoing pursuit of magnetic device research and a goal of the present work.

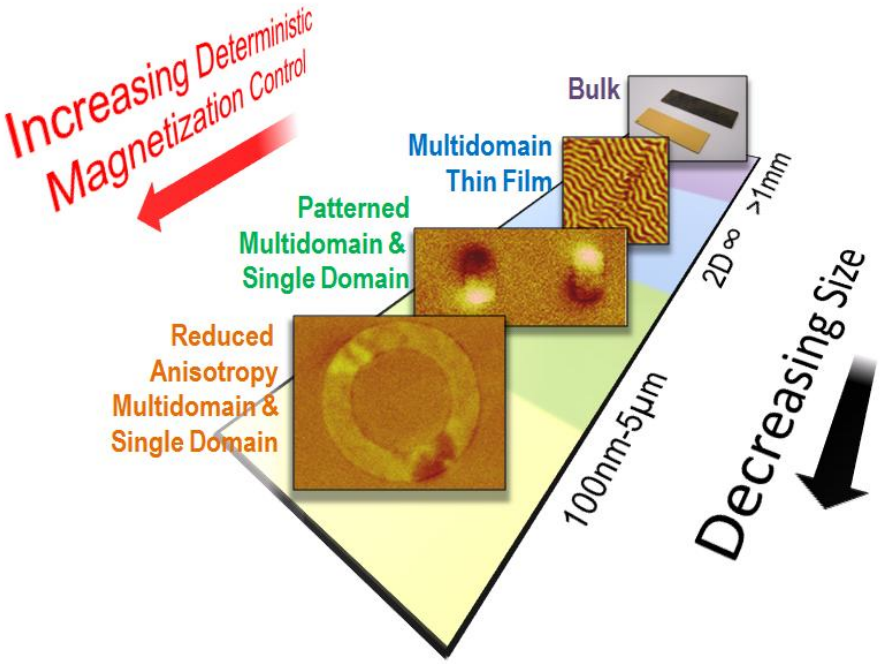

Figure 2: Trend of increasing deterministic magnetization control with decreasing feature size and anisotropy. Size regimes are approximate

1.4 Magnetoelastic anisotropy

Magnetism occurs when atoms with unpaired spin orbitals are bound to a crystal lattice. Asymmetry in the spin-orbit coupling interacting with the local crystalline electric field results in magnetic anisotropy such as magnetocrystalline anisotropy. Certain directions within the material magnetize easier than others, and this preference is strongly correlated to the crystal lattice. From this viewpoint, a modification of the crystal lattice by mechanical stress necessitates a change in the magnetic easy axis. The magneto-mechanical coupling described in this manner is called *magnetoelasticity* or the *Inverse Villari effect*. Described as energy, the directional variance in magnetic properties in response to a mechanical stress is called *magnetoelastic anisotropy*[7]. It should be noted that only a handful of magnetic materials express magnetoelasticity in useful magnitudes. This is because the magnitude of expressed magnetoelasticity is related to the asymmetry of the spin-orbit coupling and the relative strength of other magnetic anisotropies, such as magnetocrystalline anisotropy, which may lock the magnetization and hinder magnetoelastic coupling. Describing or modeling magnetoelastic response can be challenging given the diversity of magnetic materials and the complexity of the spin-orbit-crystal lattice interactions. Harder still, at the macroscale magnetic materials are composed of many millions of magnetic *domains*, or regions of uniform magnetization. Fortunately for magnetic researchers, relatively simple models have been developed to describe the cumulative behavior of these multi-domain materials under mechanical load. What follows is the multidomain model of magnetoelasticity and it will be useful for describing experiments on bulk magnetoelectric laminates which will be described later in this work.

The following multi-domain model predicts the average magnetization behavior of multiple domains under magnetoelastic anisotropy. This is useful for describing the general magnetization preference of bulk or multidomain systems. More interestingly, the “rules of

thumb" guiding magnetoelasticity which are illustrated here will make more complex systems easier to predict and visualize. Let's consider a representative multidomain (MD) model[8] of a negative magnetostrictive material (such as Nickel) consisting of four domains arranged in head-to-tail flux closure. The magnetization behavior (magnetization (M) vs. applied field (H) response) of this MD system may look something like Figure 3A, with an initially high permeability which decreases toward saturation. If we then apply a compressive stress the model takes on the form of Figure 3B. Now the M-H behavior may appear like Figure 3B, with a higher initial permeability in response to the applied mechanical load. Magnetoelastic anisotropy is added to the system leading to increased magnetization tendency parallel to the applied strain. In this instance, magnetization is completed with less applied field than in the initial case, so a convenient label for this improved response is called *easy*. In this example, the material is called *negative magnetostrictive* because a compressive (negative-sign) load causes magnetization increase along the applied direction. We observe the opposite effect in Figure 3C where a tensile stress is applied to the same negative magnetostrictive material. This time the M-H behavior shows a gradual magnetization response with initially lower permeability. This response is called *hard because* of the larger field required for magnetization. This simple interpretation of the magneto-mechanical interaction is useful for predicting average magnetization preference over large samples and can even provide a rough estimation of spin preference in nanostructures.

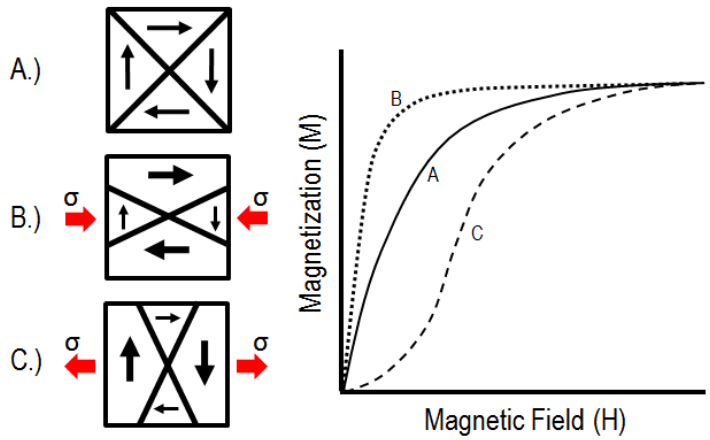

Figure 3: Magnetization behavior of a negative magnetostrictive material as a function of applied mechanical stress, σ. At left are the loading schemes and at right are the corresponding magnetization trends (M-H curves). A. No applied load. B. Applied compressive stress resulting in increased magnetization preference (easy). C. Applied tensile stress resulting in reduced magnetization preference (hard).

1.5 Quantifying magnetoelastic anisotropy

It was shown in the previous section that magnetoelastic anisotropy may be included in the energy formulation for single domain particles. The magnetic behavior in response to magnetoelasticity depends on the initial magnetization direction. Thus the phenomenological expression of magnetoelastic anisotropy must couple mechanical stress and magnetic anisotropy with respect to the direction cosines of the magnetization. The magnetoelastic anisotropy as a function of applied mechanical strain is thus

$$E_{ME}(\alpha_i, \varepsilon_{ij}) = B_1\left[\varepsilon_{xx}\left(\alpha_1^2 - \frac{1}{3}\right) + \varepsilon_{yy}\left(\alpha_2^2 - \frac{1}{3}\right) + \varepsilon_{zz}\left(\alpha_3^2 - \frac{1}{3}\right)\right] + B_2\left[\varepsilon_{xy}\alpha_1\alpha_2 + \varepsilon_{yz}\alpha_2\alpha_3 + \varepsilon_{zx}\alpha_3\alpha_1\right]$$

where B_1 and B_2 are the first and second order magnetoelastic coupling coefficients, respectively, where $B_{ij}=c_{ijkl}\lambda_{kl}$, though for the polycrystalline case bulk values may be used[7]. For most of the discussions in the present work only normal stresses will be considered. In addition, if we

assume the case of anisotropic in-plane loading with $\varepsilon_{zz}=0$ and if we restrict the magnetization to rotate in-plane then the magnetoelastic anisotropy reduces to

$$E_{ME} = K_{ME}(1-\alpha_2^2), \text{ where } K_{ME} = \frac{3}{2}\lambda_s E(\varepsilon_{yy} - \varepsilon_{xx})$$

This is the most frequently encountered form of the K_{ME} formulation as it describes the common case of biaxially loaded structures magnetized in-plane. Here, E is the Young's or stiffness modulus and λ_s is the saturation magnetostriction for the polycrystalline material. Note that the only relevant strain terms in this reduced form of K_{ME} are ε_{yy} and ε_{xx}; the strain anisotropy is the difference between them.

1.6 Magnetostriction

Just as magnetization can be manipulated by magnetoelastic anisotropy, so can magnetostriction behavior, denoted as λ. As stated earlier, magnetization and magnetostriction response are directly related, though the magnitude and sign of the lattice strain upon magnetization depends on the material. When a magnetic field is applied to a magnetic material, the magnetization will rotate to minimize the Zeeman potential. Interestingly, the crystal lattice of the material sometimes deforms from its normal state in an effort to minimize this Zeeman potential, an effect we observe as magnetostriction. We study magnetostriction ability because it provides information about the magneto-mechanical coupling efficiency. One measure of this coupling efficiency is the *piezomagnetic coefficient*, $d\lambda/dH$ but also expressed in the inverse case as $dB/d\varepsilon$. In coupled magnetoelastic systems where the goal is to maximize magnetic or mechanical output a large piezomagnetic coefficient is desired. Since a material's ability to respond to strain or magnetic field is critical to the piezomagnetic coefficient, we must look

closer at the origin of magnetostriction and how it can be maximized by magnetoelastic anisotropy.

Let us imagine that magnetic materials are made of elliptical magnetic domains, displayed in Figure 4 as ellipses with their magnetizations lying parallel to the long axis[8]. A real magnetic material may be made up of millions of such domains and the total field-induced length change (i.e. magnetostriction) of the magnetic material is thus a function of domain rotation and alignment. A completely reversing 180 degree domain structure in Figure 4A does not change the total length of the macro material because the total length of domains has not changed. If we then apply a stress as in Figure 4B, the domains may rotate 90 degrees in response to the magnetoelastic anisotropy and the total length of the domains is decreased. Now when a field is applied, the domains rotate 90 degrees to align with the field and the total length of the material increases significantly. These *non-180 degree* domain rotations increase the magnetostriction response of the material and are made possible by the magnetoelastic anisotropy. This magnetoelastic anisotropy-dependent magnetostriction behavior is important for strain-coupled magnetic systems such as the ME-RAM mentioned earlier. The magnitude of magnetostriction depends on the material composition because magnetoelasticity is closely related to magnetocrystalline anisotropy and thus chemistry and crystal structure. In Table 2 is list of selected magnetostrictive materials and their relevant magnetoelastic properties. A quick way to compare the magnetoelastic potential of materials is to look at the first order magnetoelastic coupling coefficient, B_1 which was mentioned in the previous section. A recurring challenge of magnetoelastic researchers is the need for new material systems with improved magnetostriction properties. Often a new set of fabrication techniques must be developed in order to create materials with unique chemical compositions, such as in Terfenol-D ($Tb_{.3}Dy_{.7}Fe_{1.9}$.) It should be

noted that nickel was used in many of the experiments in this work not because it had exceptional magnetostrictive properties but because it is an easy material to fabricate with.

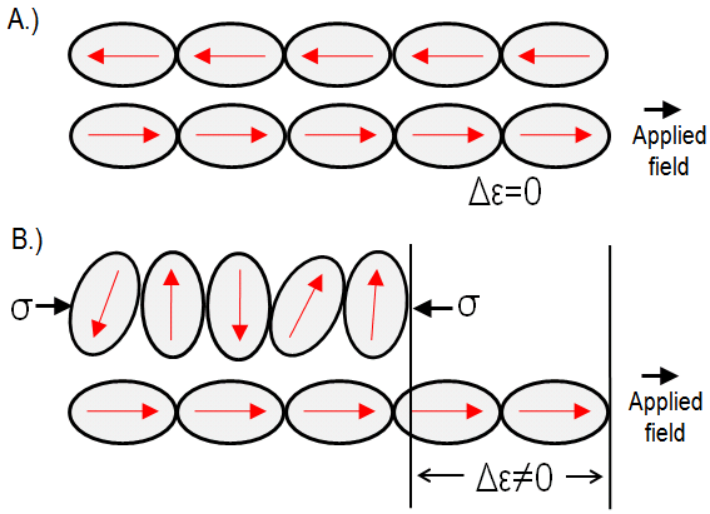

Figure 4: Magnetostriction behavior of a magnetostrictive material under applied compressive mechanical stress. A. 180 domain rotation results in zero net magnetostrictive strain. B. Applied load increases prevalence of non-180 degree domain rotation. When magnetic field is applied the net magnetostriction is non-zero.

Table 2: Selected magnetostrictive materials and magnetoelastic properties

	λ_s (με, ppm)	M_s (emu cm^{-3})	Stiffness (GPa)	B_1 (MJ m^{-3})
$Fe_{81}Si_{13.5}B_{3.5}C_2$ (Metglas)	40	865	120	4.8
$Tb_{.3}Dy_{.7}Fe_{1.9}$ (Terfenol-D)	1200	800	35	42
$Co_{43}Fe_{43}B_{14}$	120	1433	160	19.2
$Co_{60}Fe_{20}B_{20}$	50	1200	160	8
$CoFe_2O_4$	-110	500	150	-16.5
$Ga_{19}Fe_{81}$ (Galfenol)	250	1300	60	15
$Ni_{55}Fe_{45}$ (Permalloy)	27	1273	205	5.5
Ni	-34	485	200	-6.2
Co	-62	1440	209	-13
Fe	-7	1707	211	-2.9

1.7 Fabrication techniques

Many micro-fabrication techniques have been developed over the last few decades, driven by integrated circuit manufacturers as well as micro electromechanical systems (MEMS) research. Most device fabrication procedures involve a serial process of lithography, metal deposition, and etching. The most common lithography process uses UV light and glass masks, but more advanced techniques with higher resolution exist, such as e-beam lithography. While optical lithography techniques are easier and cheaper than e-beam lithography, optical techniques are diffraction limited and thus only structures larger than 1 micron can be reliably made. In this work, structures as small as 100 nm are desired, with geometry tolerances less than 10nm. All devices are thus fabricated in the e-beam lithography and lift-off process, which is described in this section. A diagram of the workflow is shown in Figure 5. In the first step, a photosensitive polymer resist (e.g. PMMA, AZ series) is spin coated onto a silicon or piezoelectric substrate. This resist is soft baked to partially bake off some of the solvent and harden the resin. In the second step, the resist is patterned in the shape of the desired structures. This is done with an e-beam writing system, which can focus a beam of electrons with sub 10 nm precision. As electrons interact with the resist, a photosensitive chemical within the resist breaks down. The patterned resist is then placed in a developer solution (MIBK) which causes the written areas of the resist to dissolve away, forming a cavity in the shape of the desired feature as in Figure 5-2. In step 3, metal is placed in the cavity of the resist either by metal sputtering, metal evaporation, or a chemical method such as CVD or electroplating. In the case of sub micron features it is desired to have anisotropic metal deposition, so metal evaporation is used most often. As shown in Figure 5 step 3, metal now fills the pattern cavity but does not conformally coat the cavity side walls (as would be the case with sputter deposition.) It should be noted that metal deposition with e-beam evaporation limits the material being deposited to elementally pure materials. In

other words, some of the exotic materials listed in Table 2 cannot be accessed at the present time. Finally, in step 4 the resist is removed by dissolving it completely in a bath of acetone. Metal which was deposited on top of the resist is removed along with the resist, (this was the reason for wanting an anisotropic metal deposition step.) Only the desired nanostructures remain on the substrate surface as shown in Figure 5 step 4. The e-beam lithography process is versatile and precise, but because it is a serial writing process samples are expensive and only a small area of structures can be patterned.

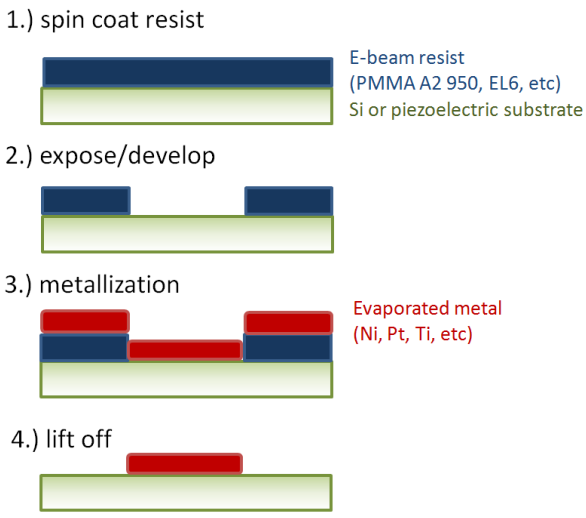

Figure 5: E-beam lithography and lift-off fabrication process flow for nanostructures.

1.8 Magnetic characterization techniques

1.8.1 MFM

Magnetic Force Microscopy (MFM) is a scanning probe technique to measure surface topography of samples with sub-nm precision. The MFM consists of a sharp (~50nm wide) silicon tip which held in a piezoelectric scanning holder. A laser beam reflects off the scanning tip to a detector which records the amplitude of the reflected signal. The tip is scanned over the surface of the sample while physically oscillated at resonance (i.e. tapping mode) to maximize

the sensitivity of the tip to topographic perturbations. As the tip scans over the sample surface, topography is recorded and plotted to generate a 3-dimensional image of the sample surface. This initial tapping mode pass is shown schematically in Figure 6a. Special functionalized tips are also produced, such as a magnetic tip which includes a thin film coating of Co or other magnetic material. After the initial tapping mode procedure, the tip is scanned over the sample once again at a user-defined height offset (i.e. lift mode) to allow the sample to interact magnetostatically with the sample. Magnetostatic tip-sample interactions are detected as a shift in the signal phase and can, like topography, be plotted to create a magnetic topography of the sample as shown in Figure 6b. The MFM approach is an extremely useful technique as it is simple to use and relatively inexpensive. Still, the technique suffers from drawbacks such as magnetic manipulation of the sample by the tip, which could result in an inaccurate measurement. The MFM technique suffers from poor planar resolution due to the physical dimensions of the scanning tip itself (i.e. tip effect). Nevertheless, MFM remains the first go-to approach for initial magnetization characterization needs.

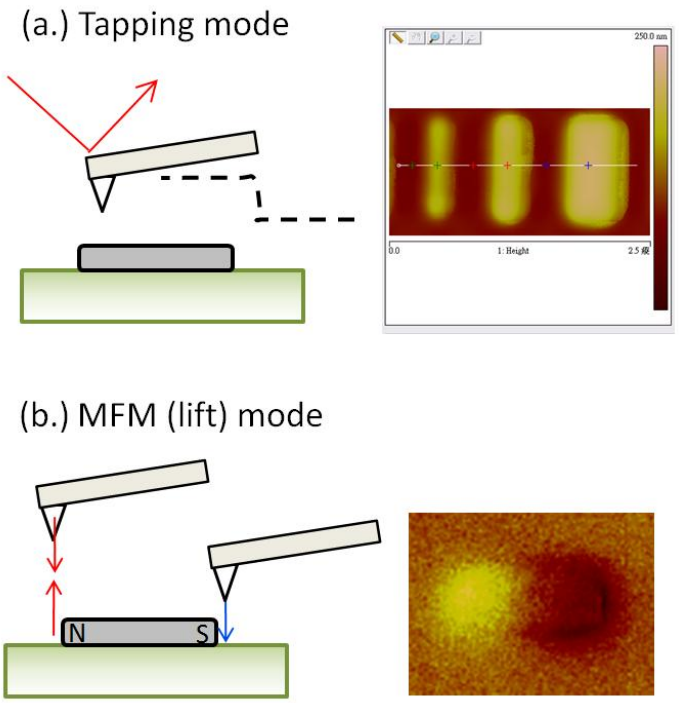

Figure 6: Comparison and examples of two scanning probe techniques. (a.) Atomic Force Microscopy (AFM) in the tapping mode and (b.) Magnetic Force Microscopy (MFM) in the lift mode

1.8.2 MOKE

Perhaps the most versatile of all magnetic characterization techniques is the Magneto-Optical Kerr Effect technique, or simply MOKE. In this technique, the sample (usually a thin reflective film) is placed in a magnetic field bias which is varied in time between large negative and positive field values. Meanwhile, a circularly polarized laser beam is reflected off the sample and onto a photo-detector. Upon reflecting off the sample, the circularly polarized light will interact with the native magnetization of the film, causing it to be elliptically polarized and rotated (i.e. the Kerr effect.) High Kerr rotation corresponds to parallel alignment between the magnetization and the laser beam. The relative change in ellipticity and light intensity as a function of applied magnetic field can be thus used to infer the magnetization of the film and generate *hysteresis plots*. Shown in Figure 7 is a hysteresis plot of the relative magnetization

change of a 200nm Terfenol-D ($Tb_{0.3}Dy_{0.7}Fe_{1.9}$) film as a function of applied magnetic field bias. Note that this plot only shows the relative magnetization (M_r) normalized to the saturation magnetization (M_s) but does not provide a quantitative measure of M_s. At high positive magnetic fields, the Mr and Ms are at unity, signifying that the film is completely saturated and the magnetization and the magnetic field are parallel. At high negative fields, the Mr/Ms is at -1, signifying that the magnetization of the field is antiparallel with the laser beam. The *remanence* is the relative magnetization which remains at zero applied magnetic field. In this example, the magnetization at zero field is 1 signifying that the magnetization remains in the direction of the magnetic field and is *in-plane*. In this manner, the in-plane or out of plane preference (i.e. the easy axis) of the magnetization can also be determined with MOKE. The field at which the film magnetization switches polarity, the *coercive field*, can be easily identified and this will be shown later to have important implications for measurements of magnetic anisotropy. Some critical limitations of this technique must be noted. Firstly, the sample must be highly reflective in order to obtain a signal from the substrate. This makes measurements of rough samples and samples with a small amount of magnetic material difficult. Secondly, the measurement averaged over the entire beam spot area, which can be as a large as $1mm^2$. This makes it impossible to measure the switching characteristics of an individual grain, domain, or nanostructure. Nevertheless, MOKE provides the fastest and easiest method to ascertain the magnetic anisotropy of virtually any film.

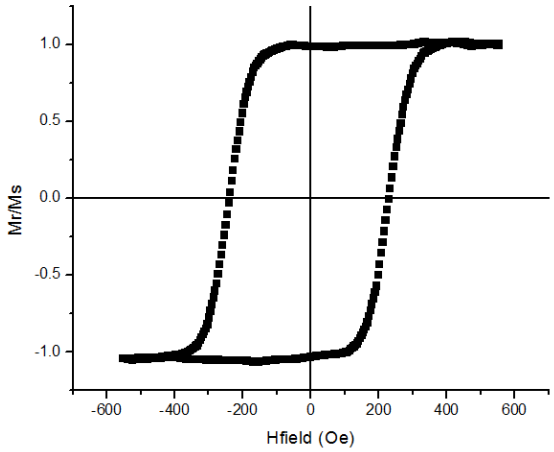

Figure 7: MOKE M-H hysteresis plot of Terfenol-D film

1.8.3 XMCD-PEEM

An advanced microscopy technique which combines the speed of MOKE with the spatial resolution of MFM is X-ray Magnetic Circular Dichroism-Photo Emission Electron Microscopy (XMCD-PEEM). The sample is bombarded with X-rays which are circularly polarized and the energy of the beam is tuned to the material being imaged (e.g. 852.5 eV for Nickel.) Upon reaching the sample, the x-rays stimulate the emission of electrons in the outer 3-4nm of the sample. The stimulated electrons are collected and accelerated with a large electric field bias, typically up to 20kV. Depending on the local magnetization of the sample, more or less electrons will be collected in that region and this dichorism results in magnetic contrast. For example, a magnetization which is parallel with the x-ray beam will have high interaction and will appear white, whereas an anti-parallel alignment will appear black. In this manner, a special image of the sample's magnetization can be created with typical resolution of about 50nm. Shown in Figure 8 are two examples of magnetic nanostructures observed in XMCD-PEEM. In Figure 8a is a 2 micron OD ring structure which shows the characteristic *onion* magnetization state typified by a spatially-varying magnetization gradient (i.e. the gradual change from black to white.) In Figure 8b is an array of single domain magnets which are 200nm in length. Here, the

magnetization is shown to be single domain because there is no change in magnetization within each bit. In the latest generation of PEEM technology, the imagining equipment and the applied x-rays can be coupled to measure the time-dependent magnetization behavior of the sample. This enables video-like observations of magnetization on time scales as small as tens of nanoseconds, providing crucial details of magnetization switching behavior. Still, one obvious drawback of this technique is that it requires the most specialized equipment, in particular a synchrotron light source capable of generating coherent x-rays. For this reason, only a few PEEM facilities exist and time to use these shared facilities is quite restricted (e.g. once every 6 months.)

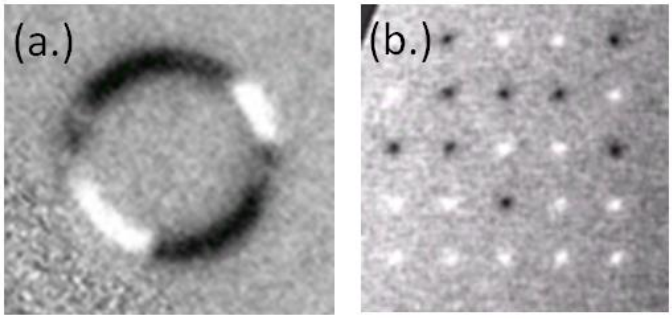

Figure 8: XMCD-PEEM images of nickel nanostructures. (a.) 2-micron OD ring structure showing specially-varying magnetization. (b.) Array of 200 nm single domain nanostructures demonstrating coherent spin structure.

1.8.4 Lorentz TEM

Transmission Electron Microscopy (TEM) involves passing high energy electrons through a sample to ascertain the crystal structure (as in bright field and dark field images) and also images of the interfacial stacking behavior. The objective lens and imaging plane can be moved relative to the sample to measure Lorentz force-induced magnetization in what is called the Fresnel mode. Lorentz imaging in Fresnel mode is simply the deflection of the electron beam due to the Lorentz force as it passes through a magnetic sample. In the Fresnel method, the

image is defocused so that the object plane is no longer in the same plane as the specimen. Depending on the local orientation of the magnetization, the beam deflection direction will vary leading to either enhanced or decreased intensity at areas of varying magnetization (i.e. domain walls). It should be noted that the required defocusing decreases the overall resolution of the technique in comparison to standard bright field TEM and can obscure structural information such as grain boundaries. However, it remains one of the highest resolution magnetic imaging techniques available, with a limit of only a few nanometers. Sample preparation is critical to achieve such high resolution imaging. In particular, the sample must be transparent to electrons and thus the thickness must be less than 100 nm. Figure 9 is an example Lorentz TEM image collected on a nickel thin film/PMN-PT heterostructure. The light gray region is a thin magnetic film less than 100 nm in thickness. The black areas are substantially thicker and thus no electrons can transmit through these regions. The magnetization of certain regions appears as bright white and black lines which can be interpreted as domain walls. Special sample preparations must be made often requiring thinning with focused ion beam milling (FIB) particularly for magnetoelectric heterostructures which often include bulk (i.e. substantially thick) substrates.

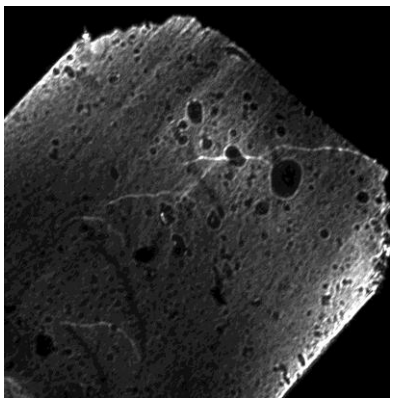

Figure 9: Lorentz TEM image of 35 nm nickel film/ PMN-PT laminate. White and black lines correspond to domain wall structures.

Chapter 2: MACROSCALE LAMINATES

2.1 Synopsis

Perhaps the most widely studied form of magnetoelectric material is the bulk laminate (i.e. a mechanically coupled composite of piezoelectric and magnetostrictive materials.) The advantage of this size regime is the accessibility of the experimental measurement techniques, since most coupling characterizations can be completed on a simple bench top. The disadvantage of bulk laminates as described in chapter1.4 is that the material is composed of multiple domains with competing magnetocrystalline and magnetostatic energies. Magnetic characterization is also limited to quantitative measurements of magnetic induction, magnetostriction, or permeability, so no direct visual observation of magnetic reorientation is possible. Nevertheless, macroscale laminates remain an essential component of many real world device applications such as sonar transducers, antennas, and magnetometers.

2.2 Literature Review

2.2.1 Magnetostriction jumps in Terfenol-D

The influence of mechanical energy on macroscale magnetic materials (i.e. Terfenol-D, $Tb_{0.3}Dy_{0.7}Fe_{1.9}$) has been studied extensively by Clark *et al.* throughout the 1970's and 80's[9]. These early experiments on monolithic Terfenol-D are an instructive demonstration of the multi-domain magnetoelastic model described earlier. Figure 10 shows the results of a magnetostriction characterization study on Terfenol-D loaded under compressive stress. Under zero stress, Terfenol-D has a maximum strain response of about 700με at a saturation field of 2000Oe. The slope of this strain-field (i.e. the piezomagnetic coefficient, dε/dH) plot under zero stress is gradually decreasing, indicating minimal magnetization realignment consistent with a

low density of non-180 degree domain rotations. By comparison, the strain-field plot at a compressive load of 7.6MPa has a dramatic increase in strain output at a field of 250Oe followed by a gradual increase until the saturation magnetostriction value of 1650με. From this result we can conclude that compressive stress in Terfenol-D increases the number of non-180 degree domain rotations resulting in maximal strain output. This is consistent with the multidomain magnetoelastic model and the "oval domain" magnetostriction model described earlier. More concisely, the magnetization in the sample switches between crystallographic easy axes under applied load as shown in the diagram in Figure 11. The compressive stress realigns the magnetizations from the [112] crystallographic direction (which is aligned with the compressive stress) to the family of [111] directions which are more or less perpendicular to the applied stress. Now when a magnetic field is applied, the magnetizations undergo a sudden "jumping" realignment from the [111] towards the [112] direction resulting in the large observed strain response[9]. If the compressive stress is increased further to 18.9MPa, the low field strain jump occurs at a higher field of 500Oe and the saturation magnetostriction increases to 1700με. Although the number of non-180 degree domain rotations again increases, the reduction in low field strain jump is due to the magnetic field having to work *against* the mechanical load. It is clear that an optimal stress bias exists to maximize the piezomagnetic coefficient and thus achieve optimal transduction of magnetoelastic anisotropy into magnetization response. A detailed study of the relationship between magnetoelastic anisotropy (i.e. voltage bias induced piezoelectric strain) and converse magnetoelectric coefficient is described later in the present work.

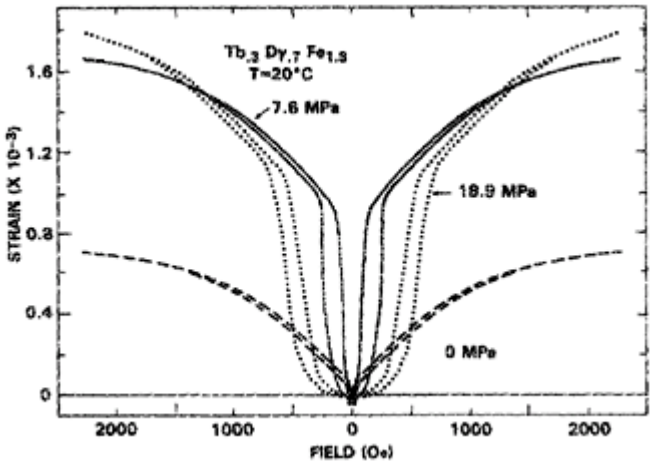

Figure 10: Magnetostrictive strain of monolithic Terfenol-D under applied mechanical load as a function of magnetic field. The magnetostriction and low field permeability is greatly enhanced from zero load to 7.6MPa. However, the higher load of 18.9MPa results in a diminished response due to the additional work required to fight against the load. (from Clark *et al.*[9])

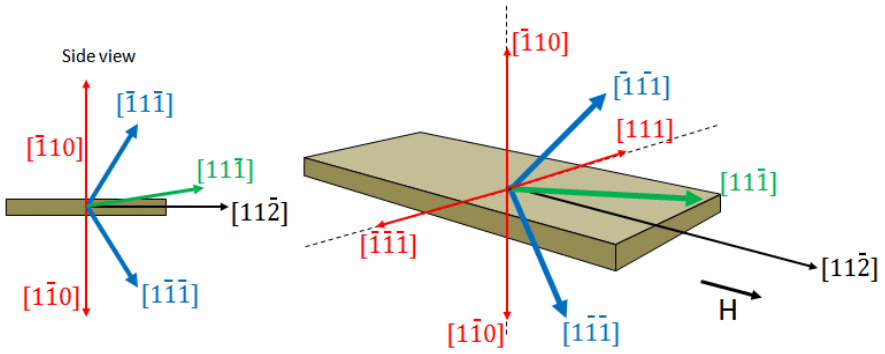

Figure 11: Schematic of monolithic [112] oriented Terfenol-D and associated crystallographic directions. Magnetizations in Terfenol-D always align themselves with the family of [111] directions.

2.2.2 CME in laminates as a function of magnetic bias field

A common macro-scale magnetoelectric device geometry is the laminated composite, that is two or more flat sheets of piezoelectric and magnetostrictive material sandwiched together[10]. The piezoelectric and magnetostrictive layers are coupled mechanically enabling

transduction between the voltage-induced piezostrain and the magnetization response of the magnetic layer. This device structure has been used to study the coupling ability of various materials and geometries; the direct and converse magnetoelectric coefficient, DME and CME, respectively. An instructive study on the role of magnetoelastic anisotropy comes from Yanmin Jia, who conducted tests on trilayer laminates of single crystal PMN-PT, a type of piezoelectric, and Terfenol-D, a type of magnetostrictive alloy. The purpose of this experiment was to study the CME coefficient of the laminate, that is, the magnetization response as a function of input voltage.

A diagram of the device structure is shown in Figure 12. An alternating voltage is applied to the piezoelectric PMN-PT layer, generating strain which is transferred to the magnetostrictive Terfenol-D. The strain reaching the Terfenol-D generates magnetoelastic anisotropy, resulting in a change in magnetization. An AC voltage of 100V at 100Hz is applied, which corresponds to an oscillating magnetoelastic anisotropy. The magnetization response of the Terfenol-D is then measured with an inductive pick-up coil which is wrapped around the entire laminate. The CME coefficient is defined as the magnetic flux (in milliGauss) over the input AC voltage, dB/dV_{AC} and is measured for a range of magnetic field biases to generate Figure 13. The CME coefficient increases sharply at low magnetic field biases until maximizing at a field of 170Oe. The coefficient then decreases gradually at higher field values. This result is consistent with the piezomagnetic response of shown earlier by Clark *et al.* and this will be discussed in detail next.

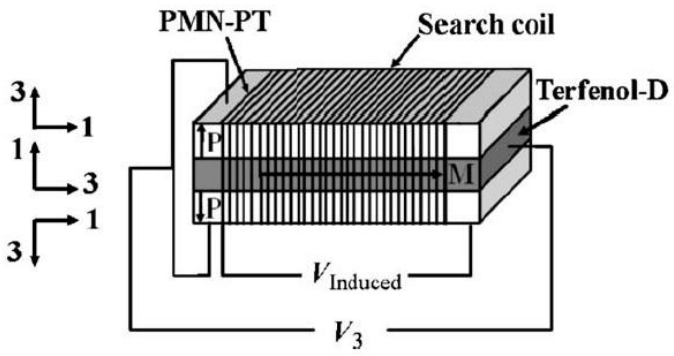

Figure 12: Schematic of Jia *et al*. experiment showing structure and measurement technique of the Terfenol-D/ PMN-PT laminate. CME coefficient is measured through the search coil.

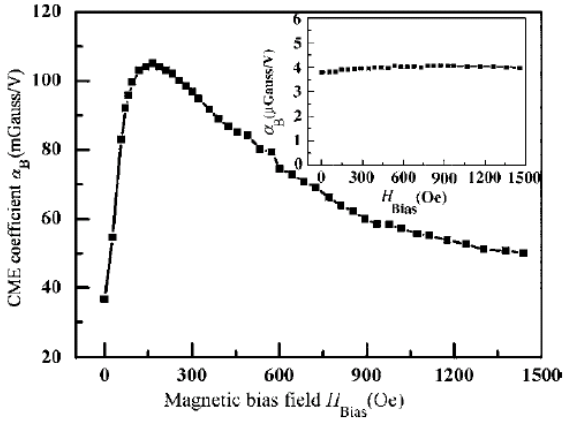

Figure 13: CME coefficient of a Terfenol-D/PMN-PT laminate as a function of magnetic field bias

We can view the results of Jia *et al.* within the context of a non-linear piezomagnetic coefficient and non-180 degree domain rotations. As described earlier, the magnetostriction response of the Terfenol-D is directly related to the incidence of non-180 degree domain rotations (since 180 degree domain rotations do not contribute to strain). For low field values, the permeability is high and the frequency of non-180 degree rotations is increased resulting in increased strain response. At high magnetic field bias values and low permeability, the field has a counterproductive effect by locking the magnetization in-line with the applied field. Locked in

this manner the non-180 degree domain rotations are minimized and thus the strain response and CME coefficient are reduced.

The rise and fall of the CME coefficient in Figure 13 is also explained by a non-linear piezomagnetic coefficient- the rate of strain change with respect to a changing magnetic field, $d\lambda/dH$. As evidenced by the experimental strain data on monolithic Terfenol-D in Figure 10, the piezomagnetic coefficient is maximal at a field of 250Oe. Indeed, The CME coefficient in Jia's data in Figure 13 also maximizes around 250Oe. From this data it can be concluded that magnetostriction plays a critical role in the mechanical control of magnetization. What this data lacks however is a detailed study on the influence of mechanical load bias on the magnetostriction and CME response. If we again look at Clark's data in Figure 10, we observe an increase in the magnetostriction and piezomagnetic coefficient with an applied mechanical load bias. We may therefore infer that an applied mechanical load will increase the magnetostriction, piezomagnetic coefficient, and CME coefficient in a magnetoelectric laminate. In this study the magnetoelastic anisotropy is constant and equivalent to the AC voltage of 100V. This study does not explore the effect of different magnetoelastic anisotropy values (i.e. voltage biases) on the total CME coefficient but this topic is explored later in the present work.

2.3 Experimental Work

2.3.1 Voltage bias influence on the CME in PZT/ Terfenol-D/ PZT laminates

2.3.1.1 Problem Introduction

Magnetoelectric (ME) materials represent an important class of active transducers with many applications in magnetometry, data storage, and actuation. These materials enable the

transduction of magnetic energy to an electric polarization (the direct magnetoelectric effect, DME) as well as the transduction of electric energy to a magnetization (the converse magnetoelectric effect, CME). CME may be especially useful for applications such as magnetic data storage, in which an electric polarization is used to write data magnetically. The use of ME materials to locally magnetize a recording media may be the ideal solution for fast data storage methods such as Electrically Assisted Magnetic Recording (EAMR)[11]. To achieve this and other applications, it is necessary to improve the CME coefficient α_{CME} (B/V_{ac}), which is a quantitative measure of magnetization intensity in response to an applied voltage. The drive to improve α_{CME} has led to advancements in component geometry, composition, and operating methods[12,13,14]. Several studies have demonstrated the dependence of α_{CME} on magnetic field bias H_{bias}[15,16] as well as input frequency[17,18], but few studies exist on the influence of voltage bias on the CME response.

Although both the DME and CME are caused by the same strain-coupling phenomenon within the ME material, the literature generally treats the two effects as separate and non-equivalent[19]. This is partially due to the presence of a nonlinear magnetostrictive phase in the magnetoelectric, thus making the ME effect a nonlinear phenomenon. From an experimental point of view, the characterization of the direct and converse magnetoelectric effects must be carried out differently[16]. Applying an oscillating magnetic field during typical DME measurements produces both 180 and non 180-degree domain wall motion within the magnetostrictive. However, the oscillating voltage technique presented in this manuscript's CME measurements produces only non-180-degree domain wall motion. Thus, the technique presented in this manuscript of applying a constant voltage bias and an oscillating voltage is different from the typical DME method of applying an oscillating magnetic field and voltage bias.

It is important to note that while the DME has enjoyed substantial experimental interest[20,21], CME has received considerably less attention. A significant cause for this disparity is the difficulty inherent in conducting magnetization measurements. Wan *et al.*[22] performed some of the first experimental CME measurements on the magnetization of a PZT/Terfenol-D laminate using a localized surface-mounted search coil. The high degree of magnetic flux leakage from this setup necessitated the development of an improved method. Jia *et al.*[10] wrapped a search coil around the entire trilayer (three-layered laminate) PMN-PT/Terfenol-D and later on stack laminates of PZT and Terfenol-D to improve the magnetic measurements[23]. Using this search coil method, several studies have been conducted which demonstrate the influence of magnetic field bias[16,24] on the CME response in laminates of varying composition[13] and geometry[23].

A recent study suggested that applying a voltage bias could improve the CME response in ME laminates further than previously reported[24]. The voltage bias on an ME laminate is equivalent to applying a compressive stress via the converse piezoelectric effect. In magnetostrictive materials, such as Terfenol-D, this compressive stress dramatically increases the magnitude of the magnetostriction response λ[25]. The magnetostriction property enhancement is the result of a forced realignment of the local magnetization toward an easy axis relatively perpendicular to the magnetic field direction. The piezomagnetic coefficient ($d\varepsilon/dH$) also increases as a result of this improved magnetostriction response. In ME laminates, increasing the piezomagnetic coefficient increases $\alpha_{CME,}$ which is the product property of both piezomagnetic and piezoelectric coefficients[26]. Wu *et al.*[24] demonstrated the influence of voltage bias on the CME response of a macro-fiber composite (MFC)/metglas laminate. The voltage bias increased the α_{CME} up to 8% and the tunability range was approximately 18%. Careful selection of the materials that make up the ME composite may create an arrangement in which the effects of

voltage bias are more pronounced than measured by Wu *et al.* Other studies have also demonstrated a change in the magnetization response of an ME material due to voltage bias[27]. It is important to note that previous studies investigate a quasi-static magnetization response to an oscillating magnetic field at a fixed voltage bias (emu) and not a dynamic induced magnetic field response to an ac voltage (G/V_{ac}) at a fixed voltage bias as studied in the present work. It is the dynamic ac excitation voltage at a voltage bias while measuring induced magnetic field that provides such a large improvement in the magnetoelectric response.

The purpose of this study[28] is to experimentally determine the degree and extent of the effect that voltage bias has on the CME response of a PZT/Terfenol-D/PZT trilayer laminate. Experimental results indicate that α_{CME} can be tuned by over 400%. The combination of PZT with Terfenol-D in a laminate geometry offers especially large gains in α_{CME} compared to the laminate study conducted by Wu *et al.* due in part to the large changes produced in the piezomagnetic coefficients by the applied load. Furthermore, larger range changes are possible with more careful selection of constituents than reported in this manuscript.

2.3.1.2 **Experimental Setup**

The ME test sample is a bonded three-layered laminate composed of two PZT plates and one Terfenol-D plate. Figure 14 illustrates the structure and instrumentation of this ME laminate. The PZT plates measure 30x10x0.5 mm^3 and are poled through the thickness with a d_{31} piezoelectric coefficient of -340 pC/N (TRS610HD, TRS Technologies Inc.). The Terfenol-D plate measures 35x10x1mm^3 (Etrema Products, Inc) and is textured along the [112] crystallographic axis to maximize magnetostriction in the longitudinal direction (i.e. *M* direction in the figure). The PZT plates are bonded on both sides of the Terfenol-D such that they are poled in opposite directions. A thin layer (approximately 100 microns) of Emerson & Cuming

CF3350 sheet epoxy joins the PZT and Terfenol-D plates, and the entire assembly is cured in a 165°C oven for 40 minutes under light mechanical compression. The thickness of the entire assembly is roughly 2mm.

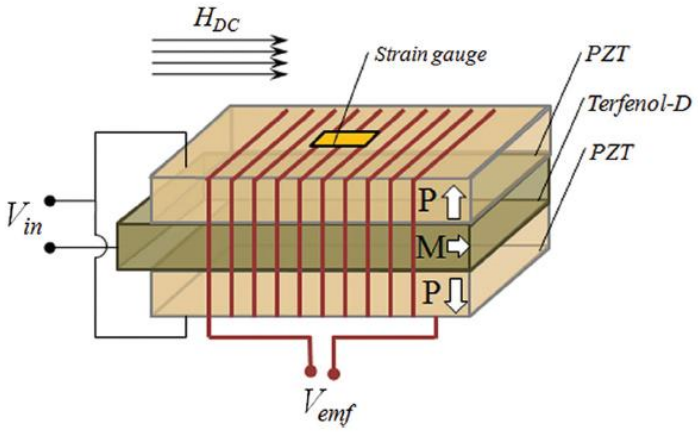

Figure 14: Schematic of experimental setup for measurement of magnetostriction and magnetic flux and for application of magnetic field, AC excitation voltage, and DC voltage bias to PZT/Terfenol-D laminate.

Strain (ε) in the ME laminate is measured using two Vishay EA-06-062AP-120 strain gauges which are applied to the surface of both PZT plates along the longitudinal, or M direction. The purpose of the two strain gauges is to verify that the laminate does not bend due to an unequal expansion of the constituent layers. In this study the difference in the two strain gauges was less than 15% and all reported measurements are an average of the two data sets. It is important to point out that the strain induced in the Terfenol-D plates by the PZT is a biaxial strain which is different from the characterization tests historically reported on Terfenol-D[25]. That is, typically uniaxial loading is applied to the Terfenol-D during characterization.

The CME response of the laminate is characterized by measuring the induced magnetization under the application of a known ac electric field. During these measurements, both a dc electric voltage and a dc magnetic field are applied to investigate the influence of these

parameters on the CME response. A Varian V4005 electromagnet with field strength varying in magnitude from 0 to 3000 Oe is used to generate the dc magnetic field in the longitudinal or M direction. The magnitude of the magnetic field is measured using a Bell 6010 Gauss meter with a resolution of 0.1 Oe placed directly adjacent and at the middle of the sample. An ac electric voltage (0.1 to 30 V_{rms}, 20kHz) and dc electric voltage bias (-200 to 750 V) are applied to both PZT plates simultaneously using an Agilent 33120A function generator which is amplified with a Trek 50/750 amplifier. The applied voltage is monitored with a Tektronix TDS 460A oscilloscope using a 10:1 passive probe. The entire laminate is submerged in silicon oil to prevent electric breakdown of the air due to the relatively large electric fields applied. The magnetic flux density B generated by the Terfenol-D induces an electromotive force V_{emf} in a 110-turn copper wire induction search coil which is wrapped around the entire laminate. The induced voltage in the search coil is used to calculate the magnetic flux density according to the formula

$$B = \frac{V_{emf}}{A \times N(2\pi f)}$$

where V_{emf} is the induced electromotive force in volts, A is the cross sectional area of the search coil, N is the number of search coil turns, and f is the frequency of the applied ac electric voltage[24]. It is important to note the distinction between the static measure of magnetization change (emu) in response to magnetic field bias and the dynamic magnetic field response to ac voltage presented by formula 1. Finally, the CME coefficient which describes the output magnetic flux developed by an applied electric field is defined as $\alpha_{CME}=B/V_{ac}$[25]. The applied voltage and induced voltage in the search coil are oscillatory in nature, so the *rms* voltage and the rms magnetic flux density values are used in the calculations of α_{CME}.

2.3.1.3 Experimental Results

The frequency dependence of the CME effect in the ME laminate is shown in Figure 15. The results are for an applied magnetic field bias of 300 Oe with an ac excitation voltage of $10V_{rms}$ applied during the test and the dc voltage bias is zero. The graph shows a sharp increase in CME response around 35 kHz consistent with the first modal resonant frequency of the ME structure. In this study all reported tests are conducted at 20 kHz, i.e. the laminate is operated at quasi-static frequencies to mitigate the amplifying effects of resonant oscillation.

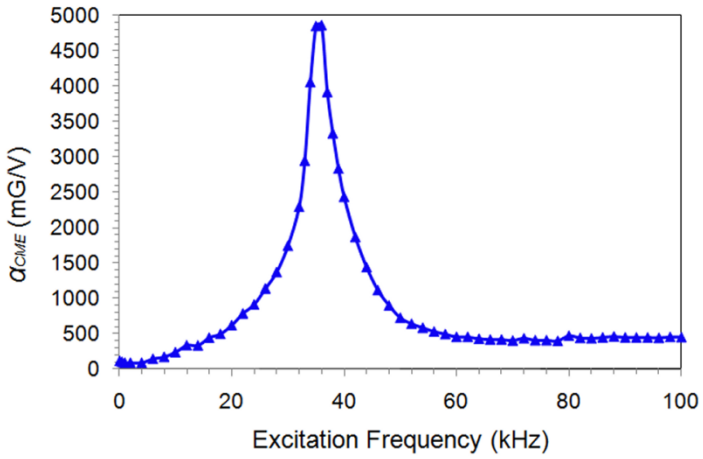

Figure 15: CME coefficient of the magnetoelectric trilayer laminate as a function of excitation frequency for Vac=10Vrms at a magnetic field bias of 300Oe

The strain response of the ME laminate as a function of a quasi-static longitudinal magnetic field is shown in Figure 16 for a range of dc voltage biases. At an applied voltage of 0V, the applied magnetic field increases the strain up to saturation values on the order of 300με. As the voltage is increased to 100V, 200V, 300V, 500V, and 700V, the saturation strain increases to 350με, 400με, 550με, 600με, and 650με, respectively. There is also an increase in the saturation field with increasing voltage bias, from about 3000 Oe at 0V to approximately 4000 Oe at 700V. The increasing trend in magnetostriction is understood to be an effect of

magnetic domain reorientation within the Terfenol-D[29]. As positive voltage is applied to the piezoelectric plates, a biaxial compressive stress is developed in the Terfenol-D through the converse piezoelectric effect. Compressive loading along the [112] (i.e. direction of M in Figure 14) is known to increase the prevalence of magnetic domains lying along the family of [ıı1] easy axes which lie perpendicular to the compressive stress[29]. As the magnetic field is applied, the magnetic domains rotate to the family of [ıı1] easy axes which lie closest to the direction of the applied field (i.e. same direction as the stress)[29]. It can be seen that compressive loading (i.e. in Figure 16 for positive voltage) increases the measured saturation strain. However, as shown in Figure 16, an increase in voltage from 700V to 750V results in a reduction in magnetostriction for a given magnetic field. This reduction is due to the increased saturation field required to rotate the domains and overcome the relatively larger compressive stress. As can be seen in Figure 16, a -100V and -200V bias decreases the strain from 300με to 275με and 250με, respectively. A negative voltage bias is equivalent to a biaxial tensile stress on the Terfenol-D, which aligns the family of [ıı1] easy axes with the tensile stress (and measurement direction) and consequently decreases the magnetostriction.

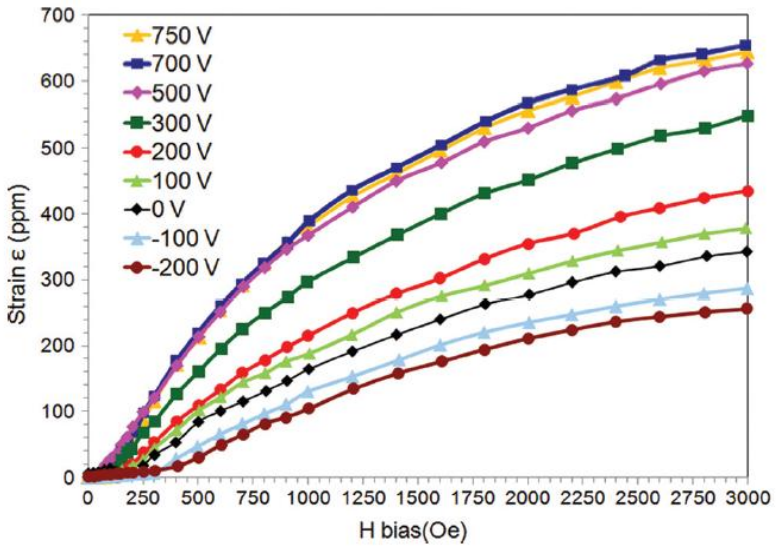

Figure 16: Magnetostriction response of PZT/Terfenol-D laminate as a function of applied magnetic field and DC voltage bias.

In addition to alterations in saturation strain with applied voltages, the slope of the magnetostriction curve (i.e. piezomagnetic coefficient $d\varepsilon/dH$) is also modified by an applied voltage as shown in Figure 17. First, the slope at both H_{bias}=0 Oe and at very large H_{bias} (i.e. 3000 Oe) approaches 0. Furthermore, the slope in all curves appear largest for magnetic fields below about 500 Oe, pointing to the existence of a maximum piezomagnetic coefficient in this region. Finally, the magnetic field at which the slope is largest shifts toward lower magnetic field values with increasing voltage bias. All of these results are consistent with data presented on monolithic Terfenol-D subjected to a uniaxial compressive load[25].

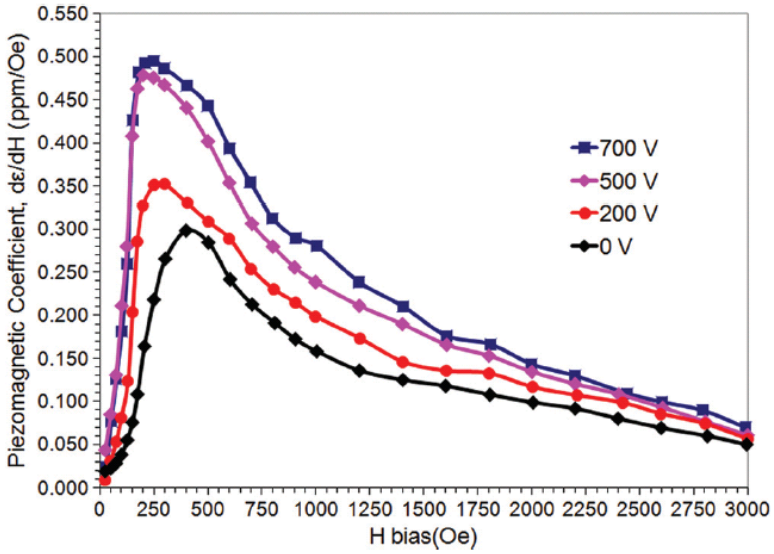

Figure 17: Piezomagnetic coefficient of PZT/Terfenol-D laminate as a function of applied magnetic field and DC voltage bias.

The magnetic flux density *B* from the ME laminate as a function of rms input ac voltage V_{ac} at various magnetic field biases H_{bias} is shown in Figure 19. The driving frequency for this test is set to 20 kHz (below the resonant region) and the DC voltage bias is set to 0. From Figure 17 it is clear that increasing the excitation voltage V_{ac} results in a linear increase in magnetic flux density output. The slope of the lines represents the CME coefficient α_{CME} (B/V_{ac}) indicating that α_{CME} is relatively constant over the measured ac voltage range of 0 to 30 V_{ac}. Focusing on the influence of magnetic field bias on $\alpha_{CME,}$ a clear difference is observed. The CME coefficient (slope of each line) initially increases as applied magnetic field bias H_{bias} increases from H_{bias}=0 Oe to H_{bias}=250 Oe. At a bias value of 250 Oe the CME coefficient reaches a maximum. An optimal value of magnetic field thus exists to maximize the CME coefficient. Further increases to the H_{bias} beyond 250 Oe result in a decrease in the CME coefficient. At very high magnetic fields such as 3000 Oe, the CME coefficient decreases and will likely approach zero near saturation. The results in Figure 18 can be understood in terms of the piezomagnetic coefficients

described in the discussion of results in Figure 17. That is, a maximum in the piezomagnetic coefficient $d\varepsilon/dH$ can be seen for magnetic fields below 500 Oe, but the coefficient tends toward zero with increasing magnetic field. The general trend in these results is consistent with previous measurements of CME as a function of H_{bias}[16].

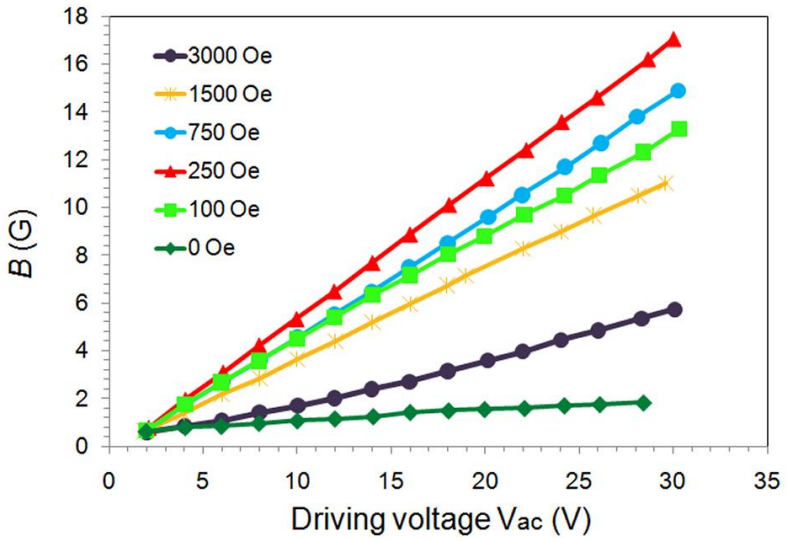

Figure 18: Induced magnetic flux B as a function of driving excitation voltage Vac for various voltage biases. The induced flux is a function of piezomagnetic coefficient which changes for different field biases.

The influence of dc voltage bias on the CME coefficient as a function of an H_{bias} is shown in Figure 19. The excitation voltage V_{ac} for this test is 10 V (rms) and the input frequency is 20 kHz. The figure shows that the CME coefficient is modified by the application of a dc electric field bias, and that it also responds to changes in magnetic field. For each curve representation of an applied voltage, the magnitude of the CME response starts at some low value when the magnetic field is 0 Oe. As the magnetic field is increased, the CME coefficient increases rapidly and peaks for magnetic fields between 200 and 300 Oe. After this rapid increase, the CME response declines slowly with additional increases in field strength. The

CME response can be assumed to vanish for a sufficiently high magnetic field consistent with the saturation field. The rise and fall of the CME response can be explained in terms of the *product property* of the piezoelectric and piezomagnetic coefficients[26]. More importantly in this figure, results show that the magnitude of the dc voltage bias also significantly affects the CME coefficient. As the voltage bias is increased from 0 to 700V at an applied magnetic field of 250 Oe, one can observe an increase in α_{CME} from 0.55G/V to 1.65G/V. The reason for this increase is consistent with the discussion provided in Figure 16, i.e. compressive loads increase magnetostriction and the piezomagnetic coefficient[29]. In contrast, as the voltage is reduced from 0V to -200V, the α_{CME} decreases from 0.55G/V to 0.4G/V. This is due to the fact that a tensile load decreases magnetostriction and piezomagnetic coefficient (see Figure 16). From -200V to 700V at 250 Oe, α_{CME} changes by more than 400%, representing a giant tunable range in α_{CME} values. The range of control offered by this laminate is considerably larger than the 18% tunability presented by Wu *et al.*[24]. Additional increases to the voltage bias above 700V (e.g. 750V) result in a reduction in the CME response due to the decreases in magnetostriction and the piezomagnetic coefficient described in the discussion of Figure 16. It is important to note that while the piezoelectric coefficient is known to change with voltage bias [19,30], the change is relatively small compared (i.e. for the electric fields evaluated) to the change in the piezomagnetic coefficient presented in this work. Therefore, enhancement of piezomagnetic coefficients with applied constant voltage are the primary cause of the increases observed in α_{CME} presented in this paper.

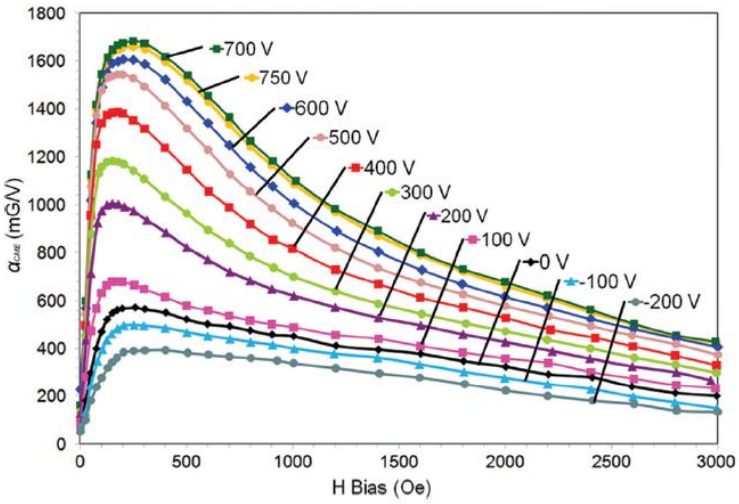

Figure 19: CME coefficient response of PZT/Terfenol-D laminate as a function of applied magnetic field and DC voltage bias.

The influence of voltage bias on the optimal magnetic field bias can also be seen in Figure 19. At 0V bias, the peak α_{CME} occurs at a magnetic field bias of 200 Oe. As the voltage bias is increased to 300V, the optimal H_{bias} decreases to 175 Oe. Increasing the voltage bias beyond 300V (i.e. 700V) shifts the optimal H_{bias} to 250 Oe. The optimal α_{CME} occurs when the product property of the piezoelectric and piezomagnetic coefficient are at a maximum. The optimal H_{bias} thus exists when the piezomagnetic coefficient is at a maximum. From experimental data on uniaxial compressive loading of bulk Terfenol-D[25], it is clear that the optimal H_{bias} for maximizing the piezomagnetic coefficient follows a similar pattern of decreasing then increasing with increasing load.

2.3.1.4 Concluding Remarks

The effect of electric voltage bias on the CME response of a PZT/Terfenol-D/PZT laminate has been experimentally determined. Increasing voltage bias was shown to greatly improve the magnitude of the CME coefficient α_{CME}, by as much as 400% for the optimal dc bias

voltage of 700V. This represents a dramatic expansion in the tunable performance characteristics of the laminate. While it is true that the piezoelectric coefficient changes in response to voltage bias[30], the relatively small changes cannot be responsible for the 400% shift presented in this work. Increasing the voltage bias was shown to shift the optimal magnetic field bias toward lower values and to also increase the saturation field and saturation magnetostriction. Utilizing voltage bias enables the tuning of the CME coefficient at a static magnetic field bias. Additional tunability may be achieved if the system is operated at resonance. Voltage induced stresses on the Terfenol-D via mechanically coupled piezoelectric strain are the chief reason for these modifications to α_{CME}.

2.4 Macroscale Concluding Remarks

In the preceding chapter the influence of magnetoelastic anisotropy on bulk magnetoelectric laminates was studied. Here an applied electric field to a piezoelectric laminate caused a change in the magnetic response of the laminate by stress-induced magnetic domain rotation. By rotating the magnetization, the stress influenced the magnetostriction and piezomagnetic properties of the laminate, thereby modulating the magnetoelectric transduction effectiveness. This was measured experimentally in Terfenol-D/PZT laminates by observing the change in CME coefficient with applied voltage bias. While a definite change in magnetic behavior with applied strain is measured in macroscale laminates, deterministic control o the magnetic phase cannot be achieved without first reducing the competing magnetostatic energies.

Chapter 3: THIN FILM HETEROSTRUCTURES

3.1 Synopsis

The influence of magnetoelastic anisotropy on the magnetization of thin film heterostructures is examined in this chapter. In thin film heterostructures, the scale of the magnetic phase is reduced in thickness until it is a nanostructured film less than 100 nm. Meanwhile, the piezoelectric phase is a bulk plate like in macroscale elements, so the general architecture remains a two phase heterostructure. Thin film heterostructures thus represent the next scale reduction after macroscale laminates since the magnetostatic energy is greatly reduced and the magnetization is generally confined in the plane of the film. Because of the reduced shape anisotropy, magnetic reorientation by magnetoelastic anisotropy is significantly easier in thin film heterostructures and some of the first magnetic observations were conducted on thin film structures. The form factor of thin film heterostructures makes it of particular technological interest for magnetic hard disk applications so it remains a popular field of study. Still, thin films usually contain multiple domain walls and this prevents true deterministic control of the magnetic phase.

3.2 Literature Review

3.2.1 Electrical reversible and permanent magnetization reorientation

The magnetization behavior of thin film materials is often very different from that of bulk. In some films, the reduced out-of-plane dimension significantly increases demagnetization energy in this direction. The magnetization may thus lay in-plane or out-of-plane depending on magnetostatic energy preference, which is ultimately determined by the thickness of the film and

the magnetic material. The domain walls themselves undergo transformations as a function of thin film thickness. For example, in nickel thin films above 100nm in thickness the magnetization can be found in separate domains perpendicular to the thin film surface separated by 180-degree Bloch domain walls[7]. In magnetic force microscopy (MFM) images these walls appear as a set of regular "stripe" patterns. As the thickness of the film is reduced to 35nm, the magnetization rotates to lay in-plane. The now 90-degree domain walls also lay in plane and are now called Néel walls. MFM images reveal no stripe patterns because the magnetic flux is now enclosed within the film. These considerations are important because the native magnetization of the film determines the magnitude and nature of the response to magnetoelastic anisotropy.

An instructive experiment on the behavior of in-plane magnetized thin films with magnetoelastic anisotropy comes from Tao Wu *et al.* who in 2011 prepared magnetoelectric laminates of Nickel thin film on PMN-PT single crystals[31]. The unique element in this experiment is the single crystal PMN-PT (011) which has an anisotropic piezostrain response with applied electric field. Recall that anisotropic strain is necessary to create magnetoelastic anisotropy and initiate magnetization rotation. In Figure 20 we see the strain response of the PMN-PT along one crystallographic direction as measured by the strain gauge technique. While the full bipolar loop (in black) appears like a classic butterfly loop, what's unusual about this material is its behavior under partially reversing electric fields. In the .14MV/m bipolar loop (green) there are significant remnant strains upon returning to 0MV/m. In later experiments this ability to control strain states with electric field will prove essential for experiments concerning magnetoelastic anisotropy.

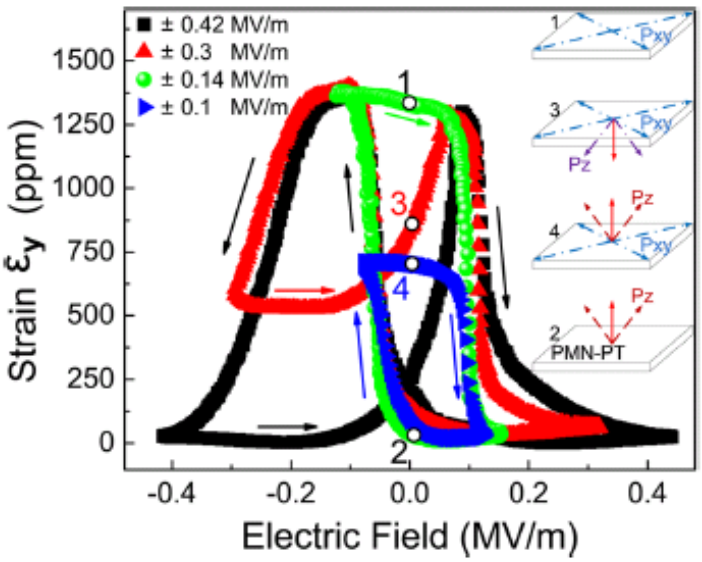

Figure 20: Strain response of PMN-PT (011) for uni-polar and bi-polar sweeping electric fields demonstrating remnant strains which can be controlled by the reversing electric field. The full bipolar loop is shown in black.

If the PMN-PT substrate is poled, then partially de-poled as in the .1MV/m bipolar curve in Figure 20, we can achieve fully reversing anisotropic strains. If we then deposit a thin film at this partially de-poled state and apply a fully polarizing electric field we may achieve a strain response as in Figure 21. From the point of view of the deposited film, the polarity of the strain anisotropy reverses completely and these strain states are stable at zero applied field. Remarkably, PMN-PT (011) not only has significant anisotropic strains, but the polarity of these strains can be reversed. If these strains are coupled to a magnetostrictive thin film then significant reversible and stable magnetoelastic anisotropy can be created. This was exactly the next experiment completed by Tao Wu *et al.*

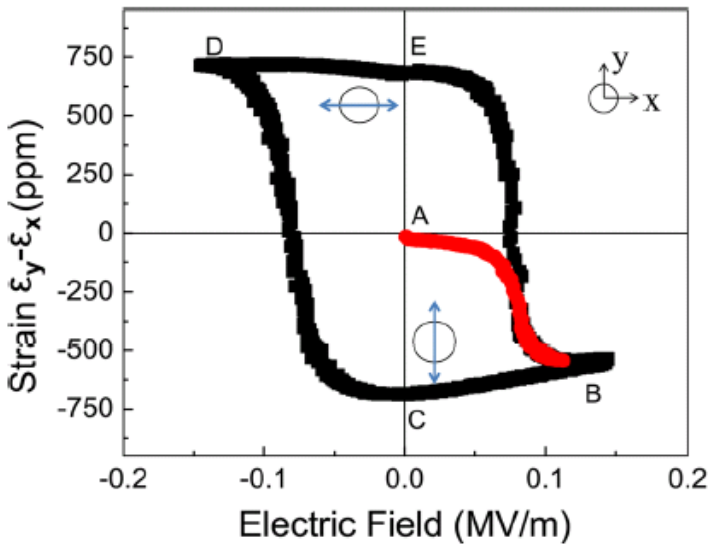

Figure 21: Reversible anisotropic strain hysteresis of PMN-PT (011). Points E. and C. have equal and opposite anisotropic strains which may enable a reversible magnetoelectric memory device.

A 35nm thick Nickel thin film was deposited on the partially de-poled PMN-PT (011) substrate. The thin film at this stage has no magnetoelastic anisotropy and would appear to have isotropic in-plane magnetization behavior. Electric fields are now applied to the substrate and the M-H curves as measured by MOKE appear in Figure 22. First, an electric field of +.14MV/m is applied to the substrate and the magnetic response along two orthogonal directions is measured (red plots in Figure 22a and Figure 22b. The magnetic response along the x appears hard while the response along the y direction appears easy. The magnetoelastic anisotropy coming from the anisotropic strain of the PMN-PT is changing the magnetic behavior of the Nickel thin film. One possible interpretation is that the magnetization of the Nickel film rotated toward the y direction. When the electric field is removed (0MV/m) this magnetic anisotropy remains because the strain anisotropy is also retained in the PMN-PT (011). Next a reversing electric field of -.14MV/m is applied to the substrate and again the magnetic behavior is observed by MOKE (green plots in Figure 22). The magnetic anisotropy in the film reverses due to the reversing magnetoelastic

anisotropy. The Nickel thin film thus underwent a completely reversing magnetization rotation due to magnetoelastic anisotropy. The magnetic anisotropy is again retained at zero electric field due to the remnant strain of the substrate.

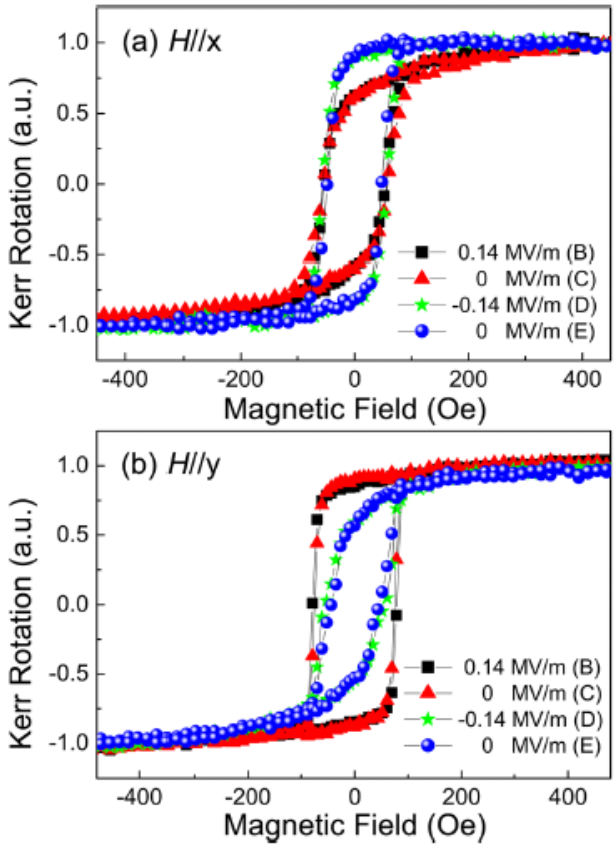

Figure 22: Magnetic hysteresis response of a Nickel thin film on PMN-PT (011) at various voltages measured in the x-direction (top) and y-direction (bottom). These plots demonstrate reversible anisotropic strain states and manipulation of the film's magnetic easy axis.

The remarkable achievement of Tao Wu *et al.* is the completely reversible and stable magnetization rotation achieved with only an electric field. Let's consider again the unique behaviors of the thin film and substrate which made this experiment successful. The thin film used was *magnetostrictive* Nickel, a necessary attribute for generating magnetoelastic anisotropy. The thin film was continuous thus eliminating shape-induced anisotropy. At 35nm, the Nickel

film was sufficiently thin to achieve pseudo-single domain in-plane magnetization response which is critical for in-plane magnetization rotation. From the point of view of the substrate, PMN-PT (011) was able to provide significant anisotropic strain required to generate magnetoelastic anisotropy. We may consider PMN-PT (011) an ideal material for future experiments involving magnetoelastic anisotropy in thin films and nanostructures. This will be demonstrated later in the present work.

3.2.3 Magnetoelectric 90° bistable switching in thin films

The work of Wu *et al.* demonstrated the magnetoelastic coupling between a thin film and a bulk substrate. One unfortunate consequence of using PMN-PT (011) in this manner is that the anisotropic strain response is hysteretic. This hysteretic behavior is energy and heat intensive and puts limits on the operating frequency of a magnetic memory device. In addition, the switching energy barrier in Wu *et al.* was predetermined by the material properties and was left unmodified. These shortcomings were addressed by Tiercelin *et al.* in their experiment on thin film/piezoelectric stack composites[32]. As shown in Figure 23, the device consists of 15 exchange coupled multilayers of $TbCo_2$ (5nm) and FeCo (5nm) on a macroscale PZT stack actuator. The advantage of using a stack actuator in this situation is that the strain response behaves linearly and has access to negative strain regimes as well. The novel achievement of this work is the establishment of a uniaxial easy axis with the exchange coupled multilayers. As shown in the diagram on the right side of Figure 23, a magnetic field bias (Hs) is then applied 90° to the magnetization easy axis (EA). The field bias applied in this manner lowers the energy barrier between the stable states defined by EA and in fact rotates them 45° to the new stables states labeled “0” and “1”. Note that these 0 and 1 states are now 90° from each other. Tiercelin *et al.*’s next step was to align these 0 and 1 states with the magnetoelastic anisotropy from the PZT stack actuator.

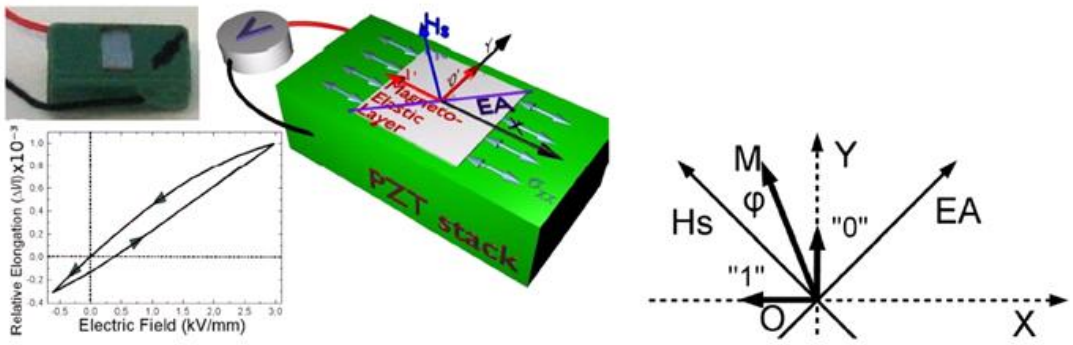

Figure 23: Schematic of nanostructured thin film/PZT stack actuator with strain-electric field response curve (left). Distribution and conventions for anisotropies and magnetization in this system showing bi-stable bit states (right). (from Tiercelin *et al*.[32])

When an electric field is applied to the stack actuator, the magnetization deterministically switches into either the 0 or 1 state depending on the polarity of the applied electric field (i.e. the sign of the strain anisotropy). As shown in Figure 24, the magnetization of the film over time was measured using magneto-optic Kerr effect (MOKE) for various applied electric field. The Kerr signal changes over time in accordance with the strain field, demonstrating that a magnetic switching event has taken place in the film. Furthermore, the magnetization rotation is permanent even at zero applied electric field due to the magnetic field bias-defined energy wells. Finally, the switching even is reversible owing to the reversing polarity of the anisotropic strain field. The magnetization of the film can be switched repeatedly and deterministically with short electric field pulses to the substrate. This work thus demonstrates the feasibility of energy barrier manipulation and non-hysteretic piezoelectric strain. This technology has remarkable consequences for applications desiring low energy and high frequency switching. An adaptation of this device structure will be demonstrated later in the present work for single domain magnets, where the easy axis is defined not by exchange bias but by shape anisotropy.

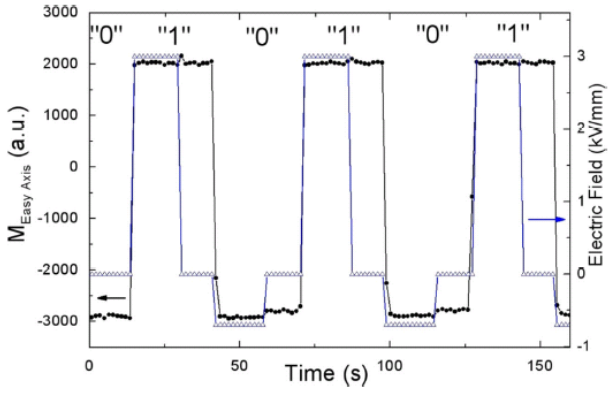

Figure 24: Plot of magnetization over time for the thin film/PZT stack actuator showing reproducible switching of magnetization from state "0" to state "1" demonstrating bi-stable 90° magnetization switching.

3.3 Experimental Work

3.3.1 Manipulation of closure domain wall in Ni/PMN-PT heterostructure[1]

3.3.1.1 Problem Introduction

This paper reports experimental observations of partial and reversible out-of-plane magnetization change in a thin film Ni/$[Pb(Mn_{1/3}Nb_{2/3})O_3]_{0.68}$-$[PbTiO_3]_{0.32}$ (001) heterostructure. Electric-field-induced isotropic in-plane compressive strain (~1000 ppm) eliminates the stripe domain pattern in a 60-nm-thick Ni thin film. When the electric field is removed, the stripe domains are returned to their original configurations with some domain wall pinning perturbations due to ferroelectric domain texturing. The observed domain structure change is attributed to the transition from Bloch wall to Néel wall and the broadening of the Bloch wall. This out-of-plane magnetization change does not occur in thicker (100-nm-thick) Ni thin film.

[1] Author's note: this section is derived from the work (C.-J. Hsu, J. L. Hockel, and G.P. Carman. Appl. Phys. Lett. 100, 092902 (2012)) which was co-authored by Joshua Leon Hockel and Chin-Jui Hsu, with equal contributions from both authors. Therefore, certain figures and descriptions may also appear in the dissertation by Chin-Jui Hsu, published at UCLA in 2012.

Controlling the magnetic properties (e.g. magnetization direction or domain structure) in thin films has important applications in both current and future devices, e.g. hard drive[33] and magnetic random access memory[34]. During the past decade, the magnetic domain structure in nanoscale nickel thin film (i.e. 2 to 200 nm) has been extensively studied.[35,36,37,38] Researchers have shown that the magnetic domain structure (e.g. maze/stripe domain pattern[38] or flux closure[36]) is extremely sensitive to film thickness (t) and magnetic anisotropy energy, with dramatic changes occurring in the t < 100 nm region.[36,37] Although many of these studies are for epitaxial Ni thin films, similar results are found in polycrystalline (i.e. non-textured) Ni thin film.[39]

One approach to control the magnetic domain structure of thin films is with magnetoelectric (ME) heterostructures (e.g. multiferroics).[40,41,42,43] Several studies report electric field induced strain produces substantial in-plane magnetization changes in Ni/ferroelectrics ME systems, e.g. 35-nm-thick Ni on $LiNbO_3$,[44] 35-nm-thick Ni on $[Pb(Mn_{1/3}Nb_{2/3})O_3]_{0.68}$-$[PbTiO_3]_{0.32}$ (PMN-PT),[45] 100-nm-thick Ni on $BaTiO_3$,[46] and 100-nm-thick Ni on $Pb[Zr_{0.52}Ti_{0.48}]O_3$ (PZT) hybrid structure[47]. Furthermore, studies have been conducted on many other nanoscale ferromagnetic thin films (e.g. CoFe,[48] $CoFe_2O_4$,[49] Fe,[50] Fe_3O_4,[51] FeGaB,[52] FePt,[53] and $La_{0.7}Sr_{0.3}MnO_3$[54]) deposited on different ferroelectric substrates (e.g. $BaTiO_3$,[48,50] $[Pb(Zn_{1/3}Nb_{2/3})O_3]_{0.94}$-$[PbTiO_3]_{0.06}$ (PZN-PT),[49,51,52,53] and PMN-PT[51,54]). While a variety of studies are present, Ni thin film is probably one of the more well understood systems in terms of thickness dependence on magnetic domain structure. Furthermore, the majority of these thin film ME studies (including Ni) focus on in-plane magnetization changes rather than the out-of-plane magnetization changes which is of particular importance to modern magnetic recording technologies.[33,43] The main reason studies focus on in-plane magnetization changes is the relatively smaller energy barrier to reorient in-plane magnetization as compared to reorienting

out-of-plane magnetization as described in theoretical analyses.[55,56] While the theoretical prediction shows that out-of-plane magnetization rotation is possible in Ni ME heterostructure,[55,56] the changes observed in reported experiments are fairly trivial.[39]

In this study, we experimentally demonstrate electric-field-controlled magnetization change from out-of-plane to in-plane in a 60-nm-thick Ni/PMN-PT (001) heterostructure. MFM results show significant and reversible changes in the stripe magnetic domain structures (i.e. elimination of stripe domains) with the application of electric fields. The observed domain structure changes are attributed to a transition from Bloch wall to Néel wall in the Ni thin film, or as a broadening of the Bloch wall. Furthermore, for a relatively thicker film (100 nm), a similar electric-field-induced domain structure change is not observed. A discussion on the relationship between electric-field-induced strain, magnetostriction, and domain wall transition in Ni thin film is provided.

3.3.1.2 Experimental Setup

The test sample consists of a 60-nm-thick Ni thin film deposited onto a 0.5-mm-thick (001) cut single crystal PMN-PT. Prior to Ni deposition, a 10 nm Ti adhesive layer and a 50 nm Pt electrode layer were deposited on the both sides of the PMN-PT. The 60-nm-thick Ni thin film was E-beam evaporated after the PMN-PT sample was poled with an electric field of 0.8 MV/m to prevent residual strains caused by the poling process. An additional 100-nm-thick Ni/PMN-PT (001) sample was also fabricated. All test results presented are from the 60-nm-thick Ni/PMN-PT (001) sample unless otherwise stated.

3.3.1.3 Experimental Results

Figure 25a shows the in-plane (i.e. both x and y directions) strain versus electric field curves (ε-E curves) of the 60-nm-thick Ni/PMN-PT (001) sample. The ε-E curves were measured by mounting a biaxial strain gauge on the sample surface with a triangular electric field waveform applied at 0.01 Hz. As shown in Figure 25a, an isotropic in-plane compressive strain (i.e. $\varepsilon_x = \varepsilon_y$) as large as 1000 ppm is produced when an electric field of 0.8 MV/m is applied, and remnant strain is absent when the electric field is removed. For MFM testing purposes, the electric field (E) was limited to the unipolar case of $0 \leq E \leq 0.8$ MV/m to prevent de-poling and subsequent reversal of polarity. An illustration of the MFM test setup is shown in the inset of Figure 25a.

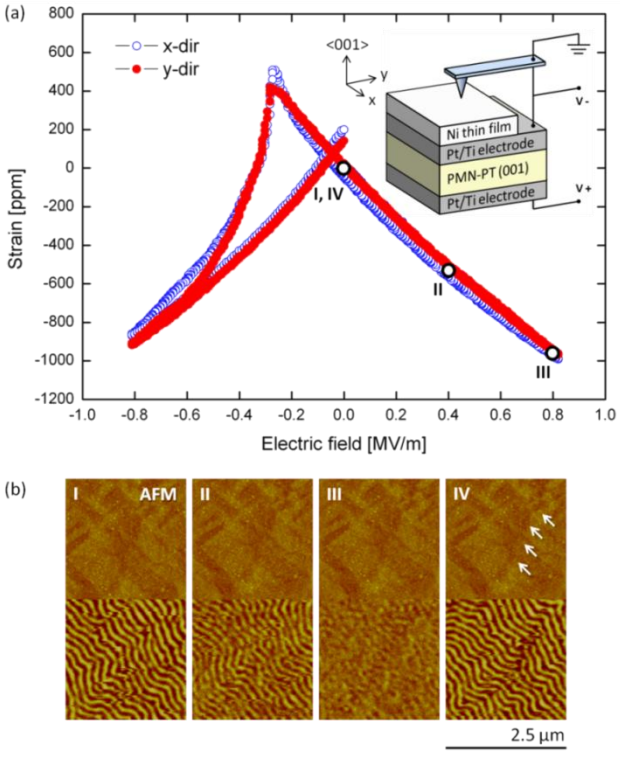

Figure 25: (a) In-plane piezoelectric response of 60-nm-thick Ni/PMN-PT (001) sample and (b) AFM and MFM images of 60-nm-thick Ni thin film on PMN-PT (001) substrate. (I) 0 MV/m, (II) 0.4 MV/m, (III) 0.8 MV/m, and (IV) 0 MV/m. Inset in (a): Illustration of 60-nm-thick Ni/PMN-PT (001) in the MFM experiment. Arrow signs in (IV) point out the domain wall pinning positions.

Figure 25b shows the AFM topographic height images and corresponding MFM domain images of the 60 nm Ni thin film captured at four different applied electric fields (i.e. points I, II, III, and IV corresponding to 0, 0.4, 0.8, and 0 MV/m respectively). A low moment MFM probe (Nanosensors PPP-LM-MFMR) magnetized along the tip axis was used for imaging. The AFM images in Figure 25b show the presence of ferroelectric domains in the PMN-PT as evidenced by the mottled light and dark regions. The height difference between the neighboring ferroelectric domains (i.e. light and dark areas) is about ± 2 nm. When comparing the four AFM images, one sees that the surface texturing does not change during the application of electric fields (i.e. ferroelectric domains are immobile). Note that the surface topography with a more regular pattern was found in other AFM scanning areas on the PMN-PT sample surface. Since the relationship between surface topography and ferroelectric domains of PMN-PT was previously studied by using piezoresponse force microscopy,[57] it is believed that the surface texture of PMN-PT shown in the AFM images of Figure 25b is partially related to the ferroelectric domains if not totally related.

When reviewing the four MFM images in Figure 25b, notable changes are observed in the magnetic domain structure. In Figure 25b-I at 0MV/m, a typical stripe domain pattern is observed in the Ni thin film as others have reported[38,39]. As the electric field increases to 0.4 MV/m in Figure 25b-II, the stripe domain pattern contrast in the MFM image reduces. At an electric field of 0.8 MV/m in Figure 25b-III, the stripe domains in MFM image are virtually eliminated in the MFM image. The electric-field-induced isotropic compressive strains (see point II and III in Figure 25a) reduce the out-of-plane magnetic stray field suggesting that the magnetization is translating from out-of-plane to prominently in-plane. Upon removal of the electric field (i.e. back to zero strain at point IV in Figure 25a), the stripe domain pattern in Figure 25b-IV is effectively recovered. However, the stripe domain distribution is slightly

different from its original pattern as indicated by the white arrows in Figure 25b-IV. Since surface roughness is known to cause domain wall pinning,[34] the texturing present in the AFM images (i.e. the immobile ferroelectric domain boundaries) is believed to pin the magnetic domain walls and produce a slightly different strip domain structure when compared to Figure 25b-I. When similar MFM tests were conducted on a 100-nm-thick Ni thin film sample, the stripe domain pattern did not change as a function of electric field. Therefore, the reorientation of out-of-plane magnetization in Ni/PMN-PT (001) heterostructure is strongly dependent on Ni thin film thickness.

Figure 26 shows the normalized Kerr rotation versus magnetic field curves (M-H curves) for the 60-nm-thick Ni thin film as a function of electric field measured by magneto-optical Kerr effect (MOKE) magnetometry. Figure 26a shows the polar mode (i.e. out-of-plane magnetization change) and Figure 26b shows the longitudinal mode (i.e. in-plane magnetization change in both x and y directions). In Figure 26a, the polar mode MOKE data shows that the anisotropy field (H_a) increases from ~3700 Oe to ~4200 Oe (i.e. $\Delta H_a \cong 500$ Oe) as the electric field increases from 0 to 0.8 MV/m (see inset for a magnified view). This increase represents an increase of anisotropy energy required to magnetize/saturate the Ni thin film in the out-of-plane direction as an electric field is applied (i.e. the out-of-plane axis becomes "harder"). The longitudinal mode MOKE data in Figure 26b shows that as the electric field is increased from 0 to 0.8 MV/m, the in-plane magnetic remanence increases and the magnetic coercivity decreases in both x and y directions. The increase in remanence represents an increase of in-plane magnetic domain structures (i.e. the in-plane direction becomes "easier") with the application of an electric field while the coercivity reduction may be attributed to a more coherent in-plane magnetic moment rotation during the magnetization reversal process with an electric field applied. The coherent in-plane magnetic moment rotation may be a result of a harder out-of-plane axis when the electric

field is applied (i.e. spins are mainly confined to in-plane directions). Since every in-plane direction is an easy direction, a reduction of coercivity is possible and could represent an explanation of the coercivity reduction with electric field.

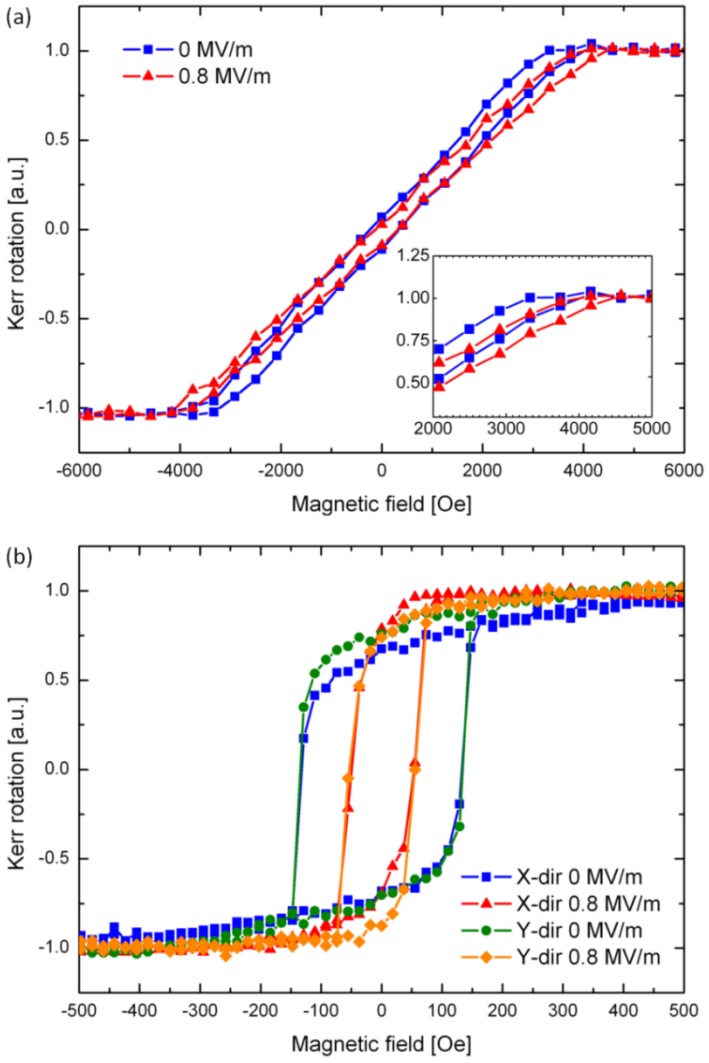

Figure 26: Normalized Kerr rotation hysteresis curves of 60-nm-thick Ni thin film on PMN-PT (001): (a) Polar mode and (b) Longitudinal mode. Inset in (a): Approximate H_a values at different electric fields.

Since the magnetic domain structure in Ni thin film is sensitive to thickness, it is misleading to define the easy and hard axis from simple observations of the M-H curves as pointed out by previous researchers.[38] However, the magnetoelastic change in energy produced by the application of electric-field-induced strain can be analytically calculated and compared to

the magnetic anisotropy change observed in M-H curves as shown in Figure 26. Since Ni is a negative magnetostriction material,[7] isotropic in-plane compressive strains reorient out-of-plane magnetization to in-plane directions. For isotropic in-plane magnetostriction,[34] the magnetoelastic energy change E_{me} can be calculated as: $E_{me} = (-3/2)\,\lambda_s\, E\, \varepsilon \sin^2\theta = 102$ kerg/cm^3, where the magnetostriction constant $\lambda = -34$ and the Young's modules $E = 200$ GPa for Ni,[7] the strain $\varepsilon = 1000$ ppm at 0.8 MV/m (see point III in Figure 25), and θ is the 90° change from out-of-plane to in-plane directions. This energy can be compared to the magnetic anisotropy energy change E_a calculated from Figure 26a: $E_a = (1/2)\,\Delta H_a\, M_s = 109$ kerg/cm^3, where $\Delta H_a = 500$ Oe and the saturation magnetization $M_s = 435$ emu/cm^3 for Ni thin film[36]. One finds that the magnetoelastic energy E_{me} input to the system is very close to the change of magnetic anisotropy energy E_a in the system supporting the described physical mechanism of domain pattern change in the MFM images (i.e. out-of-plane magnetization change).

However, theoretical predictions for a complete reorientation of the out-of-plane easy axis in Ni thin film[55,56] suggest substantially larger strains than the 1000 ppm applied in Figure 25 and Figure 26. These analytical results did not consider the actual domain structure in Ni thin film where the Bloch wall and Néel wall coexist to form magnetic flux closures[37] and may not accurately reflect the experimental results shown in this study. To better explain the discrepancy, illustrations of the domain structure changes (i.e. the change of magnetic flux closure before and after the thin film is strained) along with the corresponding MFM images are provided in Figure 27. Figure 27a shows that before the strain is induced, some magnetic flux exits the sample due to the thickness of the Ni thin film as previously reported.[36,37] The out-of-plane stray fields (i.e. N and S shown in Figure 27a) are sensed with the magnetic probes as shown in the adjacent MFM image (also see Figure 25b-I). While large out-of-plane magnetization components exist, the in-plane domain structure illustrated in Figure 27a is relatively small. Figure 27b shows an

illustration of the domain structure following the application of electric-field-induced strain. As can be seen, the size of the in-plane domains increases and the out-of-plane decreases. The mechanism for the increase of in-plane domains is attributed to an increase of Néel wall area (i.e. solid blue lines in Figure 27) while the Bloch wall area (i.e. dashed red lines in Figure 27) is reduced. Furthermore, as the Néel walls expand, they begin to "cap" the out-of-plane domains (as compared to Figure 27a) significantly reducing the out-of-plane stray field and thus reducing the contrast in the MFM image (also see Figure 25b-III). In addition, since the Bloch wall consists of spins with 180° rotation in the out-of-plane direction, it is also expected that the Bloch walls are also broadening because the spins in Bloch walls tend to stay in the in-plane direction when a strain is induced. As the thickness of the Ni thin film increases (i.e. from 60 to 100 nm), the in-plane domains become less energetically favorable and the energy required to reduce (or broaden) the Bloch walls is larger than that which is available from the PMN-PT substrate (i.e. 1000 ppm). Therefore, for thicker films (e.g. 100 nm), the 1000 ppm is insufficient to dramatically alter the out-of-plane stray fields and thus changes in MFM images were not observed.

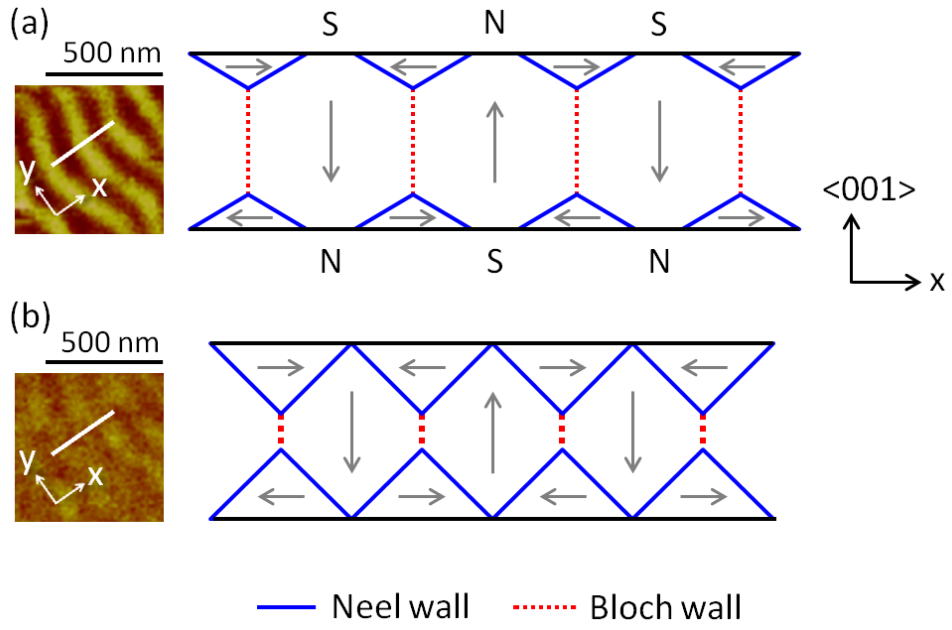

Figure 27: 2-D schematic diagrams of flux closure domain configuration in the cross-section of 60-nm-thick Ni thin film MFM images: (a) zero strain at 0 MV/m and (b) isotropic in-plane compressive strain at 0.8 MV/m. White lines on MFM images represent possible cross-section positions. Gray arrows represent the magnetization direction of each domain: "out-of-plane domains" have arrows pointing to the [001] directions and "in-plane domains" have arrows parallel to the x axis. N and S represent the polarity of stray fields exiting the sample surface.

3.3.1.4 Concluding Remarks

In conclusion, we experimentally demonstrated a partial and reversible out-of-plane magnetization change in Ni thin film through the ME effect in Ni/PMN-PT (001) heterostructure. The stripe domain pattern in 60-nm-thick Ni thin film was eliminated with an isotropic in-plane compressive strain of ~1000 ppm at 0.8 MV/m. A transition from the Bloch wall to Néel wall or the broadening of the Bloch wall, is the mechanism causing the out-of-plane magnetization change in 60-nm-thick Ni thin film. The ability to reorient out-of-plane magnetization is shown to be dependent on Ni thin film thickness.

3.3.2 Reversible and hysteretic domain motion in Ni/ PMN-PT observed by Lorentz TEM

3.3.2.1 Problem Introduction

Magnetoelectric strain-coupled heterostructures are of significant technological interest, particularly for the development of electrically controlled magnetic memory devices such as MRAM.[58,59,60] In these devices the magnetic phase is controlled electrically by a piezoelectric substrate, with interfacial strain playing the role of magneto-electric energy transduction. Of particular interest is the energy transduction between ferroelectric and magnetic domains and the reorientation that occurs at or near their interfaces. While the existence of magnetoelastic coupling in magnetoelectric composites has been widely established[61,62] direct observations of piezoelectrically induced magnetic domain wall motion, especially at the nanoscale, are largely absent. That is, the vast majority of reports focus on macroscopic measurements via SQUID or VSM systems rather than direct observations of domain movements. Measurements of magnetic domain wall evolution in response to a ferroelectric domain state are critical for understanding the role of strain anisotropy, strain gradients, and pinning sites. In addition, observations of magnetoelastically-induced Barkhausen jumps are needed to provide application oriented information to reduce device level magnetic noise, which has recently been associated with irreversible domain wall motion.[63,64] Direct domain wall observations at the nanoscale, particularly in magnetoelectric heterostructures, requires imaging techniques with enhanced spatial resolution and unique magnetic sensing capabilities. In this study, Lorentz Transmission Electron Microscopy (TEM) is used to observe electrically-induced magnetic domain wall motion, at room temperature, on a Ni (magnetostrictive) / PMN-PT (piezoelectric, $Pb(Mg_{1/3}Nb_{2/3})O_3]_{0.68}$-$[PbTiO_3]_{0.32}$ (011)) heterostructure with a back-etched electron transparent observation window. The domain motion is classified as reversible for unipolar electric fields or hysteretic for 180 degree ferroelectric reorientations with several sudden magnetoelastically-

induced Barkhausen jumps. Magnetization gradients are observed in the nickel film and these are shown with COMSOL finite element simulations to be caused by mechanical strain gradients throughout observation window. This work represents the first direct observation of magnetic domain movement using Lorentz-TEM of a magnetoelectric strain-coupled heterostructure consisting of a bulk single crystal piezoelectric substrate.

Many techniques currently exist to observe domain wall motion in magnetoelectric composites such as MFM,[65] MOKE,[66] and PEEM.[67] While some of these techniques are simple, inexpensive, and accessible, others such as PEEM are less accessible. In addition, MFM risks perturbing the magnetization of the sample during measurement while PEEM and MOKE are surface sensitive and/or lack spatial resolution. In contrast, Lorentz TEM has the advantage of a few nanometers spatial resolution and high sensitivity to the in-plane magnetization making the technique ideal to study domain walls such as Néel walls, which are expected in nickel thin films below 60nm.[68] Lorentz imaging in Fresnel mode can be classically understood through the deflection of the electron beam due to the Lorentz force as it passes through a magnetic sample. In the Fresnel method, the image is defocused so that the object plane is no longer in the same plane as the specimen. Depending on the local orientation of the magnetization, the beam deflection direction will vary leading to either enhanced or decreased intensity at areas of varying magnetization (i.e. domain walls). It should be noted that the required defocusing decreases the overall resolution of the technique in comparison to standard bright field TEM and can obscure structural information such as grain boundaries. However, it remains one of the highest resolution magnetic imaging techniques available, with a limit of only a few nanometers.[69] Sample preparation is critical to achieve such high resolution imaging. In particular, the sample must be transparent to electrons and thus the thickness must be less than

100 nm. Fabrication techniques have been demonstrated previously by Brintlinger *et al.* for magnetoelectric Lorentz TEM samples[70] however the limited sample viewing area and the reduced strain output of the thin film piezoelectric in that work made the magnetoelastic origin of the observed magnetic domain evolution unclear. In the present work we have circumvented this issue by utilizing a transparent TEM permeable sample fabricated from a bulk piezoelectric/ magnetic thin film heterostructures to avoid substrate clamping issues. This substantially increases the strain magnitude, observable area, and strain uniformity necessary for a robust multiferroic domain coupling study.

3.3.2.2 **Experimental Setup**

A 35 nm thick polycrystalline nickel film was deposited by evaporation onto a 0.5 mm thick PMN-PT (011) single crystal (Atom Optics, Shanghai) with top and bottom face 50 nm thick Pt electrodes. The planar dimensions of the bulk substrate are approximately 10 mm x10 mm. The sample is cleaved in two separate pieces to create a reentrant side wall with an overhanging film edge as shown schematically in Figure 28a (side view) and with SEM in Figure 28b. Focused ion beam milling with a Ga+ beam source at a 30 kV energy level was used to etch the PMN-PT substrate and release the Ni/Pt multilayer from the backside. After the preliminary bulk ablation of the PMN-PT substrate, currents as low as 1nA were used for high precision milling as well as to minimize collateral damage to the Ni/Pt film. The end result was an electron-transparent observation window roughly 10 x 10 μm. This observation window is seen edge-on in Figure 28c revealing a thickness of approximately 100 nm (35 nm of Ni with some Pt and residual PMN-PT). It should be noted that the thickness of the membrane is non uniform as indicated by the uneven SEM contrast in Figure 28b. Near the edge of the membrane the thickness is approximately 65nm, but this thickness increases to approximately 100 nm near the

center of the membrane. All TEM images were taken using a JEOL 2100F-LM microscope with a specially designed objective pole piece that eliminates the residual Oersted field on the samples.[71] To establish the crystallographic axes of the PMN-PT substrate, necessary for linking the strain direction to changes in magnetic structure, the sample's diffraction pattern was analyzed (Figure 28d). The diffuse ring pattern corresponds to the polycrystalline Ni film; diffraction spots to the single crystal PMN-PT substrate. The real space crystallographic axes of the sample was determined by correcting the intrinsic optical rotation of the microscope between diffraction and imaging mode and is shown in the bright field image in Figure 28e.

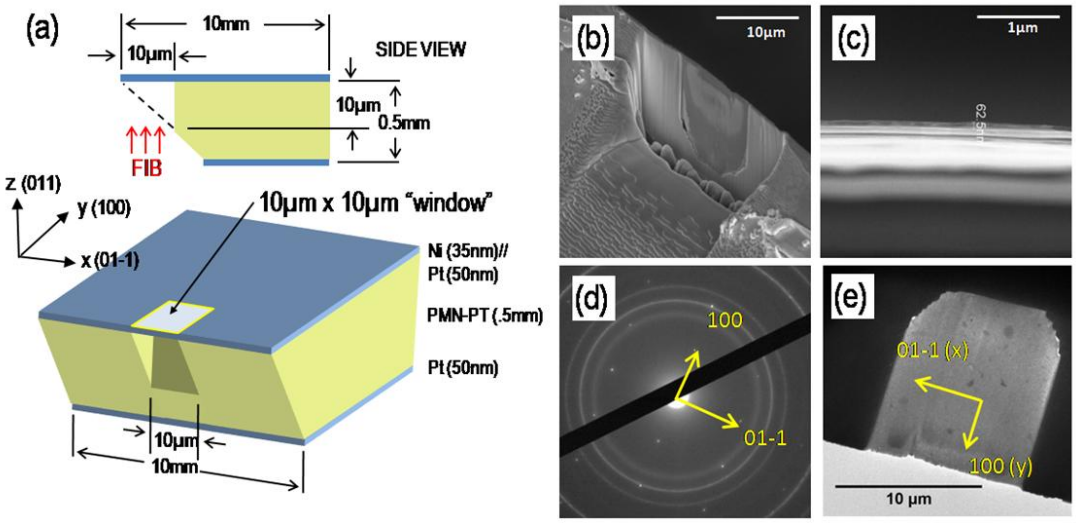

Figure 28: (a.) Sample preparation and geometry details. (b.) SEM micrograph of sample backside showing FIB milled observation window. (c.) SEM micrograph of observation window edge. The window thickness is approximately 100nm. (d.) Experimental diffraction pattern image of the PMN-PT (011) substrate with crystallographic axes indexed. (e.) In focus bright field image of observation window with relevant crystallographic axes indexed.

Single crystal PMN-PT is a popular piezoelectric material in the literature because it has significant and reproducible electric field/strain behavior.[72] The (011) crystal cut has recently received attention because it has large *anisotropic* in-plane remnant poling strain, considerable linear anisotropic piezostrain, and a large non-linear jumping strain during 180 degree

ferroelectric polarization reversal. Figure 29 shows a plot of the strain in each in-plane axis (see Fig. 28e) as well as the anisotropic strain (i.e. $\Delta\varepsilon = \varepsilon_y - \varepsilon_x$) vs. electric field as originally measured by Wu *et al.*[72] The a-h labels in Figure 29 refer to specific strain states/electric fields at which Lorentz images were captured. The magnetoelastic anisotropy in a magnetic film at a given electric field is related to the strain anisotropy by

$$K_{me} = (3/2)\lambda_s E(\Delta\varepsilon)$$

Where λ_s is Ni saturation magnetostriction coefficient (-32 ppm) and E is the Young's modulus of nickel (200×10^9 Pa). The applied electric field creates magnetoelastic anisotropy in the Ni film and reorients the magnetization of the film through rotation, growth, or de-pinning/jumping mechanisms. The amount of magnetization reorientation is related to the magnitude and direction of the applied strain anisotropy, therefore quantification of the strain for this magnetoelastic study is essential. A finite elements model was developed using COMSOL Multiphysics to approximate the non linear electric fields and strain gradients observed around the complex geometry of the10 x 10 μm Ni thin film window. The PMN-PT was modeled as a 0.5 x 0.5 x 0.5 mm element using the piezoelectric module. A 3.5^o slope was removed from one (100) edge to form the overhanging cleaved edge and a 10 x 10 μm slot was cut vertically from the center of the cleaved edge to form the observation window. The materials coefficients were derived from experimental strain gauge measurements.[72] The Ni film on the top surface of the PMN-PT was approximated by a linear shell element. Electric fields between -0.16 and 0.32 MV m^{-1} were applied to the model to match experimental conditions. Figure 30a-c shows a series of calculated strain states corresponding to electric fields a, b, and c in Figure 29. The color plot corresponds to the local strain anisotropy $\Delta\varepsilon = \varepsilon_y - \varepsilon_x$, with darker colors indicating a larger strain anisotropy. Shown schematically with white and black arrows are the strain distribution and local magnetization direction, respectively. A "saddle"-shaped strain gradient is visible at all voltages,

caused by the significant poling induced remnant compression along the (01-1) axis. As shown in Figure 30b and c, the strain gradient within this saddle becomes more pronounced as the electric field is increased. This effect of strain gradient on the local magnetization will be discussed in detail in the next section.

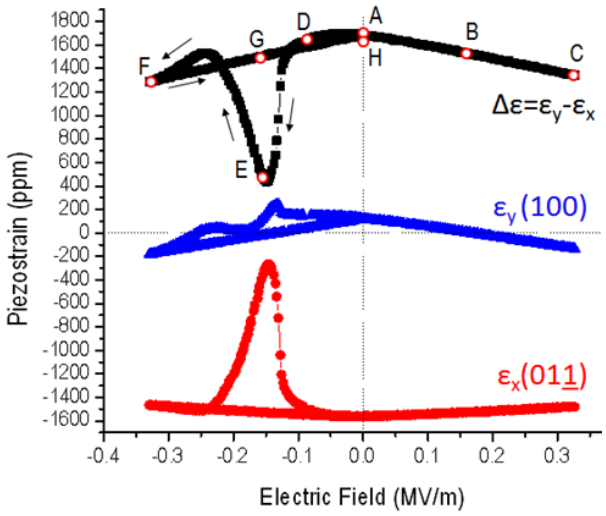

Figure 29: (left) Piezoelectric strain data for the PMN-PT (011) substrate used in this study with specific strain states (A-H) referenced in the main text. Measured by T. Wu *et al.*[72]

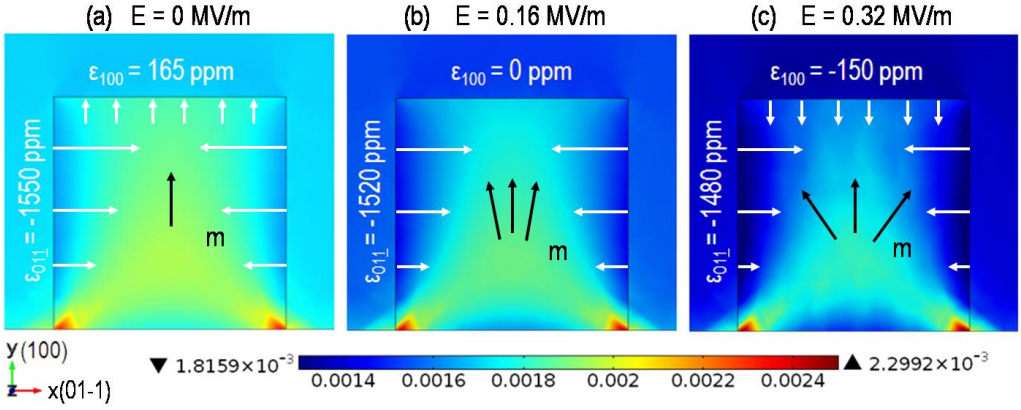

Figure 30: (a-c) Strain gradients in the nickel thin film at various voltages as calculated by COMSOL simulations. Color bar corresponds to strain anisotropy $\Delta\varepsilon = \varepsilon_y - \varepsilon_x$. White and black arrows schematically show strain distribution and magnetization direction, respectively.

3.3.2.3 Experimental Results

The magnetic thin film's response to a unipolar linearly increasing piezostrain is shown in Figure 31 a-d. The light grey rectangular region in Figure 31 is the boundary of the observation window. This region contains a thin membrane of Ni/Pt and trace amounts of PMN-PT, which appear as irregular spotting in the observation window. The edge of the sample is along the lower portion of the image while the vast majority of the substrate continues in all directions above, left, and right of the observation window. The sample is poled prior to imaging in Figure 31a, therefore a substantial poling anisotropic strain of about 1300ppm (point a in Fig. 29 and Figure 30a) is already present in the film, with compression in the x direction ((01-1) axis) and tension in the y direction (100). As can be seen in Figure 31a, the sharp white and black contrast is visible extending parallel to the (100) axis and originating at the junction between the observation window and the bulk substrate along the top of the image. This contrast results from rapidly changing magnetization consistent with the presence of Néel walls. From a classical perspective, the Lorentz force due to the interaction of the beam with the sample's magnetic structure causes local deflections of the beam. At discontinuities in the magnetization (i.e. domain boundaries), this results in either increased or decreased intensity. Furthermore, we see weak line contrast in the area, known as ripple contrast, representing slow change of local magnetization.[63] Magnetization ripples result from the competing interactions of the random crystalline anisotropies due to the multiple grain orientations and the exchange interaction between neighboring grains.[73] Based on the ripple contrast we can determine the local magnetization direction on either side of the domain walls. These directions are marked with arrows in Figure 31a. As the voltage is increased to 80 V (0.16 MV m^{-1}), the tensile strain along the y axis (100) decreases to approximately 0 ppm (point b in Figure 29 and Figure 30b) and the strain along the x (01-1) does not change significantly. This represents a roughly 200 ppm

change in anisotropic strain equivalent to 1.9 kJ m^{-3} of magnetoelastic anisotropy in the film. Looking at Figure 31b, little changes occur in the domain wall configuration as contrasted to Figure 31a, but a ripple pattern begins to form over the entire substrate. The ripple patterns run along the x (01-1) axis, indicating that the local magnetization is aligned perpendicular to these ripples (i.e. along the y (100) axis). This magnetization reorientation arises due to the relative increased compression (i.e. magnetoelastic anisotropy increased) along the (100) and nickel's negative magnetostriction (see Figure 29b). Comparing Figure31b with the COMSOL simulation in Figure 30b, the change in magnetization may be explained by the increased strain gradient in the film relative to the 0V case. In Figure 31c, 160V (0.32 MV m^{-1}) is applied to the substrate equivalent to 150 ppm of compressive strain along the (100) axis (point c in Figure 29 and Figure 30c) and 4 kJ m^{-3} of change in the film's magnetoelastic anisotropy relative to the 0 V state. The domain walls that were immobile in Figure 31b have now de-pinned and a significant Barkhausen jump is visible. Two of the domain walls have combined forming a long chain extending along the (100) direction indicating that magnetization (and domain wall alignment) along the compressive strain direction (100) is preferred. The long white domain wall in Figure 31c is intersected by a dark domain wall which runs along the (01-1) forming a cross tie domain wall at their intersection. The presence of the cross tie in Figure 31c further confirms the prevalence of Néel walls in this film with flux closure predominantly within the plane of the film[74], though it is unclear which of the intersecting domain walls is the primary Néel wall and which is the crossing Bloch line. Interestingly, the domain walls appear to originate at or near imperfections in the film (i.e. the irregular dark spots) which may serve as magnetostatic pinning sites. It is unclear whether these film imperfections are a result of the FIB milling process, which may introduce substrate debris and damage the film, or the sample fabrication process (i.e. the metal evaporation,) which may introduce film impurities. The ripple patterns from Figure 31b

are now broader and more defined; extending in a curving trajectory along the (01-1) implying that a nonlinear strain gradient exists due to the geometry of the observation window. The larger component of magnetization ripples along the (100) direction implies that the magnetization is now reorienting toward the (01-1) axis. Interestingly, the curving trajectory of the magnetization in Figure 31c corresponds well with the finite element simulated strain gradient in Figure 30c. The most significant effect is observed in the center of the window region and this is shown by the simulations to also have the highest strain gradient. Upon removal of the electric field in Figure 31d, the ripple patterns disappear completely and the domain walls return to their original locations (contrast with Figure 31a) indicating that domain wall motion in the unipolar linear regime is a reversible process. At least two additional unipolar electric field cycles were applied to the sample and the domain wall motion in each successive test was reproducible and reversible. The one-to-one correspondence between strain state and magnetization evolution is further evidence of the strong coupling between ferroelectricity and magnetization in this magnetoelectric heterostructure.

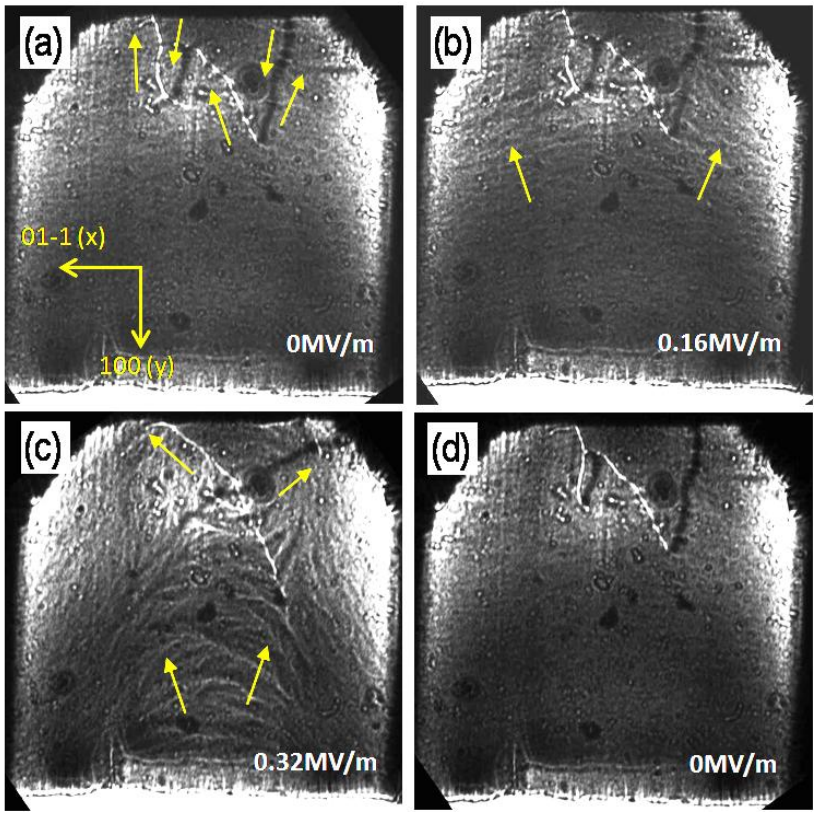

Figure 31: (a-d) Unipolar piezoelectric strain on Nickel thin film/ PMN-PT (011) heterostructure observed with Lorentz TEM corresponding to strain states a-d in Figure 29, respectively. Magnetization of domains are indicated with arrows. (a.) 0 V before applied voltage. (b.) 80V (.16 MV m^{-1}) (c.)160 V (.32 MV m^{-1}). (d.) 0 V.

The heterostructure's response to a bipolar electric field is described next. Figure 32a, d-h is a series of Lorentz TEM images for the heterostructure under six different electric fields (i.e. a to d to e to f to g to h in Figure 29). Going from Figure 32a (point a in Figure 29) to Figure 32b (just prior to the coercive field, -0.08 MV m^{-1}, point d in Figure 29) there is little change in strain state from the PMN-PT and a corresponding lack of magnetic change in Lorentz TEM. The electric field is next decreased to just below the coercive field (-0.08MV m^{-1} point d in Figure 29) in Figure 32d and there is little change in the magnetic image, attributed to a relatively small change in strain state. As the field decreases below the electric coercive field (-0.16MVm^{-1}, point e in Figure 29), the strain anisotropy (i.e. $\Delta\varepsilon = \varepsilon_y - \varepsilon_x$) drops by 1300 ppm with a decrease in

compression along the x axis, as schematically shown in Figure29 point e. Figure 32e reveals at this strain state that two domain walls (indicated by arrow) have vanished and that the film's magnetization state is more uniformly aligned with the (100) compressive direction. The fact that a significant electrically-induced magnetic domain evolution occurred near a large strain jump is further evidence that the observed spin rearrangement is magnetoelastic in origin. As the voltage is decreased to -160 V (-0.32 MV m^{-1} point f in Figure 29), Figure 32f reveals a ripple pattern emerging and crossing domain walls similar to those previously seen in Figure 31c. The anisotropic strain states and magnetoelastic anisotropy produced in Figure 32c and Figure32f are nearly identical as shown by comparing Figure 29, points c and f. This further supports the argument that these magnetic evolutions are due to magnetoelastic anisotropy and not merely ferroelectric switching behavior. Reducing the voltage to -80V (-0.16 MV m^{-1} point g in Figure 29) causes the domain walls to relax in Figure 31g; however two walls remain pinned at an imperfection which is labeled with an arrow. A comparison between Figure 32e and Figure 32g (points e and g in Figure 29) reveals that although both images were taken at the same electric field, the domain wall configuration is different indicating an irreversible magnetic domain evolution produced by a hysteretic ferroelectric states in the PMN-PT. Reducing the electric field completely to 0V in Figure 32h, the magnetic domain walls relax further and return to the same strain state as in Figure 32a. Comparing the domain wall pattern in Figure 32a and Figure 32h indicates that two domain walls have vanished during the ferroelectric polarity reversal, demonstrating hysteretic magnetic irreversibility.

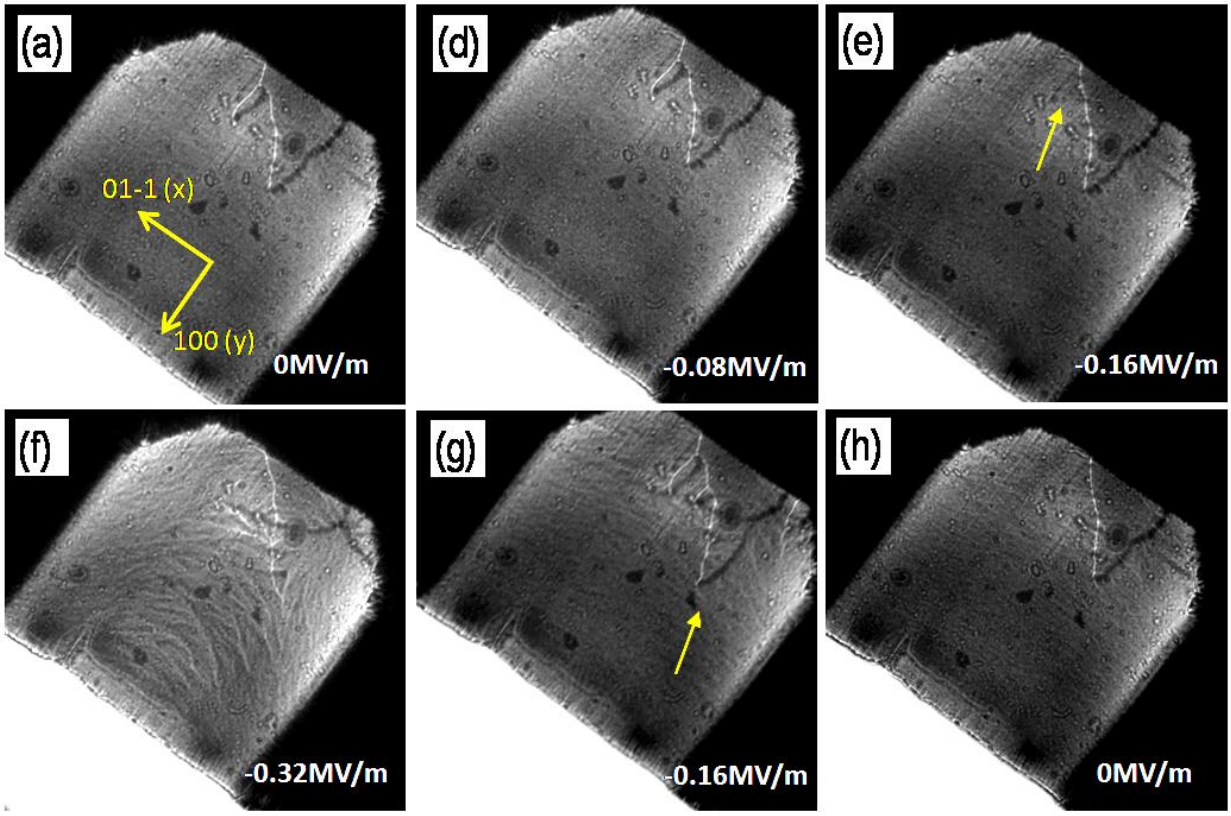

Figure 32: (a, d-h) Reversing electrical polarization procedure on magnetoelectric heterostructure observed in Lorentz TEM corresponding to strain states a, d-h in Figure 29, respectively. (a.) 0V the substrate is pre-poled with a positive electric field. (d.) -40 V, -0.08 MV m^{-1} just prior to the coercive field of the PMN-PT. (e.)-80 V -0.16 MV m^{-1} just after passing the coercive field. (f.) -160 V, -0.32 MV m^{-1}. (g.)-80 V, -0.16 MV m^{-1}. (h.) 0 V, 0 MV m^{-1}.

3.3.2.4 Concluding Remarks

In this paper we have directly measured magnetic domain structures as a function of electric field in a bulk ferroelectric substrate coupled with a nanostructured ferromagnetic thin film. Unipolar electric fields applied linearly increased the magnetoelastic anisotropy in the nickel thin film and caused reversible magnetic domain wall motion and local spin arrangement. However, bipolar electric fields caused a hysteretic polarization reversal in the ferroelectric substrate resulting in non-reversible magnetic domain wall evolutions and Barkhausen jumps in

the magnetic film. COMSOL finite element simulations demonstrate that the observed local spin arrangement follows a saddle-shaped mechanical strain gradient. Domain wall stabilization and pinning sites resulting from film defects were shown to play a critical role in the domain wall reversal behavior. These pinning sites could play a significant role in stabilizing devices based on magnetoelastic coupling and warrant further study. The observation of subtle domain wall phenomena in this study was made possible by the combination of a unique sample structure and Lorentz microscopy which has high sensitivity to in-plane magnetization and excellent spatial resolution. Furthermore, this data provides an important approach to begin more systematic measurements on magnetic reorientation with an electric field necessary for applications such as MRAM.

3.4 Thin Film Concluding Remarks

In this chapter, the influence of magnetoelastic anisotropy on thin film heterostructures was investigated in two experiments. In the first experiment, a 60nm thick Ni thin film heterostructure was fabricated where the magnetization is in a metastable position between in-plane and out-of-plane. This is because as the thickness of the film is increased the out-of-plane magnetostatic energy is increased necessitating the formation of out-of-plane Bloch walls and Neel capping domains. The stress from the 011 PMN-PT substrate creates significant in-plane anisotropy and increases the area of the Neel capping domains, partially eliminating the external flux from the top layer of the film. Thus the magnetization can be controlled between an in-plane and out-of-plane orientation using only electric field. The magnetization rotation is highly stochastic however and the in-plane magnetization morphology cannot be controlled deterministically. In the second experiment, a 35nm Ni thin film is rotated in the plane of the

film by anisotropic stress. This is observed in Lorentz TEM as the reversible motion of Neel domain walls and hysteretic Barkhausen jumps. The applied stress only changes the local morphology of the domain wall and the general magnetization preference, but cannot be considered deterministic control. The advantage of thin film structures over bulk laminates is the greatly reduced magnetostatic energy leading to highly mobile domain walls which can be observed experimentally.

Chapter 4: SINGLE DOMAIN STRUCTURES

4.1 Synopsis

The mechanical control of single domain magnets is explored in this chapter with an emphasis on analytical formulations of the energy landscape. In single domain magnets the magnetostatic energy is decreased to a point where domain wall formation is no longer favorable and shape anisotropy becomes the dominating energy. In this regime the magnetoelastic anisotropy is large enough to deterministically control the magnetization. Three experiments are conducted demonstrating the deterministic control of magnetization in structures of this scale. The first experiment is a proof of concept for the mechanical control of magnets, achieving a full 90° magnetization rotation. The second experiment describes a method to modify the energy landscape of a bit by applying a magnetic field bias along the short axis of the bit. This changes the location of the energy wells creating a situation where the magnetization can be controlled deterministically between two *bistable* positions by a mechanical stress. In the third experiment, an attempt is made to observe the spin structure *within* a single domain bit using Lorentz TEM. Taken as a whole, there three experiments prove the viability of magnetoelastic control in nanostructures once competing anisotropies have been sufficiently reduced.

4.2 Literature Review

4.2.1 Switching field and shape anisotropy

The behavior of all magnetic systems is dictated by magnetostatics and its associated energy minimization behavior. In multidomain elements the individual magnetizations may arrange themselves to maximize flux closure; however this is not an option for single domain

elements. Instead, the magnetization will align itself in a particular way according to the shape and this magnetic preference may be called *shape anisotropy*[7]. This is a particularly important topic in magnetic device research because small differences in device geometry will have a large impact on its magnetic behavior.

Let's consider a single domain element magnetized along its long axis as shown in Figure 33. To satisfy flux conservation across the ends of the element there must be an internal *demagnetization* field (H_d) equal and opposite to the exiting field (H_{ext}). The magnitude of this demagnetization field is dependent on the separation distance of free surfaces, with smaller separation distances having a larger demagnetization field. Single domain magnets naturally favor long-axis magnetization to minimize the demagnetization field and to maximize flux closure within the high-permeability magnetic material. The shape anisotropy is the magnetization preference for a particular direction, proportional to the difference in demagnetization energy all directions. For simple planar elements where the magnetization is assumed to lay in-plane, we only need to consider two orthogonal in-plane demagnetization factors.

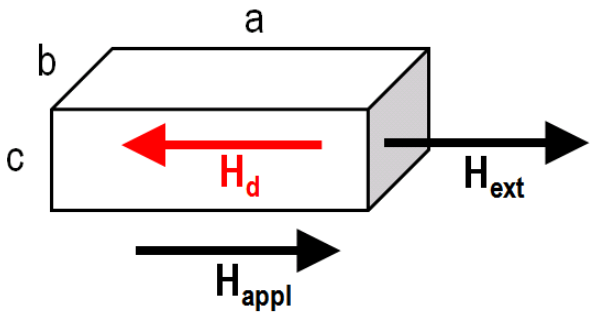

Figure 33: Schematic for shape anisotropy and demagnetization field arising from magnetostatic effects

The total magnetostatic energy in this system assuming uniform magnetization is $u_{ms}=(1/2)H_dM_s$ however this does account for the variance in demagnetization field that comes from real geometries. The shape anisotropy K_{shape} can be calculated using shape anisotropy constants Na Nb and Nc for the case of a 3-dimensional solid. Tables have been created for these shape parameters which are based on the ratio between orthogonal dimensions (e.g. b/a)[75].

$$K_{shape} = \frac{1}{2\mu_0}(N_b - N_a)Ms^2$$

For the special case where the magnetization is confined to in-plane rotation the energy distribution in this system can be expressed as

$$u_{ms} = K_{shape}\sin^2\theta$$

Shape anisotropy does more than determine static magnetization direction; it also determines magnetization switching character. In the quasistatic single domain approximation, magnetic bit switching occurs when the applied external magnetic field (H_{appl}) overcomes the internal demagnetization field. The quantification of this *coercive* field is critical to our understanding of the bit's energy landscape, its 3-dimensional magnetic anisotropy. As stated earlier the demagnetization field is dependent on magnetic geometry, so we may thus expect coercive field to depend on magnet geometry as well. Indeed, as the aspect ratio of the magnet increases, so do the demagnetization field and the coercive field. From this standpoint it is clear that lower aspect ratio structures will have a lower coercive field and smaller switching energy barrier.

Earlier we discussed the contribution of other anisotropies to the switching field of a single domain element. Recall that magnetocrystalline anisotropy, shape anisotropy, and magnetoelastic anisotropy contribute to the total effective anisotropy of an element. From this viewpoint, we may potentially manipulate the switching field of an element by changing the

magnitude of the magnetoelastic anisotropy. This experiment will be demonstrated later in the literature review.

Single domain elements and the Stoner Wohlfarth approximation

If we consider again the MD model we may conjecture about the behavior of just one domain on its own, a *single domain*. Single domains occur when the demagnetization and exchange energy in a particle is not large enough to warrant domain wall formation. In practice, the single domain model is valid for systems as large as 10^{12}-10^{18} atoms, which in physical dimensions is about 500nm[6]. Magnetic flux in single domains is not self-contained as in the MD model so the competing perpendicular magnetic moments found in MD systems is no longer present. Whereas magnetoelastic anisotropy in MD systems caused the growth or decline of one domain over another, we may expect a single domain to respond to stress through *rotation* of the magnetization. This difference in behavior between MD and single domain systems is perhaps the most technologically important emergent magnetic property that arises from a decrease in scale. In recent years single domain particles have been widely studied and now form the basis of magnetic computing hardware such as spin torque transfer (STT) magnetic tunnel junctions (MTJ)[76,77,78,79].

The single domain model was first proposed by Stoner-Wohlfarth (SW) in 1948 and remains today a relevant and instructive model for predicting magnetic behavior at this scale[80]. Using SW we may derive the energy landscape of single domain magnetic particles for arbitrary applied fields and anisotropies and even generate M-H curves and anisotropy or *astroid* plots of these systems[81]. SW is surprisingly simple; the unique assumption being that the single domain can be represented by one spin with a finite angle relative to applied anisotropies. This single

spin reacts to an applied field by rotating, and this is done *coherently*, or as one unit. In reality this assumption is the real weakness of SW because no system has a completely uniform spin structure. SW cannot treat the "s" or "flower" domains that frequently occur in larger single domain elements and for this we must rely on finite element modeling[82]. However, it will be shown later that SW can be adapted for any geometry through the inclusion of shape-induced anisotropy terms. In fact, most anisotropies such as magnetocrystalline and magnetoelastic anisotropy may be included in SW allowing for even the most complex magnetic systems to be modeled. Thus the SW single domain model represents a significant advancement toward our goal of understanding deterministic control of magnetization through magnetoelastic anisotropy.

The following description of the Stoner-Wohlfarth theory is adapted from C. Tannous and J. Gieraltowski[6]. We will first consider the behavior of a single domain's magnetization to an applied magnetic field bias, a relatively simple case, and later in the present work we will include magnetoelastic anisotropy. A convenient representation of single domain particles is a prolate ellipsoid with one dominant uniaxial shape anisotropy K_{uni} parallel with the long axis, as shown in Figure 34.

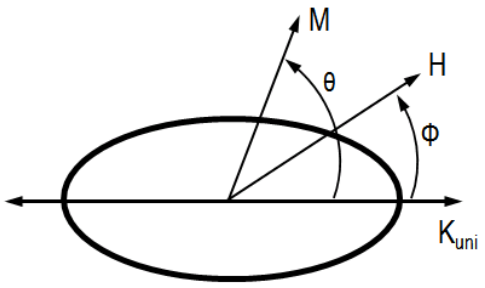

Figure 34 Conventions and symbols for the Stoner Wohlfarth theory as described in this text.

The magnetization M responds to the Zeeman potential energy coming from the applied field H by rotating to the lowest energy position. Thus the two energies in this system are the anisotropy energy E_A and the Zeeman potential E_z which may be described further in terms of the effective anisotropy K_{eff} and the angles θ and Φ between the magnetization and the applied anisotropies.

$$E = E_A + E_Z = K_{eff} \sin^2\theta - M_s H \cos(\theta - \phi)$$

The effective anisotropy K_{eff} can be expanded further to include shape-induced anisotropy K_{shape}, magnetocrystalline anisotropy K_{MC}, and magnetoelastic anisotropy K_{ME}

$$Keff = K_{shape} + K_{MC} + K_{ME}$$

If we assume the special case of in-plane magnetization rotation and that shape anisotropy may be defined by two orthogonal in-plane shape factors N⊥ and $N_{||}$, then we may rewrite Keff taking into account the angular dependence of these anisotropies with respect to the magnetization direction

$$Keff = [2\pi M_s^{\,2}(N_\perp - N_{||}) + K_{MC} + K_{ME}]\sin^2\theta$$

Later it will be shown that K_{MC} and K_{ME} can also be expanded. We may now plot the energy variation or *landscape* of a particle with arbitrary anisotropy $H_k = 2K_{eff}/M_s$ and for varying applied magnetic fields. An example of such a plot is shown in Figure 35 which plots the landscape of a single domain particle with a magnetic field bias of increasing magnitude applied at a fixed angle of 30° from the long axis. We observe that for increasing bias values the energy minima shift locations and in fact only one global energy minimum remains for high fields. We observe that the magnetization rotates to the global minimum in response to the applied field. Interestingly, the height between energy minima, the energy barrier, also changes in magnitude

with applied magnetic field. In other words, applied anisotropies modify the magnetic switching behavior of the single domain particle. This tendency of the energy barrier to shift and transform is an important design consideration for applications relying on low switching energy or, conversely, high stability.

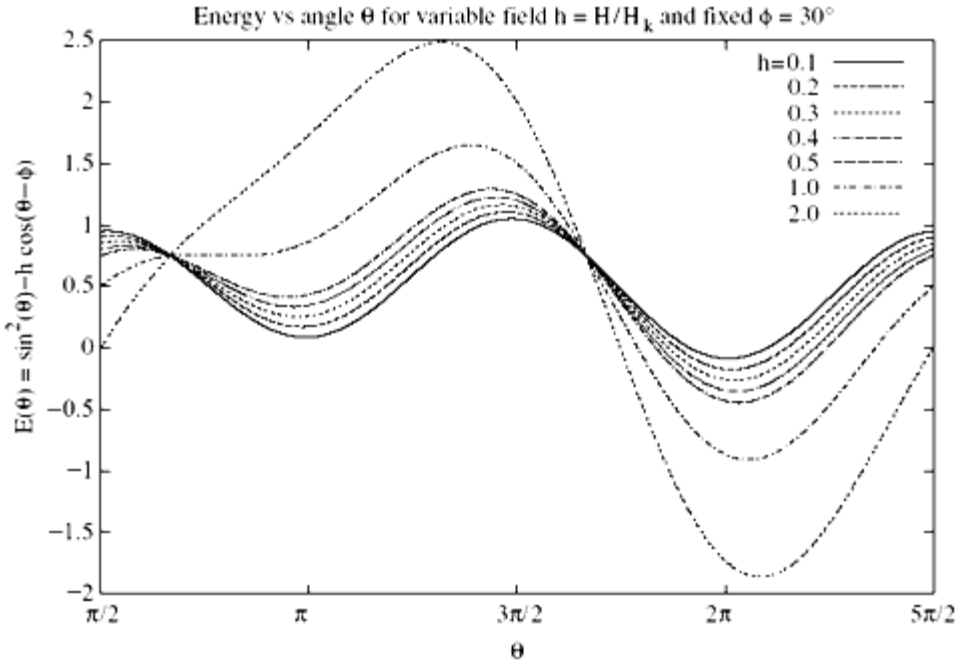

Figure 35: Variation of energy as a function of applied field magnitude for a field bias Φ which is 30° relative to the shape anisotropy. At h=.1 the energy minimum (easy axis) is aligned along the long axis. As the applied field is increased the magnetization rotates and the energy barrier increases dramatically. (from C. Tannous and J. Gieraltowski[6])

4.2.2 Switching field manipulation in 300nm patterned nickel nanostructures

Magnetoelastic anisotropy within the context of single domain elements has been studied only recently. Single domain elements have one dominant magnetization direction, so for convenience such magnets are approximated by a single coherently rotating magnetization vector. This assumption was championed by Stoner-Wohlfarth and the details of these assumptions were mentioned earlier. The affect of magnetoelastic anisotropy on the magnetization of single

domain elements may be quite substantial. An appropriately applied stress may even rotate the single domain magnetization by 90 degrees provided the magnitude of the stress is sufficiently high. One of the very few papers on the magnetoelastic control of single domain elements is by Alexandre Bur *et al.*, which was completed in 2011[83]. In this work they mechanically loaded large arrays of nanostructures and observed clear changes in the magnetic switching behavior of the arrays. However, the magnitude of magnetoelastic anisotropy was not enough to control or rotate the magnetization of the array. Nevertheless, this experiment is noteworthy as it demonstrates mechanical manipulation of nanoscale magnetic single domain elements.

The sample in Bur *et al.*[83] consists of an array of 300x100x35nm^3 rectangular nickel bars on a silicon substrate. As shown in the MFM images of Figure 36, the structures appear single domain as exemplified by the light and dark regions of magnetic contrast. It is important to identify single domain character in the sample to establish that the spins are responding coherently to the applied magnetoelastic anisotropy. The sample is then placed in a 4-point bending apparatus which will load the sample in tension or compression by up to +/- 1200με. The magnetic behavior of the sample is measured by longitudinal MOKE microscopy, sweeping the magnetic field from -700 to +700 Oe. The M-H curve of the array without magnetoelastic anisotropy in Figure 37appears square in shape, with almost 100% remnant magnetization and a coercive field of about 450 Oe. This native coercivity is from magnetostatic anisotropy caused by the shape of the nanobars themselves. Such shape anisotropy is one of the most important design considerations for magnetic devices as it represents a considerable energy factor. The sample is then loaded in compression and the coercive field increases by about 50Oe, maximizing at 500Oe for a compressive strain of 1210με. The magnetoelastic anisotropy in this situation works in conjunction with the shape anisotropy to increase magnetization along the long axis of the bars. Additional magnetic field is required to switch the nanobars and we

observe an increase in coercivity. Finally, the sample is loaded in tension by 1060με and the coercivity of the array decreases to about 380Oe. In this loading condition, the tensile stress counteracts the shape anisotropy which decreases the magnetic preference along the long direction. We observe a decrease in coercivity because less magnetic field is required to switch the array. The conclusion of this paper is that while mechanical manipulation of single domain elements is possible, the shape anisotropy must be reduced significantly if complete magnetization rotation is to be achieved. This may be done by reducing the aspect ratio (i.e. length to width ratio) of the nanostructures or by manipulating the energy barrier as shown in the study by Tiercelin *et al*. Later in the present work, arrays of nanostructures will be revisited and the effect of magnetoelastic anisotropy on smaller aspect ratio structures will be observed.

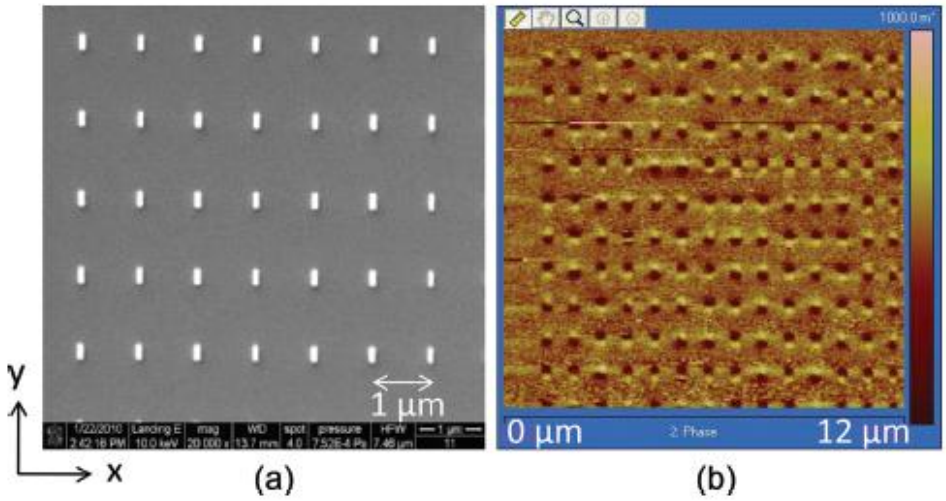

Figure 36: Surface topography of nanobar array imaged by SEM (left) and magnetic response imaged by MFM (right). The MFM clearly demonstrates the single domain behavior of the nanobar array.

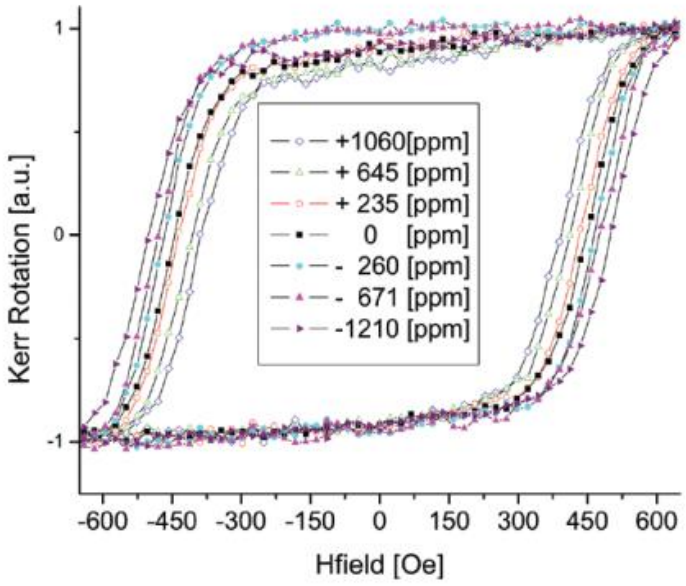

Figure 37: M-H response of nanobar array as a function of applied mechanical strain measured by MOKE magnetometry. MOKE measures a relative change in magnetization.

4.3 Experimental Work

4.3.1 Single domain spin manipulation in strain coupled heterostructures

4.3.1.1 Problem Introduction

The influence of magnetoelastic anisotropy on the magnetic behavior of single domain magnetostrictive elements has been observed directly with PEEM. The geometry of the single domain bit has been selected to minimize the barrier energy while still maintaining thermal energy stability. The magnetoelastic anisotropy this experiment comes from PMN-PT (011) where the magnitude of anisotropy is high enough to overcome the shape anisotropy and induce a 90° planar rotation. A demonstration of this type has important implications as it proves the concept of magnetoelastic control for single domain memory devices.

4.3.1.2 Experimental Setup

The structure consists of an array of 200x100x10nm^3 Nickel ellipses mechanically coupled to a single crystal PMN-PT (011) substrate which exhibits anisotropic strain under applied electric field. As shown schematically in Figure 38, the nanoellipses are arranged into groups of 25 and each group is aligned in one of four directions. Two of the orientations are parallel or anti-parallel to the anisotropic strain field while the remaining two orientations are 45° to the strain field. The nanostructures are aligned in this way in order to study the effect of magnetoelastic anisotropy at 4 different angles relative to the shape-induced easy axis. The entire assembly is then placed in the PEEM under ultra high vacuum where the change in magnetization can be detected by the x-ray circular magnetic dichroism (XMCD-PEEM) technique. This technique detects the direction and magnitude of a magnetized sample relative to an in-plane "axis of sensitivity". The results are displayed as contrast images where the contrast signifies magnetization magnitude parallel to a pre-defined axis of sensitivity.

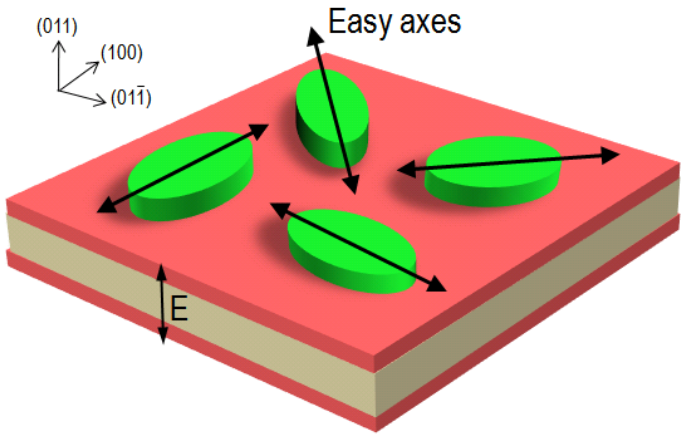

Figure 38: Schematic of single domain nanostructure/PMN-PT heterostructures with rotated easy axes. Each type of single domain structure will behavior differently to the same strain field due to the different orientation of the magnetization relative to the strain.

4.3.1.3 Experimental Results

The results of the experiment demonstrating 90° magnetization rotation in single domain elements is detailed here. A unipolar electric field is first applied to the PMN-PT substrate, increasing from a value of 0MV/m to a final value of 2.7MV/m (135V for the .5mm thick substrate). The XMCD-PEEM images for an array of 25 nanoellipses with the long axis oriented horizontally and the x-ray axis of sensitivity aligned with the long axis is shown in Figure 39A. At 0V, the magnetizations of 9 of these bits are pointing to the left (black dots) while the remaining 16 are pointing to the right (white dots). A color-coded and simplified schematic of this initial magnetization state is shown in Figure 39E. At 50V (.1MV/m, Figure 39B), none of the ellipse magnetizations rotate though the contrast in the black dots decreased slightly. The coercivity of the substrate is 70V and has not yet been reached after the application of 50V. We expect the strain response to be insignificant in Figure 39B which explains the lack of rotation at this voltage. When the voltage is increased to 75V (.15MV/m, Figure 39C), we observe that ten of the 25 ellipses reduce in contrast and disappear from the PEEM contrast image altogether. As shown schematically in Figure 39G, we may interpret the magnetization of the ten ellipses to have rotated 90° and to now point along the hard axis of the ellipse. The magnetoelastic anisotropy has overcome the energy barrier imposed by the shape anisotropy in these bits making the new "easy" axis perpendicular to long axis of the bit. Unfortunately, there are two possible magnetization states which are perpendicular to the long axis and it is not possible to determine which of the two states each bit is in. Magnetoelastic anisotropy is a uniaxial anisotropy and not unidirectional, so the 90° magnetization rotation seen here are not controlled in a completely deterministic manner. Next, the voltage is increased to 135V (2.7MV/m, Figure 39E) and two of the bits switch back to the initial configuration or undergo a 180° rotation. The magnetoelastic anisotropy at this voltage is less than the anisotropy at 75V, so this may explain the reclaimed

magnetization at this state. Another explanation is that random thermal noise is influencing the magnetization rotation now that the switching energy barrier has been reduced by the magnetoelastic anisotropy. The magnetization in this state is at an instability point allowing random thermal fluctuations to switch the magnetization 180°. The upper-right and lower-right bits in Figure 39D underwent a 180° switch from the initial state, possibly due to the combined action of magnetoelastic anisotropy and thermal noise. These results described a qualitative change in image contrast but nonetheless provide the first ever experimental evidence of a deterministically controlled magnetization rotation by magnetoelastic anisotropy. The next section will describe the quantitative analysis of the XMCD-PEEM data.

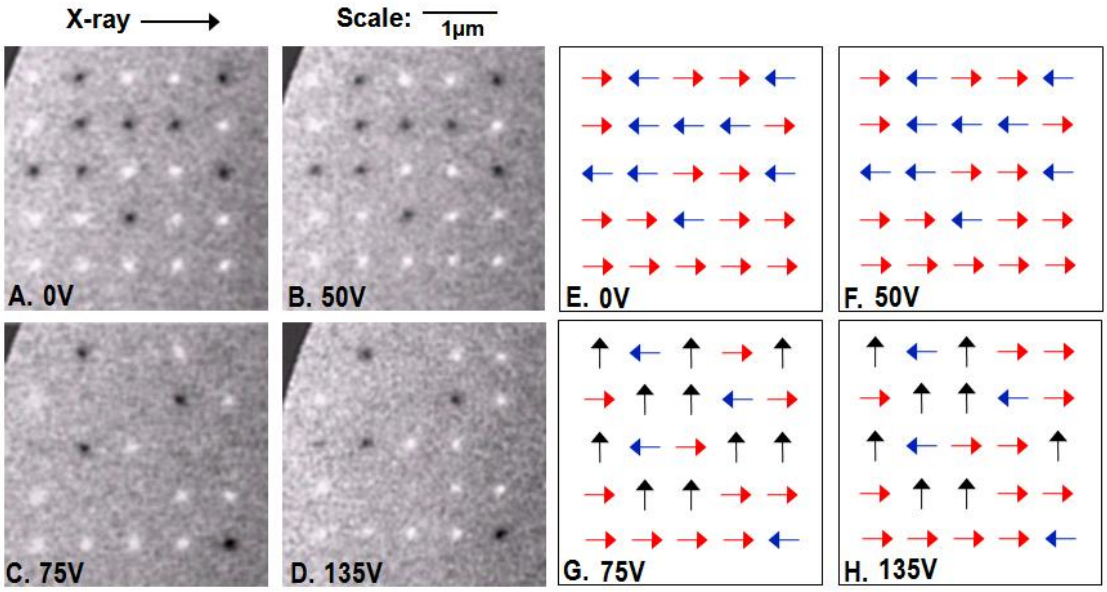

Figure 39: XMCD-PEEM images and magnetization schematics for an array of 200x100x10nm elliptical nanostructures at different applied voltage biases. A., B., C., D., The contrast of individual structures in the XMCD-PEEM image changes drastically upon crossing the electric coercive field value of 70V. E., F., G., H., Possible magnetization configuration based on contrast in A., B., C., and D.

The XMCD of individual pixels may by queried post experiment to yield quantitative data describing magnetization change in individual single domain ellipses. Each pixel in the contrast plots in Figure 39 represents a distance of roughly 30nm. Therefore, an elliptical nanostructure of 200x100nm^2 should occupy roughly 7x3 pixels, providing sufficient data points for XMCD analysis. The XMCD response of selected ellipses as a function of applied electric field (left) and the numbering convention for individual bits (right) are shown in Figure 40. The XMCD magnitude and polarity correlate to the magnetization direction and magnitude of the bits. Each data plot in Figure 40 is related to an individual bit in Figure 40 (right). At 0V, half of the bits are magnetized to the right as evidenced by the initially positive XMCD values varying from .003 to.005. Other bits at 0V are initially magnetized to the left as evidenced by the XMCD values of -.003 to -.005. When the electric field is increased to 70V we observe a rapid decrease in the XMCD value which is consistent with a 90° rotation of the magnetization and the loss of contrast in the PEEM contrast images. The XMCD value of the bits approaches zero with increasing voltage, independent of the initial magnetization direction (left or right). In accordance with classic Stoner-Wohlfarth theory, the bits rotate their magnetization coherently in response to the magnetoelastic anisotropy as evidenced by the solid color of each bit in the contrast images. Curiously, one bit labeled D5.1 in Figure 40 switches 180° as evidenced by the fully reversing XMCD value (from .003 to -.007). This unexpected behavior is likely do to thermal instability as described in the previous section. One obvious benefit of XMCD-PEEM analysis over a large sample size is the capability to make statistical measurements of switching reliability. Additional analysis of the ellipse structures with SEM may yield information about geometry defects which would explain why some bits did not switch.

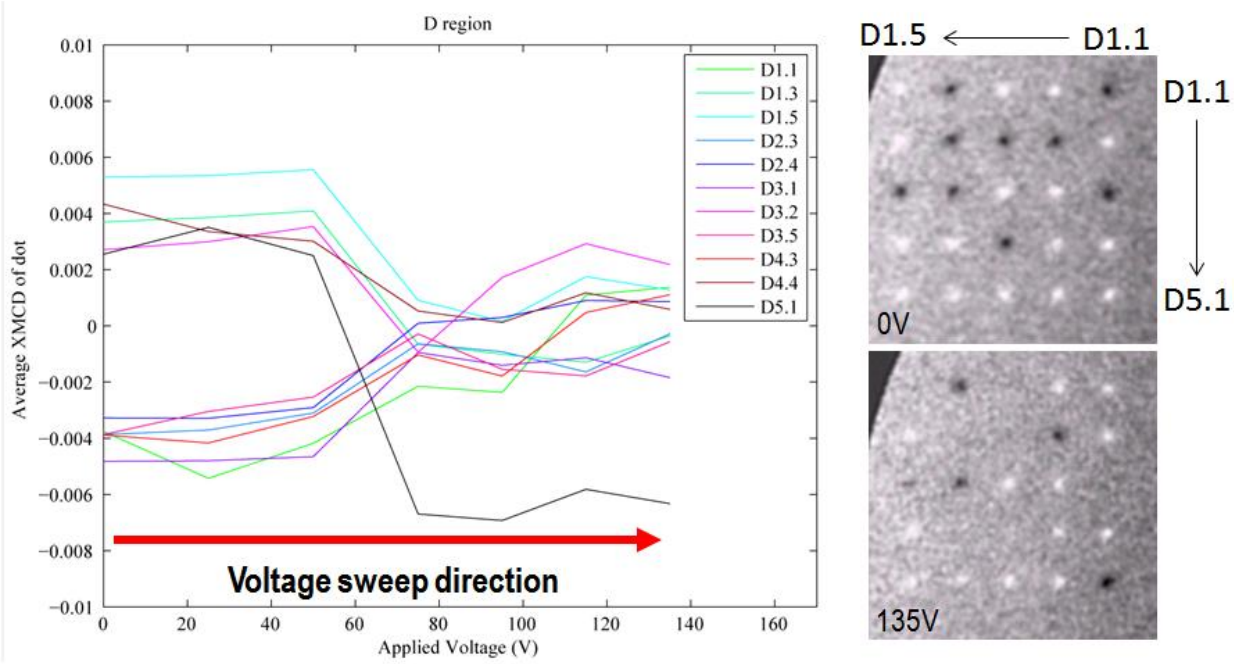

Figure 40: XMCD contrast values for selected elliptical nanostructures as a function of applied electric field showing quantitative evidence of magnetoelastically induced 90° magnetization rotation. The coercive field of the substrate is 70V.

The better understand the role of ferroelectric domains on the strain state of individual bits, piezo force microscopy (PFM) characterization was completed on the un-poled PMN-PT (011) substrate without a top electrode or magnetic bits. Figure 41a is a PFM plot of the substrate showing light and dark regions roughly 1µm wide. These regions correspond to ferroelectric domains with different polarization orientations, either in-plane (dark) or out-of-plane (light.) The ferroelectric substrate in the unpoled state has random polarization, so the polarization state under an individual bit cannot be determined after electrode deposition and prior to poling. Therefore, when the poling process is completed and the final domain state of the ferroelectric is known, the net strain difference between unpoled and poled states is unknown. As shown in Figure 41b, a grain with out-of-plane polarization will experience tensile strain upon crossing the coercive field but will relax and return to a zero strain state upon electric saturation. This

situation may explain why a bit might switch 90° but then return to the un-rotated state as was observed in some bits during the experiment. The possible strain situation is shown in Figure 41c where the bit id deposited on a grain with in-plane polarization. In this case, the bit experiences compressive strain with electric saturation and this is consistent with a one-time 90° rotation which was observed many times in the experimental results. Thus, a model of ferroelectric grain-magnetic bit interaction has been presented which explains why some bits rotate, some rotate twice, and others do not rotate.

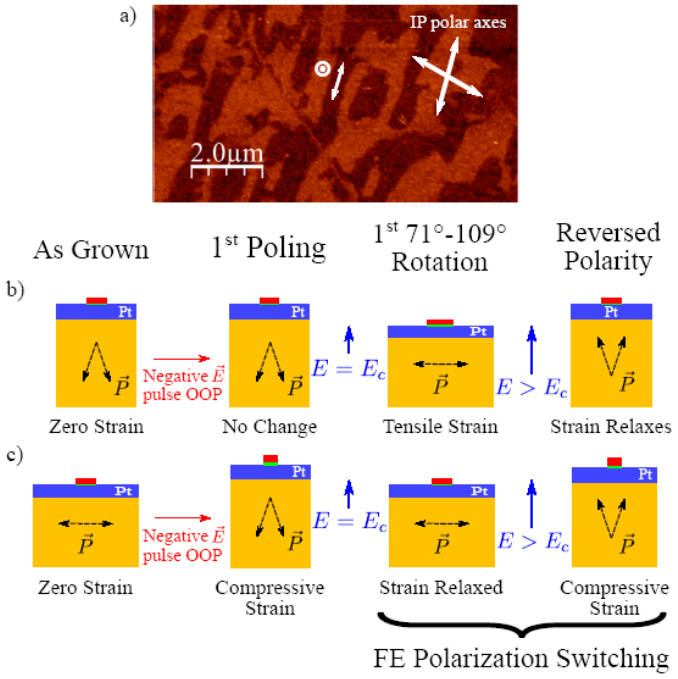

Figure 41: (a) Piezo Force Microscopy (PFM) scan of bulk PMN-PT (011) substrate. (b) model of strain behavior for bit deposited on out-of-plane grain. (c) model of strain behavior for bit deposited on in-plane grain.

4.3.1.4 Concluding Remarks

This experiment provides clear evidence of the coupling between mechanical strain and magnetization in single domain elements through magnetoelastic anisotropy. Additionally, a

model has been presented to relate the ferroelectric polarization of the specific domain under the bit to the final strain state when electric field is applied. The magnetization can been rotated 90° using piezostrain and this level of control is deterministic in that a coherent rotation of the magnetization is accomplished. However, a remaining challenge is developing a process to know the domain structure of the piezoelectric under each bit prior to bit deposition or to set the domain polarizations prior to deposition. Until this problem is addressed complete switching of all bits in an array is unlikely and this prevents device implementation.

4.3.2 Bistable 90° switching in single domain magnetoelectric memory

4.3.2.1 Problem Introduction

Single domain bits have two stable magnetization states which are defined along the long axis by the shape anisotropy and are separated by 180° by the so-called *energy barrier*. The energy landscape of magnetic bits is thus predetermined by the geometry of the bit itself, making physical geometry one of the most important design factors. The work of Nicolas Tiercelin *et al.*[32] demonstrated the use of a magnetic bias field applied perpendicular to the bit's long axis to sculpt the energy landscape by lowering the energy barrier between the stable magnetic states. This was first demonstrated on exchange-biased thin film magnets but has not yet been shown in single domain magnets. A thin film structure does not have a pre-determined magnetization state its behavior under mechanical would be difficult to predict. The advantage of a single domain magnet is that the magnetization is defined by the shape and thus the starting magnetization is known a-priori. It would be an important technical achievement to demonstrate on single domain magnets what Tiercelin *et al.* showed for thin films. This section describes the implementation of a bi-stable 90° switching scheme in a single domain magnet array. As shown in Figure 42-I, the

proposed device structure consists of an array of bits on a single crystal PMN-PT (011) substrate. The bits have two stable magnetization states (defined by the long shape of the bit) as shown schematically with a red arrow. A bias field Hs (but this could also be an exchange biasing layer) is then applied perpendicular to the long axis of the bit as shown in Figure 42-II. This causes the stable magnetic state (the red arrow labeled 'm') to rotate toward the bias field. The magnitude of the bias field should be tuned to position the new stable magnetic states so that they are 90° apart (i.e. the angle between the red arrow and the bias field should be 45°.) Now, if the bit is aligned 45° relative to the anisotropic strain from the substrate as shown in Figure 42-III and IV then the magnetoelastic anisotropy from the substrate can be used to switch the magnetization of the bit by 90°. In this case, the additional magnetic anisotropy from the applied mechanical strain contributes to the total energy landscape of the structure, creating a new preferred magnetization direction. The magnetization is bi-stable (with 90° well separation) at zero applied electric field because there is a co-existence of a global energy well at the same location as the applied mechanical strain. A key feature of this system to point out is that the height of the energy barrier can be controlled in two ways: firstly, the shape (i.e. the aspect ratio) of the bit determines the starting height between the 180° energy wells. This is important for thermal stability of the bit but also to avoid an unnecessarily large energy barrier. Secondly, the applied magnetic field bias (or exchange bias layer) can be tuned to control the separation angle and height of the energy barrier between stable states. This single domain device structure represents an improvement on the 90° switching devices where the strain is applied perpendicular to the long axis (i.e. the PEEM tests in the previous section) because the direction of magnetization rotation can now be controlled deterministically, as opposed to random 90° rotations.

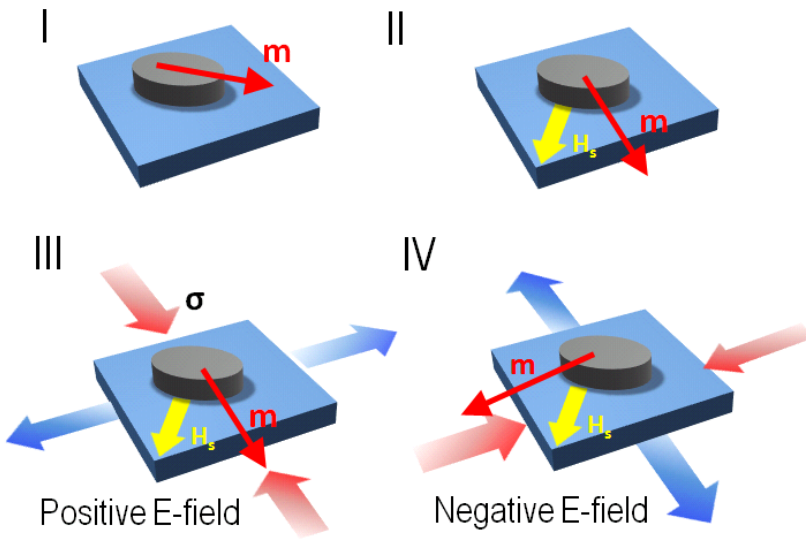

Figure 42: Schematic of experimental procedure for energy barrier manipulation experiment. I. Elliptical nanostructure has magnetization m predefined by shape anisotropy. II. Magnetic field bias Hs is applied perpendicular to native shape anisotropy. III. Magnetoelastic anisotropy is applied to switch magnetization 90° to state IV. Switching between III and IV can be repeated.

To demonstrate analytically the device concept, a formulation was developed based on Stoner-Wohlfarth single domain theory to compute the energy landscape of a single domain ellipse with shape anisotropy, magnetoelastic anisotropy, and Zeeman potential. The full form of this energy equation is

$$E = K_{Zeeman} + K_{shape} + K_{Magnetoelastic}$$

Which, when expanded is

$$E = -\mu M_s H_s \cos(\phi) - \frac{1}{2}\mu M_s H_a \sin(\theta) + \frac{3}{4}\lambda_s \sigma \sin(2\theta)$$

Where H_s is the bias magnetic field value in A/m and H_a is the shape anisotropy in A/m (but is also sometimes written as $M_s(N_a\text{-}N_c)$ where N_a and N_c are the so-called shape factors.) This model assumes a perfect prolate ellipse structure with perfect collinear magnetization alignment, a length of 200nm, a width of 100nm, and a thickness of 35nm. The magnitude of the shape

anisotropy magnitude is determined from the geometry of the ellipsoid and was calculated previously by Osborn[84] and Ahoroni.[85,86,87] The magnetoelastic anisotropy is assumed to be +/- 700με applied 45 degrees to the long axis as shown schematically in Figure 42-III and IV. This value corresponds to the maximum applied strain from the PMN-PT substrate in the half-poled case as measured by experiment. The Zeeman potential (bias field) was assumed to be 260 Oe, and this value was tuned manually until the energy wells positioned 90° apart. A plot of the energy landscape as a function of angle for the single domain ellipse (without magnetoelastic anisotropy applied) and the schematic of terms and definitions is shown in Figure 43. The shape anisotropy defines two energy wells (the energy minimums) at +/- 90° (i.e. along the long axis). The field bias is applied perpendicular to the long axis which on its own forms a single energy well at 0° (i.e. along the hard axis). The combined action of these two energies forms two new energy wells at +/-45° as shown in the blue line in Figure 43. The two energy wells are equivalent and the stability parameter[88] between them (a measure of thermal stability) is ~200E_b/kT.

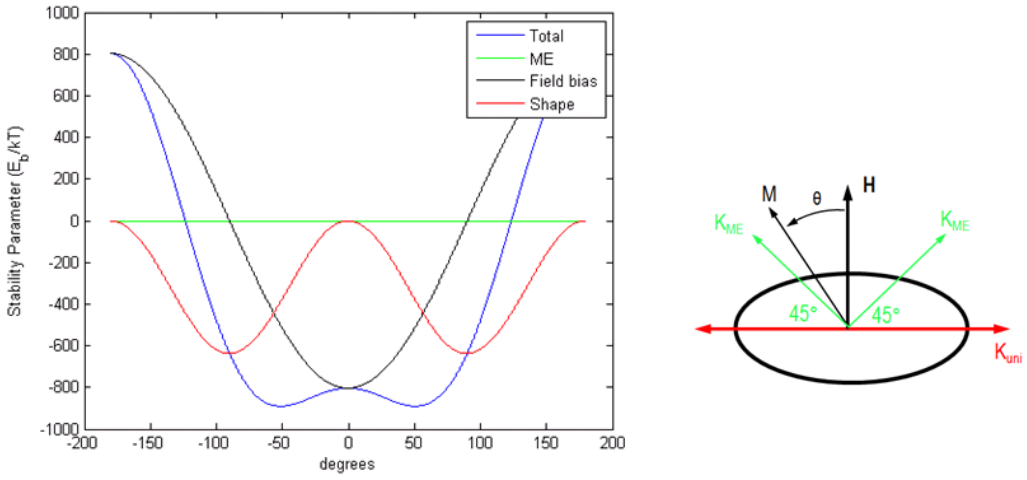

Figure 43: Energy landscape (left) of a 200x100x35nm elliptical nanostructure with field bias of 260Oe applied along the hard axis at Φ=90°. Coordinate system for this analysis. The applied bias creates two energy wells at θ=-45° and θ=+45° in the blue total energy plot.

As stated earlier, the height of the energy barrier as well as the separation angle between the energy wells can be controlled by tuning the magnitude of the applied bias field. Figure 44 is a plot of the energy well separation angle (left) and the normalized barrier height (right) as a function of the applied bias magnetic field normalized to the uniaxial anisotropy K_u. At zero applied bias field, the energy well separation is 180° (i.e. wells predetermined by the shape anisotropy) and the barrier height E/K_u is 1 (i.e. the barrier height E is simple the uniaxial anisotropy K_u.) As the bias field is increased to equal the K_u (i.e. $h_{bias}/K_u = 1$) the barrier separation angle is still roughly 120° and the barrier height is approximately 25% of the original barrier energy. At the critical bias field of $h_{bias} = \sqrt{2}K_u$ the angle between the energy wells is 90° and the energy barrier is just 7% of the original uniaxial anisotropy. The 90° separation arrangement is ideal for the 90° magnetoelastic switching scheme, but we can imagine other systems with higher magnetic bias fields that have smaller energy well separation and smaller barrier height.

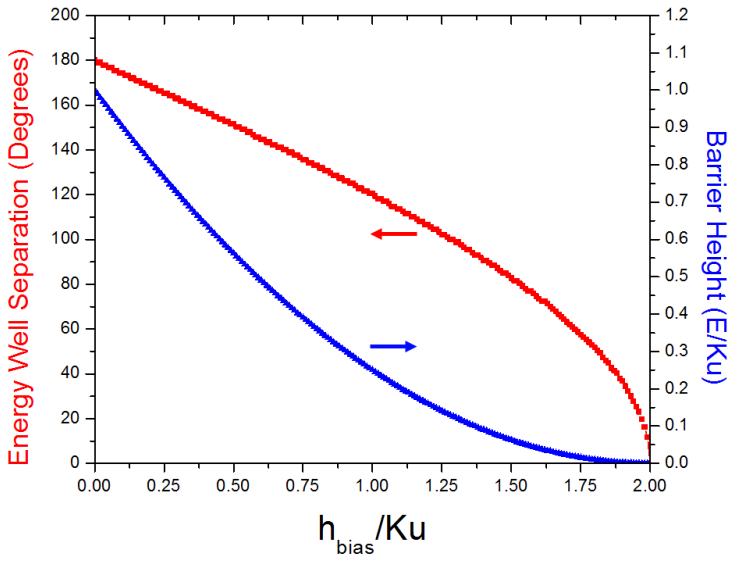

Figure 44: Plot of energy well separation angle (left) and normalized barrier height (right) as a function of applied bias magnetic field normalized to the shape anisotropy (Ku)

Next, the influence of magnetoelastic anisotropy is included in the analytical formulation. A positive strain field of 700 με is applied and the results of the calculation are shown in Figure 45. The magnetoelastic anisotropy is rotated 45° relative to the long axis of the bit, as shown by the green line (i.e. total with ME anisotropy) plot. The combined action of the magnetoelastic anisotropy with the shape and Zeeman energies results in one global minimum energy state (i.e. the blue line with the minimum at +45°.) Thus the magnetoelastic anisotropy deterministically defined a single magnetization direction and a clockwise rotation toward +45°.

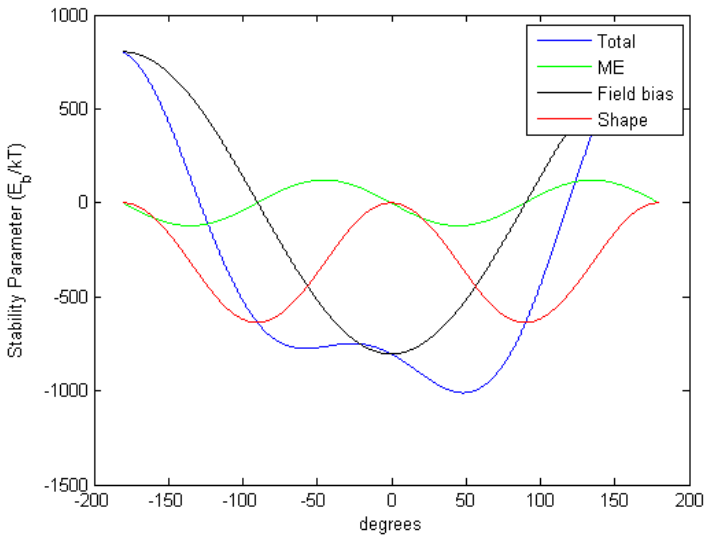

Figure 45: Energy plot of the elliptical nanostructure with applied magnetoelastic anisotropy at +45 degrees relative to the long axis of the bit. This creates a single global energy minimum at θ=+45°.

The polarity of the strain field can now be reversed to -700 με as shown in Figure 46, forming one global minimum energy 90° from the minimum defined by the +700 με case (i.e. the blue line with the minimum at -45°.) The magnetization may be switched repeatedly between the energy minimums in Figure 45 and Figure 46 (i.e. from +45° to -45°) by controlling the strain

anisotropy and thus the applied electric field polarity to a ferroelectric. Experimental efforts to demonstrate this switching scheme will be detailed next.

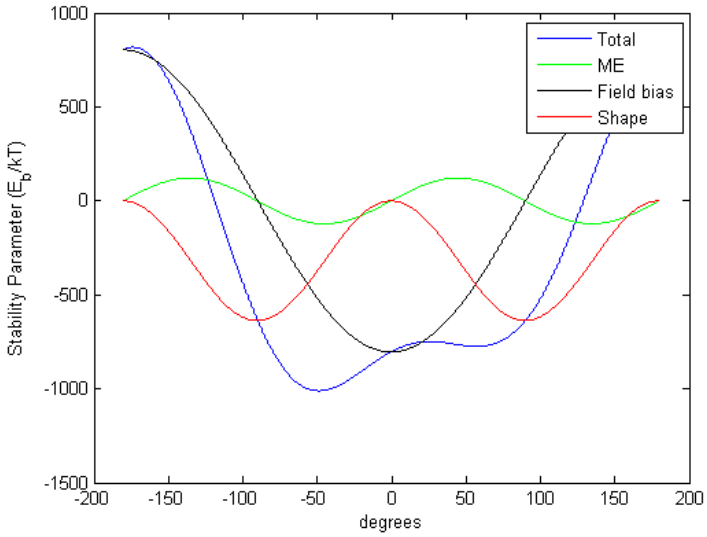

Figure 46: Energy plot of the elliptical nanostructure with applied magnetoelastic anisotropy at -45 degrees relative to the long axis of the bit. This creates a single global energy minimum at θ=-45°. Total magnetic switching of 90° degrees is accomplished between the two energy wells by reversing the polarity of magnetoelastic anisotropy.

4.3.2.2 Experimental Setup

To study the switching behavior of magnetic bits under applied magnetoelastic anisotropy, multiple arrays of 35nm thick nickel single domain bits were deposited onto a single crystal piezoelectric PMN-PT (011) substrate using the e-beam/lift off process. Figure 47a shows an SEM micrograph of three of the patterned arrays; each array is patterned with excellent geometric regularity. A total of nine arrays were created, each with a unique in-plane elliptical or rectangular geometry. The magnetic response of the bits was measured by MOKE magnetometry, necessitating a fairly large array of 2000x2000 bits in each array- an area of roughly 1mm^2. The M-H response of selected bit arrays is shown in Figure 47b and 1c. Figure 47b demonstrates the

dependence of the switching field on elliptical bits of increasing aspect ratio. As the length of the bit array increases from 150nm to 300nm, the switching field increases from 175Oe to 300Oe, respectfully. This is explained by the corresponding increase of magnetostatic shape anisotropy with increasing bit aspect ratio. It can be deduced that the energy barrier and therefore magnetoelastic anisotropy required for switching is significantly higher for larger aspect ratios. It is expected that a breakdown in single domain behavior should occur at some critical aspect ratio or volume. To demonstrate this behavior, Figure 47c plots the M-H response of 300nm long bits of increasing width. As the width increases from 100nm to 150nm, the switching field decreases from 300Oe to 225Oe. The difference in demagnetization energy between two orthogonal in-plane directions is lower for the case of the 300x150nm bit than the 300x100nm bit, reducing the shape anisotropy. Most telling is the M-H response of the 300x200nm bit array, whose switching field reduced to 100Oe and in-plane remanence reduced to nearly 75%. The reduced remanence at zero field hints at a multidomain bit typified by incoherent magnetization rotation. While ME-cell induced switching may be easier for this geometry than for other aspect ratios, the deviation from single domain behavior may not be desirable for read methods such as STT.

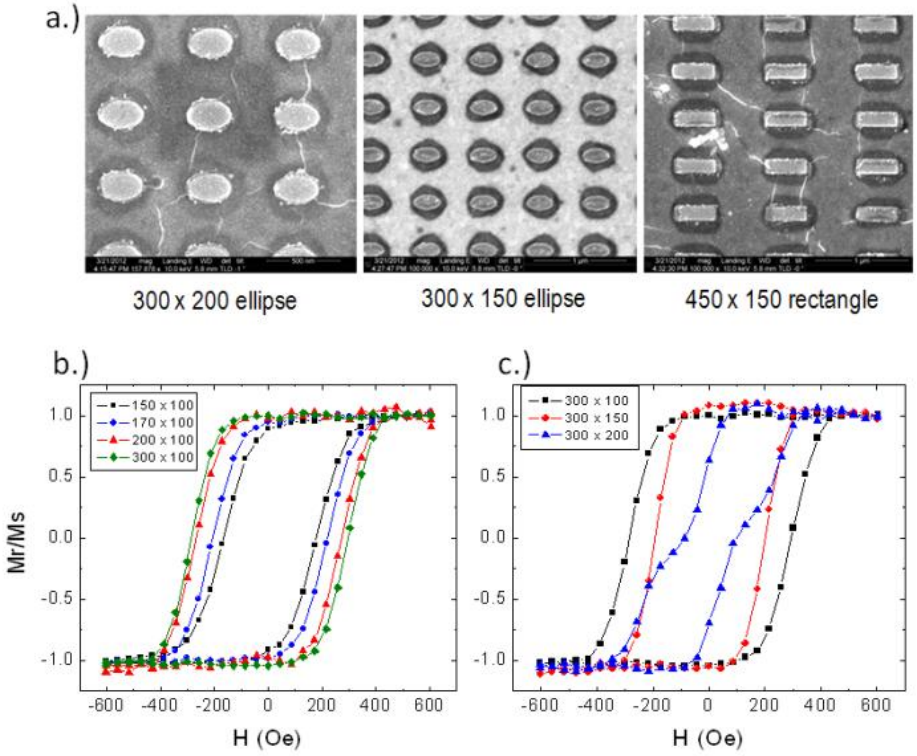

Figure 47: (a.) SEM micrographs of 35nm thick single domain nanostructure arrays, dimensions given in nanometers. (b.) and (c.) M-H response of single domain elliptical nickel nanostructures with various aspect ratios, generated by longitudinal MOKE

From Figure 47 it is deduced that the 150x100x35nm geometry has the smallest switching field and thus the smallest initial energy barrier. This geometry was selected for further testing because of the likelihood that it can be switched magnetoelastically. As shown in Figure 48 A is schematic of the device structure which consists of three ellipse arrays on a piezoelectric PMN-PT (011) substrate. The bits are oriented with their long axis 0°, 90°, and 45° to the applied magnetoelastic anisotropy (i.e. the compressive and tensile stress directions) as shown in Figure 48C to study the affect of the same stress anisotropy applied at different angles. An SEM image of the bit array is shown in Figure 48 B showing that the bits are separated by 500 nm to mitigate magnetostatic interaction between bits.

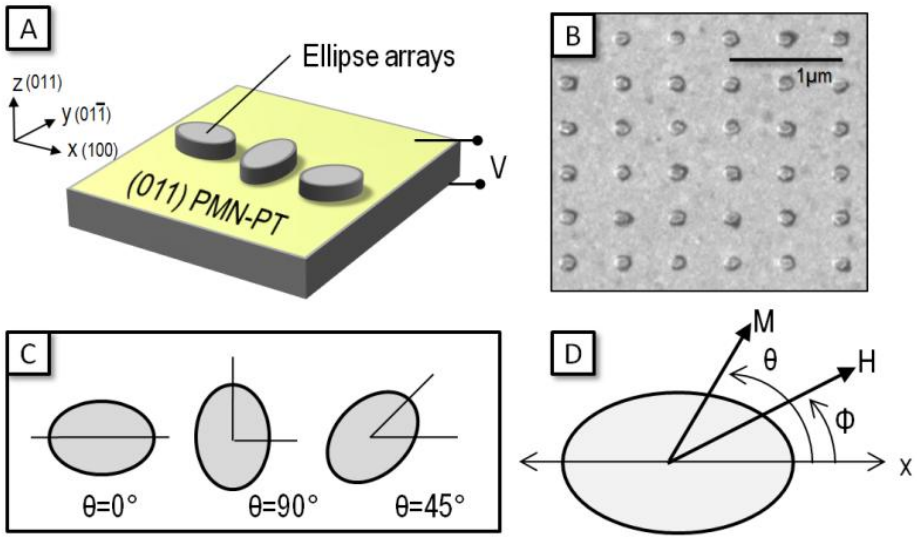

Figure 48: (a) Schematic of 150nm x 100nm x 35nm single domain/PMN-PT (011) magnetoelectric heterostructure. (b) SEM micrograph of single domain array. (c) Top view schematic of the array orientations. (d) Coordinate system for this experiment.

4.3.2.3 Experimental Results

To confirm the influence of magnetoelastic anisotropy on the complete energy landscape of a magnetic bit, voltage was applied to the magnetoelectric structure while measuring the switching field at multiple in-plane angles. Figure 49a shows a set of M-H curves for the single domain array in three strain states: with no stress, with compression along the long axis, and with compression along the short axis. At zero stress (black line labeled 'unpoled') the switching field of the ellipses is approximately 200 Oe. An electric field of 0.8MV/m is then applied to the substrate to pole it, generating significant in-plane magnetoelastic anisotropy. The electric field is returned to 0 MV/m for the MOKE measurement so only the remnant stress is present in the bits. As shown by the red line in Figure 49a, the coercivity of the ellipse increases to approximately 250 Oe when the compression stress is along the long axis. In this instance, the magnetoelastic anisotropy is added to the native shape anisotropy of the bit, resulting in a larger

uniaxial anisotropy and a larger switching magnetic field (as compared with the zero stress state.) The blue line in Figure 49a shows the response of the ellipses to a stress applied along the short axis of the bits. In this case, the magnetoelastic anisotropy goes *against* the native shape anisotropy and the result is a smaller coercivity. One interpretation of this result can be understood within the context of the analytical formulations and plots as described in the previous section. We may think of the mechanical stress controlling the height of the energy barrier and thus influencing the switching field.

To gain a full understanding of the stress's influence on the switching field, it is necessary to measure the switching field at all in-plane angles. The switching field (or generally the *anisotropic field*, Ha) is then plotted as a function of angle and the resulting plot is the *Stoner Astroid* in Figure 49b. In this experiment the anisotropic field was measured every 10° with each data point representing an average of 50 measurements by MOKE. The black, red, and blue curves correspond to the zero stress, stress applied along the long axis, and stress applied along the short axis states, respectively. From the zero stress black line, we see that the highest switching field occurs at $\theta=0°$ and $\theta=90°$ with a minimum at $\theta=45°$ and $\theta=135°$. For the red and blue lines we see the anisotropic field Ha increase and decrease for all angles relative to the zero stress case, respectively. From this result we may conclude that the ellipse array has a uniaxial anisotropy coming from the shape anisotropy and more importantly that the ellipse array responds to the applied stress coherently by globally increasing or decreasing the switching field (i.e. a non-coherent magnetization evolution was not observed.) The stress thus affects single domain structures by changing the complete energy landscape of the bit.

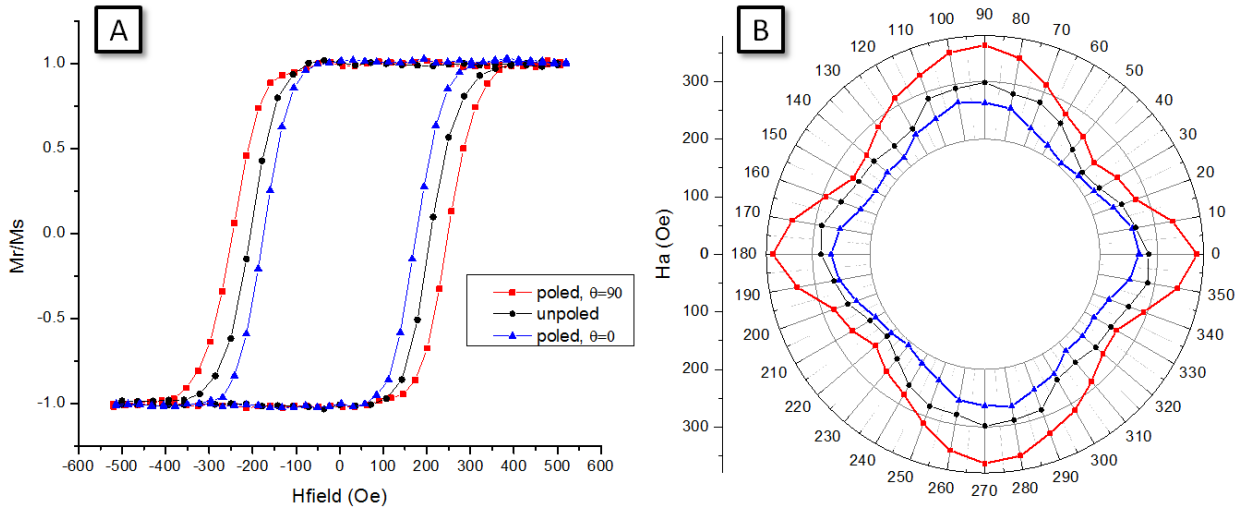

Figure 49: (a) MOKE M-H plot of 150x100x35nm^3 ellipse array with and without strain, with compressive strain along the long or short axis of the bit. (b) Stoner-Wohlfarth astroid of the magnetoelectric strain-coupled ellipse array under the same loading conditions as (a).

Next, the influence of stress when applied at 45° relative to the long axis of the bit is studied next which is of particular importance for the proposed bistable 90° switching device. Figure 50 is an astroid plot of the anisotropic field for an ellipse with no stress and for stress applied along θ=45°. For the case where stress is applied we see that the anisotropic field increases in some directions but decreases in others. At θ=45° the anisotropic field increased by approximately 50 Oe while at θ=135° the anisotropic field decreased by 50 Oe. In fact, the entire astroid appears to have rotated counterclockwise indicating that a coherent rotation of the magnetization occurred. The important thing to note is that the magnetization rotated deterministically toward one energy well, specifically the compressive direction along θ=135°. A complete rotation was not accomplished possibly because the strain magnitude from the substrate was not high enough but nevertheless the concept of deterministic rotation toward a single energy well has been demonstrated.

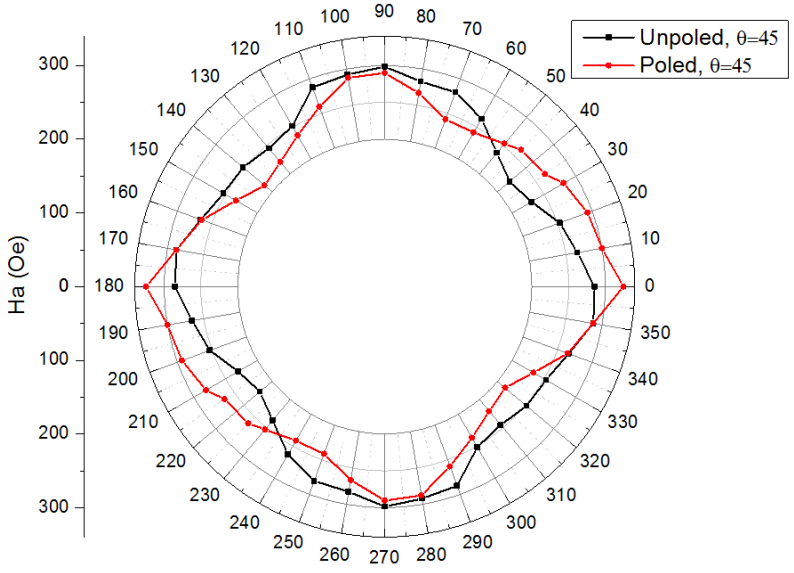

Figure 50: Stoner Astroid of single domain ellipse array with zero stress and for stress applied at 45° relative to the long axis.

4.3.2.4 Concluding Remarks

In this section, a bistable 90° deterministically switchable single domain magnetoelectric heterostructure was analyzed. Analytical formulations indicated that an applied magnetic field bias could theoretically lower the energy barrier enough to enable deterministic magnetoelastic switching by mechanical stress from a piezoelectric substrate. The height and angle of the barrier between the stable energy wells can be controlled by the geometry of the bit and the applied magnetic field bias. An experiment was conducted consisting of a large array of single domain magnets strain coupled to a piezoelectric substrate. Mechanical strain from the piezoelectric substrate influenced the switching field and also the global energy landscape of the bit, though complete switching was not accomplished. The off-axis stress applied at 45° and 135° showed evidence of coherent deterministic rotation toward a single energy well. In future experiments, the addition of a bias magnetic field applied along the short axis may lower the energy barrier significantly allowing the magnetoelastic anisotropy to dominate.

4.3.3 Spin manipulation in single domain observed by Lorentz microscopy

4.3.3.1 Problem Introduction

In our past work we demonstrated on thin film magnetoelectric structures that it is possible to control the magnetization of said films electrically. However, measuring this effect on nanoscale structures is a considerably more difficult task requiring sophisticated measurement techniques. In the previous section, efforts to measure nanoscale magnetization rotation using XMCD PEEM imaging were details. Although these results quantitatively demonstrated 90° switching in single domain ellipses, this experiment lacks spatial resolution making a spin-level observation of the magnetoelastic coupling effect impossible. For this reason we began collaborating with the Brookhaven National Laboratory to undertake TEM Lorentz microscopy measurements.

4.3.3.2 Experimental Setup

Transmission Electron Microscopy (TEM) with Lorentz Effect imaging works by detecting the rotation of transmitted electrons through a magnetic material. The highest spatial resolution and magnetic contrast can be achieved with this method, however the sample requires special preparation. The sample must be quite thin (less than 100nm) and this presents a challenge for our magnetoelectric structure which consists of magnetic nanostructures on a .5mm thick PMN-PT substrate. As shown in the schematic in

Figure **51**, a magnetoelectric sample was designed specifically for TEM imaging. The main feature of this design is a “viewing window” which is a thinned section of the bulk substrate made by Focused Ion Beam milling. The thickness of this viewing window is about 100nm thick.

Nanostructures may by fabricated on the top surface of this viewing window making it possible to use TEM Lorentz microscopy on nanostructure arrays.

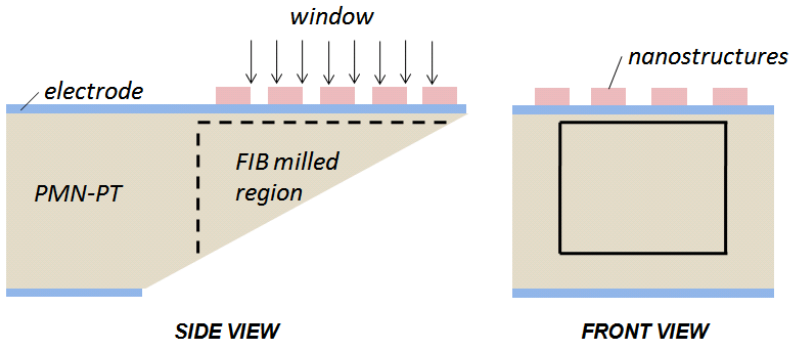

Figure 51: Schematic of Magnetoelectric TEM sample with Nickel nanostructures on PFIB machined MN-PT, Side and Front views.

4.3.3.3 Experimental Results

Figure 52 (left) is an SEM micrograph of the completed TEM sample viewed from below. The thin viewing window is visible as a dark sheet in the upper left. Figure 52 (right) is an SEM micrograph of the top surface of this viewing window. On the top surface of the window we have fabricated an array of 200x100x35nm^3 nano-ellipses. Other array geometries have also been fabricated, such as 150x100nm ellipses. These nanostructures are strain-coupled to the PMN-PT (011) substrate. It must be noted that the crystallographic structure of the underlying substrate material may also be examined in TEM, enabling direct observation of the substrate lattice-to-nanostructure strain coupling phenomenon. Figure 53 is an in-focus brightfield image of one of the bits demonstrating the high resolution of this observation technique. Note the crystalline structures which are grains in the metal electrode layer and remaining PMN-PT substrate. The magnetic bit itself is the oblong black structure which is invisible due to its thickness and the thickness of the substrate. In other words, the observation window was not milled thin enough o

permit magnetic observations in this sample. This may also be due to the decreased saturation magnetization of the elementally pure nickel in this magnetic bit. Future samples with reduced window thickness may permit a spin-level experimental observation of magnetic reorientation within a patterned nanostructure. Such an observation may yield information about strain coupling in the nanoscale, such as shear lag and other non-linear strain effects. This information will prove invaluable for any application requiring magnetoelastic coupling, such as spin wave ME-cells.

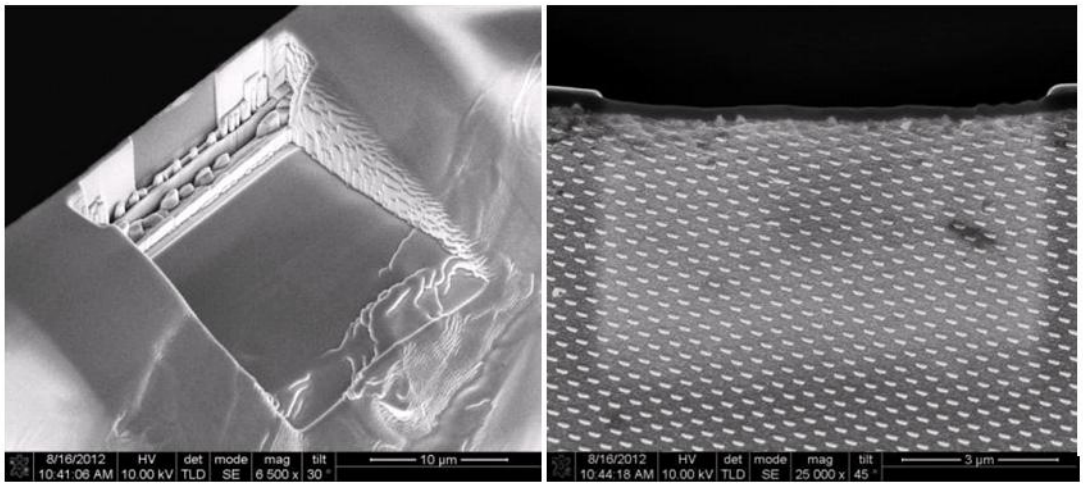

Figure 52: SEM micrograph of magnetoelectric TEM sample viewed from below (left). The underside of the viewing window is visible as a dark grey film in the upper left. SEM micrograph of the top surface of the viewing window (right) showing arrays of single domain nanostructures. The outline of the viewing window is visible as a faint, lighter region.

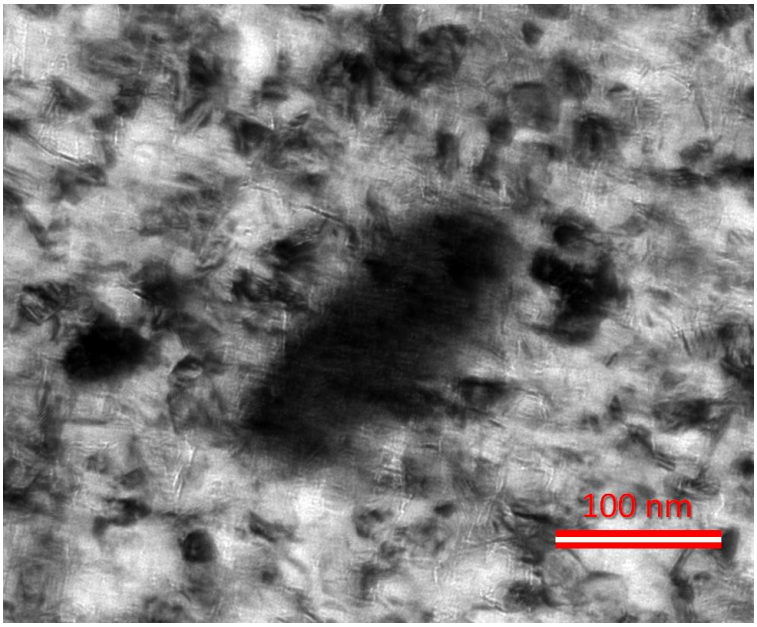

Figure 53: In-focus bright field TEM image of 200x100x35nm ellipse on PMN-PT

4.3.3.4 Concluding Remarks

To gain a better understanding of magnetoelastic reorientation it is necessary to make experimental observations with improved techniques. In this section the magnetoelastic spin reorientation of a single domain bit was observed in Lorentz TEM. The results were unsuccessful due to the thickness of the observation window and the relatively low Ms of nickel.

4.4 Single Domain Concluding Remarks

In this section three experiments were conducted which as a group demonstrate the viability of strain-based control schemes for single domain particles. Compared to thin films, single domain magnets have significantly more shape anisotropy which sets the initial magnetic configuration. From this base state the magnetization can be controlled deterministically if the induced magnetoelastic anisotropy is applied in the appropriate direction. This coherent rotation

of the magnetization is the key advantage of single domains. While thin film structures have no shape anisotropy, the stochastic alignment of the domains prevents thin films from having the same level of determinism as single domains. In the first experiment, the 90° rotation of $200x100x35nm^3$ nano-ellipses was demonstrated using the poling strain from a PMN-PT (011) substrate. While most bits rotated 90°, some bits did not rotate and others rotated twice, and this was shown to be caused by the random polarization direction of the un-poled piezoelectric substrate. These results were observed using the PEEM technique and represent the first visual evidence of a coherent single domain bit rotation with mechanical strain. In the second experiment, a device was presented and tested which would enable bi-stable and reversible 90° magnetization rotation. The key advantage of this technique is that the magnetization can be in only one of two energy wells, and these energy wells can be selected using mechanical strain. Without applied electric field, the magnetization remains due to the coexistence of an energy well along with the strain. In the third experiment, the magnetization rotation of ellipse structures was observed in Lorentz-TEM. TEM offers the highest resolution of any observation technique, however the magnetic sensitivity is relatively low and as a result no magnetic contrast was seen in the single domain structures.

Chapter 5: RING-SHAPED STRUCTURES

5.1 Synopsis

In this chapter the concept of a patterned nanostructure with *no shape anisotropy* is introduced. In ring-shaped magnets, the geometry is radially symmetric in-plane, meaning that any in-plane magnetization direction is energetically identical and no native easy axis exists. From this point of view, we may imagine a system where the magnetization can be defined arbitrarily with minimal energy input. Two experiments are described here on ring-shaped nanostructures where the net magnetization and motion of domain walls can be controlled deterministically and is shown to rotate by as much as 90°. In the first experiment, a 35nm thick ring structure's vortex domain walls are rotated by anisotropic strain and are observed in MFM. In the second experiment, a 10nm thick ring structure with Neel walls is also rotated in-plane and is observed in PEEM. In the last section, a method is proposed which would enable dynamic in-plane control of the magnetization and this may lead to many interesting devices, such a nanoscale magnetic motor.

5.2 Literature Review

5.2.1 Magnetization behavior in ring shaped structures

Shape-induced anisotropy is related to the demagnetization energy of an in-plane oriented magnetization. Since the magnetization configuration follows the shape anisotropy and thus the geometry of the sample closely, special care must be given to the design of magnetic structures. Shape-induced anisotropy may be reduced or eliminated all together through the adoption of high symmetry structures such as discs and rings. In disc structures below ~50nm the magnetization is single domain in-plane (in the case of Nickel). Such structures have not been

studied experimentally due to the difficulty inherent in manufacturing small structures of uniform diameter. In disc structures above ~50nm in diameter the flux may take the form of a vortex domain with significant out of plane magnetization components. Such disc structures are undesired for planar magnetization control because of the stability and lack of net magnetization in these vortex domains.

If the center of the disc structure is removed we will then have a *ring*, which is a very popular geometry receiving much attention in recent years[89,90,91]. The ring structure has two stable magnetization configurations: the *onion* and the *vortex*. The vortex state is identified by a magnetization which is completely enclosed in the structure. A shown in Figure 54, the vortex state shows little magnetic contrast in MFM due to the lack of external magnetic flux. The vortex state represents the most energetically stable magnetization state for the ring system but because of the zero-net magnetization has no immediate useful applications. By contrast, the onion magnetic state shown in the bottom of Figure 54 has two distinct magnetic poles identified by a dark and light domain wall region in MFM. The onion state is formed by applying a saturating magnetic field in-plane, then removing the magnetic field. The system relaxes to form two main domain regions separated by head and tail domain walls. The symmetry of the system and the hysteresis in the magnetic material allow the onion state to remain at zero-field and is thus a high-energy meta-stable magnetic state. Magnetic rings and the unique onion state can be made in any dimension, though the behavior of the ring and the magnetic structure of the domain walls vary with the ring's dimensions as will be illustrated next.

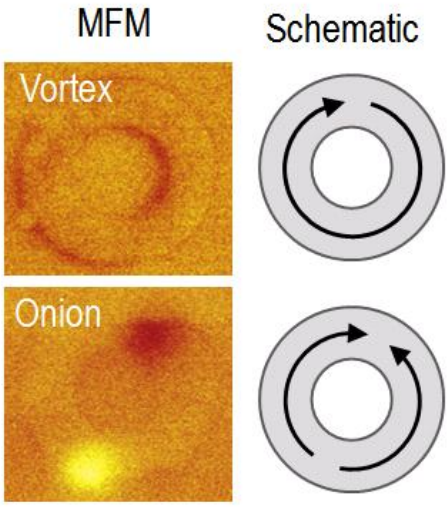

Figure 54: Stable magnetic configurations of the ring geometry, MFM scans and schematics. Vortex configuration has enclosed magnetization (top). Onion state has one magnetization direction and two domain walls (bottom).

Magnetic domains are regions of discontinuous magnetization within the same structure. They form automatically to minimize magnetostatic and exchange energies. There are many different types of domain wall which can form depending on the magnitude of these energies, and these ultimately depend on the geometry of the magnetic structure. Figure 55 shows magnetic force microscopy images of three different ring geometries and the corresponding domain wall structure. At left is a 2-micron outer diameter (OD) nickel ring displaying vortex-type domain walls which appear as swirling magnetic contrast. The annular width (i.e. the OD minus the inner diameter) is the critical dimension for domain wall formation, and this ring has a relatively thick annular width of 300nm. Upon formation, the onion magnetization state has considerable demagnetization and exchange energy across the annular width and a vortex nucleates to minimize these energies. If we reduce both the OD and annular width we will have the ring in the center figure of Figure 55, which has a 1-micron OD showing Néel type domain walls. These walls form between domains magnetized at 90° to each other and are identified by sharp discontinuities in magnetization contrast (i.e. triangular or broad contrast regions with

linear boundaries). The right-most figure in Figure 55 is of a ring which is 500nm in OD and has an annular width of just 100nm. The magnetostatic and exchange energies across the annular width are relatively small in this onion state so broad Néel or vortex domains are not favorable. The spin structure in the domain region of this structure is indeterminate, but it typified by a diffuse region of magnetic contrast.

It is necessary to consider the type of domain wall because different domain wall types have very different behavior when magnetoelastic anisotropy is introduced. The type of domain wall present in the structure is indicative of the demagnetizing field within the structure and this field is related to the tendency of the magnetization to pin against the structure walls. From this perspective one domain wall type may have less pinning potential and move easier than others with magnetoelastic anisotropy. While Néel and diffuse domain walls have considerable external flux normal to the structure (which contributes to demagnetization energy and can pin the magnetization), the flux from vortex domains is contained entirely within the structure indicating that the demagnetization field is greatly reduced. This means that a vortex domain contained within a low shape anisotropy ring has little to impede its rotational motion. The study of domain wall motion in rings under magnetoelastic anisotropy and its dependence on domain wall type and ring geometry will be discussed later in the present work.

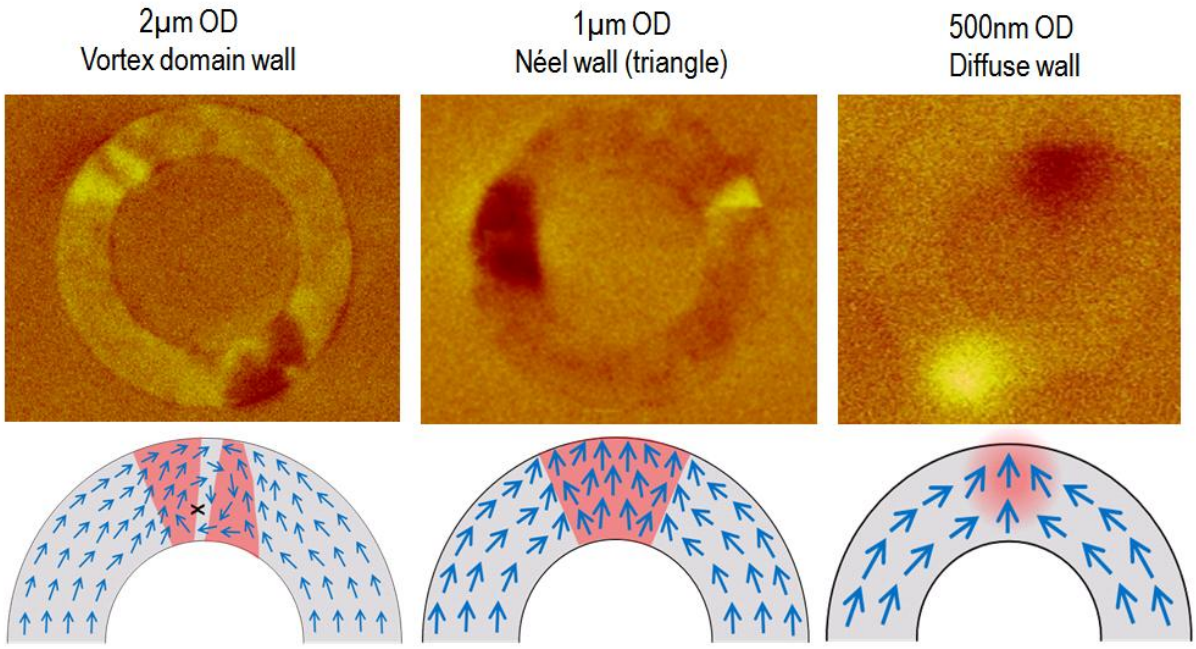

Figure 55: Domain wall configuration of the ring geometry as a function of structure geometry. Large annular widths and outer diameters tend to have vortex domain walls (left). The demagnetization energy is not large enough to form vortex domain walls so Neel walls are seen in smaller rings (center). In the smallest rings (right) the exchange at the domain wall region is reduced to the point where a definite domain wall is not required. A gradual rotation of spins results in a diffuse domain wall region.

In recent years, the ring structure has been frequently investigated for studies of magnetic domain wall physics[92], vortex memory applications[93], and magnetization dynamics[94]. In the introduction section it was previously mentioned that the type of domain wall within the onion magnetization state is dependent on the geometry of the ring structure. This behavior of rings was studied extensively by Mathias Kläui *et al.*[95], who is still regarded as the preeminent expert on magnetic ring structures. Figure 56 shows the magnetization phase diagram (i.e. the dependence of magnetic domain wall type on annular width and structure thickness) for Permalloy (a) and Cobalt (c) rings. The precise morphology of the ring domain wall is moderated by a balance between exchange and magnetostatic stray field energies:

$$E_{strayfield} = \frac{1}{8} M_s^2 t^2 W$$

$$E_{exchange} = \frac{1}{2} tAln\left(\frac{rmax}{rmin}\right)$$

Where t is the out-of-plane thickness of the structure, W is the annular width, A is the exchange coupling constant, and r_{max} and r_{min} are the outer and inner radiuses of the vortex core, respectively. The phase diagram as proposed by Kläui is thus:

$$t = \frac{A}{4M_s^2 W} ln\left(\frac{rmax}{rmin}\right)$$

As the annular width of the structure in Figure 56 increases beyond 250nm, the magnetization asymptotically favors the vortex magnetization state. Vortex domain walls form to minimize demagnetization energy, and this condition is only reached above a critical annular width. Vortex domain walls also have a considerable out-of-plane component which we may expect to be favorable in thicker structures. This is confirmed in Figure 56a: for the same annular width the vortex state is favored in thicker structures, especially above 7nm. This work demonstrates that how the domain wall can be engineered by simply selecting the appropriate ring geometry. The next section will discuss the importance of domain wall type as it pertains to domain wall mobility.

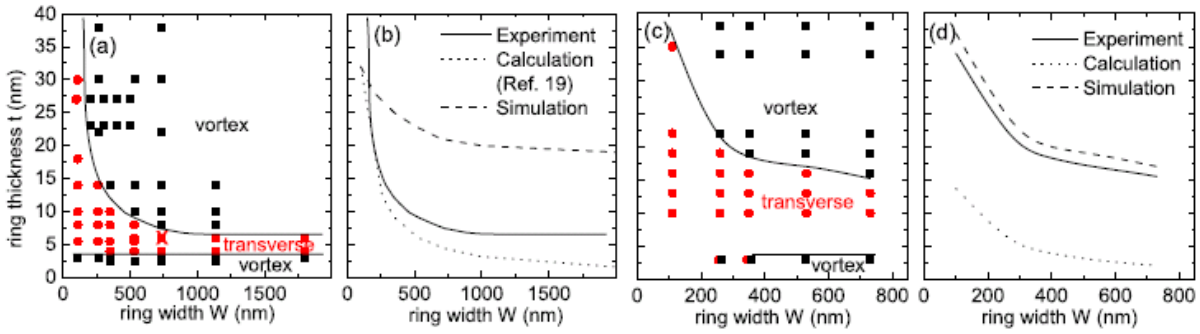

Figure 56: Magnetization phase diagrams for various ring structures. Permalloy rings (a) and Cobalt rings (c). (From Mathias Kläui *et al.)*

Knowing which type of domain wall to expect in a ring is important if our goal is to move the wall through magnetoelastic anisotropy. This is because different domain wall types have different in-plane magnetization components and magnetostatic pinning potential. The simulation plots in Figure 57 show how a structural defect in a ring structure has major consequences for the motion of different domain wall types. The energy vs. position plots at the bottom of Figure 57 illustrates how vortex and transverse walls behave in an opposite manner to the same defect. Figure 57a is of a transverse domain wall. The demagnetization field is transverse to the ring structure and this energy is minimized for thinner constrictions. For this reason this type of domain wall is most energetically stable at the thinnest portion of a defect, as shown schematically in the energy vs. location plots at the bottom of Figure 57. We may expect the mobility of a transverse domain wall pinned in such a manner to be very low due to the energy minimum which exists at that point. In contrast, Figure 57b shows the same constriction with a vortex type domain wall. The black arrows in Figure 57b and c point to the maximum transverse demagnetization field in this domain wall around the leading and tail edges of the vortex. As the vortex nears the defect the spins in the leading edge rotate to become parallel with the defect. The spin rotation in the leading edge compresses the spin relaxation length and increases the exchange energy in this region. This exchange is relieved through rotation of

neighboring spins and any further motion of the vortex domain is inhibited. Vortex domains thus experience notch defects as an impediment to motion as shown in the schematic energy diagram below Figure 57b. Regardless of domain wall type, defects play a crucial role in motion impediment and this work illustrates the importance of defect free structures in domain wall studies.

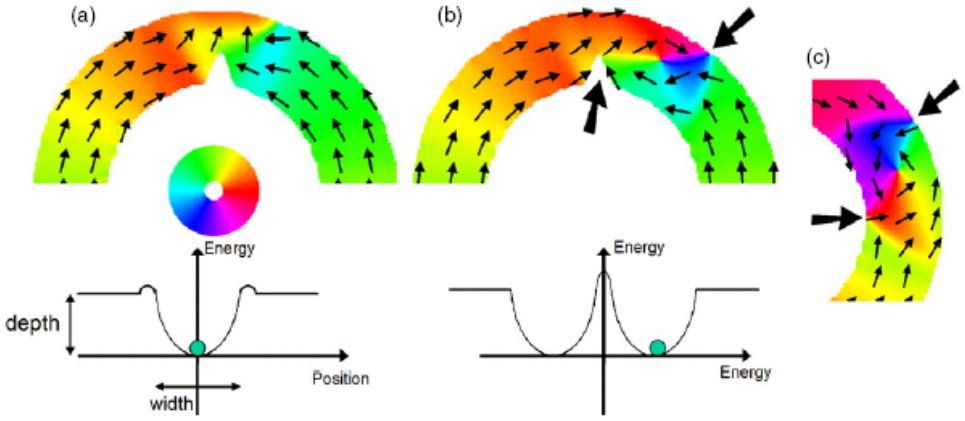

Figure 57: Defects in ring structure and the pinning/repulsion behavior depends on the type of domain wall. Transverse domain wall is pinned by defect (left). Vortex domain wall is repulsed (right). (From Mathias Kläui *et al.)*

5.2.2 Current induced domain wall motion

Domain wall motion in ring structures has recently attracted great interest because it may yield information about the energy landscape of domain walls, their evolution and response to external energies, and magnetization dynamics in general. The first studies of domain wall motion in rings were done with externally applied magnetic field bias[92,93,96]. DC magnetic fields are applied in-plane to vortex domain walls in a long, smooth strip line and the motion and evolution of the domain wall over time is observed. In this situation the Zeeman potential of the applied field interacts with the local spin structure of the domain. If the Zeeman potential is large

enough to de-pin the domain wall then motion occurs. Interestingly, the domain wall also undergoes deformation and evolution as it propagates and the speed of this propagation is nonlinear and oscillatory. Under a magnetic field bias a vortex domain may evolve into a transverse domain, and then back into a vortex domain as it propagates along a strip line. The forward velocity of such a domain appears oscillatory and the forward motion can even reverse at times. This oscillatory behavior is related to the procession of spins within the vortex and the coupling of the vortex core to the applied Zeeman potential. This view is supported by the fact that vortex motion begins after an initial time delay due to the "effective mass" and dissipative elements we expect in dynamic oscillatory systems. These observations illustrate that domain wall motion is a non-adiabatic process but nevertheless, precise domain wall positioning with magnetic field is possible.

Spin-polarized currents also have been applied to domain walls to initiate motion with great success[97,98]. First, a domain wall is initiated in a long strip of ferromagnetic material. A current is injected on one end of the domain wall and becomes spin-polarized on passage through the domain wall. Exchange interaction between the polarized spin and the domain wall is increased but this energy is transferred as a spin torque on the domain wall itself. The domain wall displaces in the direction of the current flow and the effect is greatest in thin domain walls which have a high magnetization gradient. Fast domain speeds of over 100m/s can be achieved with ultra short pulses of <100ps but with very high current densities of up to $10^{12}A/m^2$ [97]. Shown in Figure 58 is experimental photoemission electron emission microscopy (PEEM) imagery of current-induced domain wall motion in a 1000nm wide Permalloy strip line. The domain wall is shown to displace approximately 400nm with each pulse, and after five current pulses displaces a total of about 2000nm. The domain wall also appears to transform from a vortex type domain into a transverse type domain. A high degree of control can be obtained with

this technique, though the current densities and domain wall transformations may prohibit device level implementation. The influence of other anisotropies (such as magnetoelastic anisotropy) on the motion of domain walls in ring structures has to be investigated, but this will be shown later in the present work.

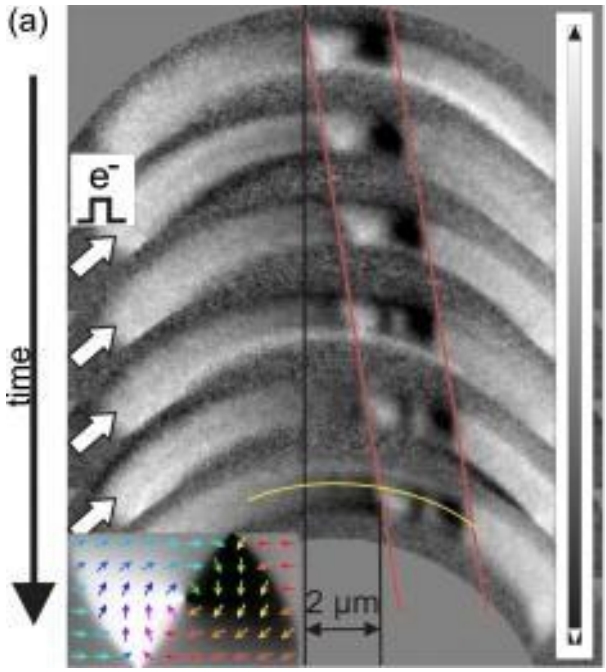

Figure 58: Time-resolved PEEM imaging of vortex domain wall motion in Permalloy ring nanostructure under applied current pulses. (from O. Boulle *et al*.[97])

5.3 Experimental Work

5.3.1 Electric field induced magnetization rotation in Ni ring structures

5.3.1.1 Problem Introduction

Patterned ferromagnetic nanostructures have been studied extensively for applications in non-volatile data storage and memory, where information is to be encoded within the bit's magnetization direction. While attractive features include stability and predictability of magnetic states, these characteristics simultaneously inhibit magnetic manipulation for recording. For

example, in bi-stable single domain nanostructures the large shape anisotropy requires relatively large external energy to switch the magnetization (i.e. high strength magnetic field)[80]. Therefore, new geometries and writing mechanisms need to be investigated that can easily switch magnetization directions with low power.

Several approaches to lower the energy barrier between magnetic states have been attempted using low geometric ratios and/or magnetic meta-stabilities, and switching mechanism which include current injection[99], voltage-induced magnetic anisotropy[100], and magnetoelastic strain[7]. More recently, the ring geometry has been studied for both its unique meta-stable "onion" magnetization state, and its stable "vortex" state, for encoding a bit of information in chirality[101]. Reorientation of the onion magnetization state is accomplished by either applying a magnetic field[89,90,91] or injecting current[102,103]. Both of these reorientation mechanisms result in either an onion to vortex transition or a partial rotation of the onion's vortex-type domain wall. These methods are considered impractical due either to large energy requirements, in the case of applied field, or cumbersome wiring arrangements, in the case of current injection. Furthermore, neither of these two methods are capable of achieving coherent rotation of the onion state (onion to reverse onion transition), though this has been proposed[104]. Therefore, other ring switching approaches warrant study.

More recently, researchers[83,105,106] have suggested using mechanical and electric field induced strain as magnetic switching mechanism through the generation of magnetoelastic (ME) anisotropy in magnetoelectric heterostructures, although this has not been studied in the context of rings. ME anisotropy (e.g. $K_{ME}=(3/2)\lambda_s E|(\varepsilon_y-\varepsilon_x)|$ [J/m^3]) is a function of the material's magnetostriction constant λ_s, Young's modulus Y, and induced strain anisotropy $\varepsilon_y-\varepsilon_x$. The K_{ME} is used to overcome other energies, such as shape anisotropy and defect pinning, to reorient the

magnetization direction (i.e. an easy axis). The induced anisotropic strain is generated electrically by combining a piezoelectric with a magnetostrictive material to form a magnetoelectric heterostructure or laminate[107]. One piezoelectric material that has been studied to produce anisotropic strains is a single crystal (011) PMN-PT. This particular cut produces tensile and compressive strains in two orthogonal in-plane axes ($01\bar{1}$ and 100) as well as providing a memory effect from the remnant strain states[108,109]. Magnetoelectric heterostructures of this type are simple in design, requiring only electrodes on the piezoelectric member to achieve magnetic reorientation. While a few papers exist in the literature investigating magnetoelectric nanobar structures[83], their application to ring geometries is absent. One advantage associated with ring structures is the lower contribution of shape anisotropy to the Gibbs free energy as compared to nanobars or ellipses with aspect ratios larger than one.

5.3.1.2 Experimental Setup

In this paper[110], we experimentally investigate the reorientation of the onion state in a nickel ring structure fabricated on a piezoelectric substrate. An un-poled $10 \times 10 \times 0.5$ mm^3 single-crystal (011) $Pb(Mg_{1/3}Nb_{2/3})O_3]_{(1-x)}$-$[PbTiO_3]_x$ (PMN-PT, $x \approx .32$, ATOM OPTICS CO., LTD., Shanghai, China) with 5nm Ti/50nm Pt deposited as an adhesion layer/electrode is used as the substrate. On the top (011) PMN-PT surface, ring geometries were patterned using a dual-layer methyl methacrylate (MMA) lift-off resist and electron beam writing with a current of 1000μC/cm^2. Three ring geometries with inner/outer diameters were studied: 350/500nm, 700/1000nm, and 1400/2000nm. After ring pattern development, 5nm Ti/35nm Ni/2nm Pt (adhesion, ferromagnetic, capping layer) was deposited by e-beam evaporation. This was followed by lift off, resulting in nickel ring structures strain-coupled with the substrate. A schematic of the experimental setup and crystallographic orientation along with an SEM image

of the ring structures are shown in Figure 59. Magnetic force microscopy (MFM) images were collected by a Bruker Dimension 5000 scanning probe microscope using low-moment tips to eliminate tip-induced perturbations of the ring magnetization. Voltages are applied to the bottom electrode in situ while the top electrode and MFM tip are connected to a common ground to eliminate electrostatic interactions.

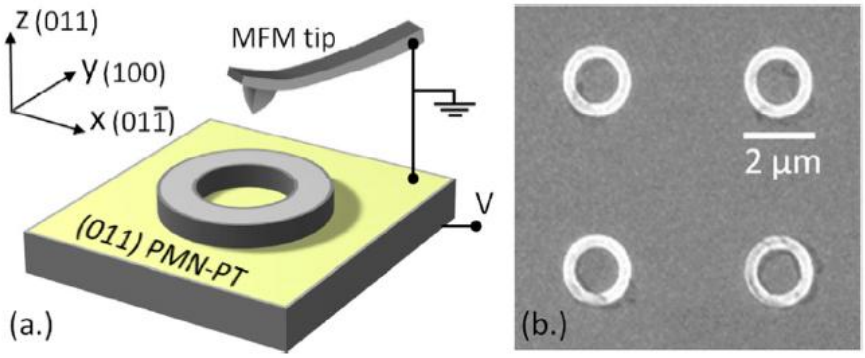

Figure 59: (a.) Schematic of experimental setup of Ni ring/PMN-PT heterostructure and (b.) SEM micrograph of 2000nm ring structures

5.3.1.3 Experimental Results

Following fabrication and prior to poling (i.e. residual strain ~0) the rings are magnetically annealed in an externally applied field of 5kOe along the y axis (see Figure 59) to form the characteristic onion state after removing the field[104]. As shown in Figure 60a in the 2000nm ring MFM image, the onion state can be identified by light and dark spots (i.e. circled regions) which are aligned with the direction of the applied magnetic field along the y-axis. These spots correspond to the location of highest magnetization divergence (i.e. tip-sample interaction) and mark the location of vortex-type domain walls[111]. We note that the domain walls presented in Figure 60a are not perfectly aligned with the applied magnetic field due to the existence of local energy wells which cause them to "relax" to a local energy minimum. These

local energy minimums may be attributed to imperfections in the ring geometry and/or defects, grain boundaries in the material[111], or pre-stress due to the fabrication.

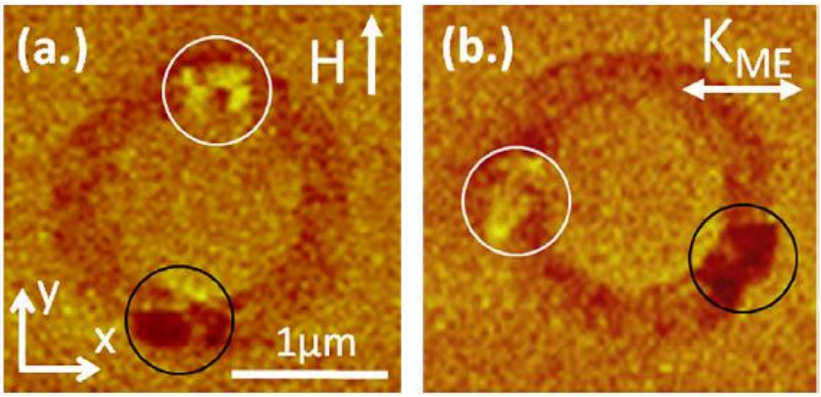

Figure 60: Magnetic force microscopy images of ring structures. (a.) 2µm ring structure in onion magnetization state along +y direction. (b.) ring after application of 0.8MV/m to the PMN-PT substrate demonstrating near-90° rotation of magnetic dipoles

After the magnetic field is removed, a ramped electric field up to 0.8MV/m is applied to the ferroelectric substrate to pole the PMN-PT and is held constant. Figure 61 plots the strain anisotropy (right ordinate axis) and magnetoelastic anisotropy (left ordinate axis) produced by the PMN-PT as a function of applied electric field (adapted from T. Wu *et al.* 2011[31]). The anisotropic piezostrain at 0.8MV/m (point b) is 700µε consisting of -1200µε along the x axis and -500µε along the y axis[111]. The magnetoelastic anisotropy at 0.8MV/m is ~7.4kJ/m^3 (i.e. Y= 220GPa and λ_s=-32ppm for nickel). The combination of anisotropic strain and magnetoelastic anisotropy theoretically creates an easy axis along the x-axis.

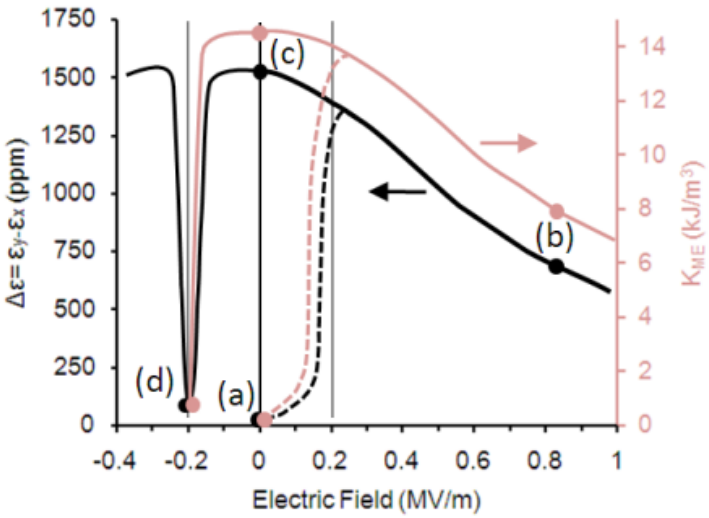

Figure 61: In plane anisotropic strain (black, left) and magnetoelastic anisotropy (red, right) as a function of applied electric field. (a.) un-poled, zero strain state. (b.) poled substrate with constant applied field. (c.) poled substrate at remnant polarization state. (d.) de-poled substrate after reversing electric field. Initial poling process is shown with dashed line.

Figure 60b shows an MFM image of the Ni ring structure as the electric field is held constant at 0.8MV/m. Comparison of the MFM images in Figure 60a (field annealed) and Figure 60b (0.8 MV/m) reveals that the location of the light and dark spots (i.e. vortex domain walls) has rotated 90° counter clockwise (CCW) and is now parallel with the x axis. More specifically, the vortex domain walls rotated to align with the magnetoelastic easy axis through the application of an electric field. Theoretically, the magnetoelastic anisotropy and induced strain should achieve a maximum rotation of 90° and these results approach this limit. In this study, a large number of these rings were investigated and in a variety of dimensions. It should be noted that magnetization rotations were also observed in the 1000nm and 500nm diameter ring geometries. However, for the 1000nm and 500 nm ring structure these rotations were not reproducible and the results were excluded from this letter. Rotation events were only observed in a small fraction of these ring structures. We attribute the reproducibility (i.e. variability from

ring to ring) issue to the higher incidence of pinning defects (e.g. most probably geometric defects due to processing issues) in 1000nm and 500nm rings (i.e. fabrication defects more prominent in smaller size) and/or the lack of a vortex type domain wall. With regard to the later point, the high mobility of the vortex domain walls in 2000nm rings as compared to the transverse domain walls of 1000nm and 500nm rings is a topic which warrants further study.

Figure 62a-d show the behavior of the 2000nm ring's magnetization under different electric field/strain conditions. For this study, a different 2000nm ring is imaged with MFM. Figure 62a is an MFM image after applying and releasing a saturating magnetic field (5 kOe) along the y axis. The PMN-PT induced strain state for this ring is found in Figure 61 at point a (i.e. $\Delta\varepsilon=0$). Figure 62b shows an MFM image with 0.8MV/m applied to the substrate (strain referenced to point b in Figure 61) in which the onion state rotates ~45° CCW toward the new easy axis. Figure 62c shows that the magnetization remains in the same direction as for the 0.8MV/m case shown in Figure 62b after the electric field is removed (E= 0.0MV/m). This shows that for this electric field (see point c in Figure 61) a remnant anisotropic strain of ~1500$\mu\varepsilon$ is still present in the sample. The magnetization did not rotate upon removal of the electric field because the easy axis has not changed. In fact the magnitude of the anisotropy increased from ~7.4kJ/m to ~16kJ/m. Therefore, removal of the field made this a more favorable easy axis. Thus, a voltage is not required to maintain the magnetization direction due to the lack of a driving energy to reorient the vortex domain walls. To further illustrate the magnetoelastic origin of the rotation, an electric field of -0.2MV/m (note change in polarity) is applied to de-pole the substrate and return it to a near-zero strain state[31] (i.e. point d in Figure 61). As shown in Figure 62d the magnetization remains in the 45° CCW position, identical to Figure 62b and Figure 62c, because once again a new easy axis has not been created by the change in electric field. This can be seen by looking at the strain field and the magnetoelastic anisotropy shown in

Figure 61 point d. Therefore, further application of an electric field does not reorient the onion state. If reorientation with an electric field is desirable it can be achieved as T. Wu *et al.***Error! ookmark not defined.** demonstrated by depositing the structures on a partially poled substrate. A partially poled substrate biases the remnant strain and thus a new easy axis can be created with the application of a pulsed electric field.

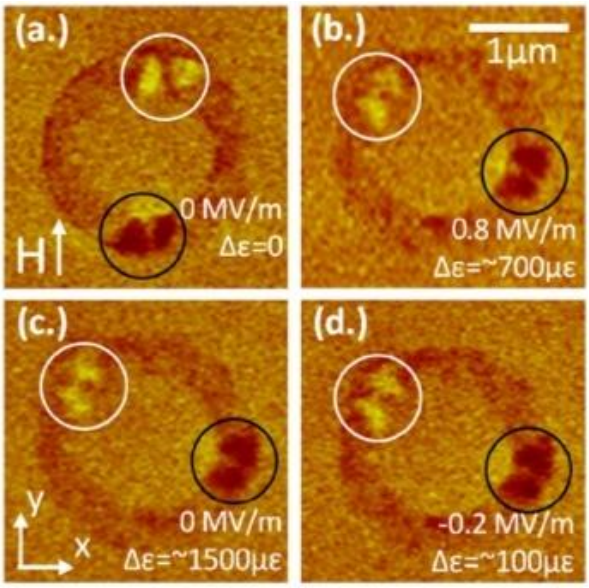

Figure 62: Magnetic force microscopy images of a 2000nm ring structure under different strain states. (a.) Onion initialized in the +y direction. (b.) 0.8MV/m applied to the PMN-PT substrate, note CCW rotation of magnetic poles. (c.) 0.0MV/m, note stability of magnetic rotation. (d.) -0.2MV/m to de-pole substrate

The ease of magnetic rotation in this system is due to a number of factors which combine to reduce the competing magnetic anisotropies. Firstly, the radial symmetry of the ring structure reduces shape anisotropy such that any magnetization direction is energetically equivalent. Secondly, the electric field induced anisotropic strain from the piezoelectric substrate generates sufficient magnetoelastic anisotropy in the ring structure to rotate it to new directions, though pinning defects remain an issue. Lastly, the vortex-type domain walls present in the thicker 2000nm ring structures exhibit high exchange and low demagnetization energy[111], which may

reduce the effect of magnetization pinning along the ring's normal surfaces. The relative lack of magnetic anisotropies in the ring system may enable interesting applications in which other anisotropies are introduced advantageously. For example, uniaxial anisotropy may be introduced through the addition of an exchange bias underlayer or with a magnetic field annealing process during the metal deposition, thereby creating a defined easy axis in the ring. Other easy axes could then be created magnetoelastically using the coupled piezoelectric substrate, thus resulting in numerous stable magnetization configurations. Switching between two stable magnetization states could be accomplished with short electric field pulses to the substrate. This is one example of a bi-stable magnetic switching scheme for magnetic memory applications made possible by the ring geometry.

5.3.1.4 Concluding remarks

In summary, we achieved a permanent 90 degree rotation in the magnetization direction of patterned rings using only electric field-induced magnetoelastic anisotropy. This experiment serves to underscore the relevance of the strain-mediated magnetoelectric effect in emergent technologies.

5.3.2 Domain wall motion in Ni ring/PMN-PT heterostructures observed by PEEM

5.3.2.1 Problem Introduction

In the previous experiment, magnetic force microscopy was used to observe magnetization rotation in Nickel ring structures. While providing excellent spatial resolution, the MFM method suffers from a slow scan rate and may even interfere with the magnetization of the ring due to stray field from the scanning tip. To eliminate the possibility of tip-induced

perturbations and to improve the speed of characterization, magnetoelastically coupled Nickel ring samples were prepared for XMCD-PEEM study.

5.3.2.2 Experimental Setup

The sample consists of 1μm, 2μm, and 3μm OD rings in 10nm-thick Nickel with annular widths of 200nm, 250nm, 300nm, and 350nm. Electric fields from 0V to 175V were applied in steps of 5V and the resulting XMCD contrast, XMCD color map, and magnetization schematics are shown in Figure 63. Before the experiment, a saturating magnetic field is applied to the ring perpendicular to the axis of magnetic sensitivity, which is shown by the black arrow Figure 63.

5.3.2.3 Experimental Results

The initial magnetic configuration may be interpreted from the PEEM color map and a schematic of this interpretation is shown in the upper right corner of Figure 63. The ring initially has four domain walls which are head to head and possibly in the transverse domain wall state. This initial magnetic configuration is unexpected as it is neither the classic vortex nor the transverse onion state. This multidomain state is likely caused by insufficient saturating magnetic field combined with a substantial initial remnant strain which is possibly results from a previous poling experiment. Next, electric field is applied to the substrate and the response from the maximum field of 175V is shown in the bottom half of Figure 63. As evidenced by the PEEM contrast and color plots at 175V, the magnetization in the ring changes significantly with the added magnetoelastic anisotropy. At 0V, many parts of the ring are colored blue signifying magnetization vertically downward as shown in the schematic in Figure 63. These blue parts turn red at 175V indicating that the magnetization in these regions rotated 180 degrees. The magnetization at 175V favors parallel alignment with the magnetoelastic anisotropy, causing two

prominent domains to nucleate then sweep and dominate over the four domains which were present at 0V. A schematic of the final magnetization state is shown in the bottom right corner of Figure 63. The magnetization points radially outward at all points around the ring, though the majority of the spins prefer parallel alignment with the strain field. This may be caused by a complex superposition of field-induced magnetization states, magnetoelastic anisotropy, and pre-strain. Focusing on the domain wall regions, it is clear that a significant translation and rotation of the domain walls occurred. If we consider the scale of the PEEM images we may conclude that the domain walls displaced several micrometers. The reduction in the number of domains from four down to two indicates that the magnetostatic increased in these areas and that the exchange energy between these domains also increased. We may conclude that the potential energy resulting from magnetoelastic anisotropy initiated domain motion and was ultimately converted into exchange and magnetostatic energies through the elimination and rotation of domain walls.

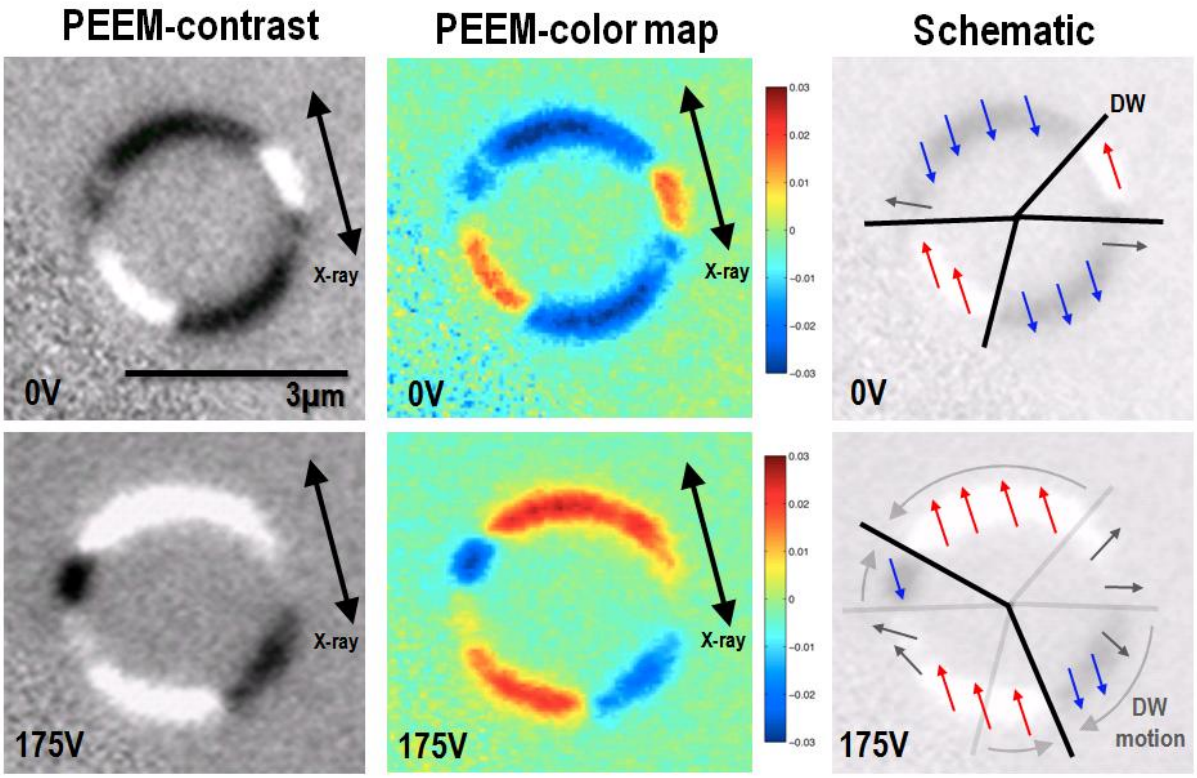

Figure 63: XMCD-PEEM contrast (left), XMCD-PEEM with color mapping (center), and magnetization schematics (right) for a 3 micron OD Nickel ring on PMN-PT with and without applied voltage. From the PEEM color map we can infer four domain walls at 0V. At 175V we observe a collapsing of the domain walls reducing the number of walls from four to two.

5.3.2.4 Concluding Remarks

These preliminary results already indicate that magnetoelastic anisotropy can be used to deterministically position domain walls in ring structures owing to their lack of shape anisotropy. Future experiments with rings in XMCD-PEEM will focus on initializing the vortex magnetization state and minimize the initial remnant strain in order to achieve a more clearly defined magnetization rotation.

5.3.3 Continuously rotating magnetization in ring structures by stepped radial strain

5.3.3.1 Problem Introduction

This experiment concerns the design and fabrication of a nanoscale magnetic stator capable of continuous high frequency magnetization rotation. The previous work on magnetoelastically controlled ring structures consisted entirely of strain-coupled Nickel rings on a PMN-PT (011) substrate. This substrate created magnetoelastic anisotropy by straining anisotropically under an applied electric field. While useful for demonstrating 90° control of magnetization, this substrate cannot achieve the multiple strain fields required for positioning the magnetization in an arbitrary direction. As shown in Figure 64 (left), the magnetization of the onion state can theoretically be positioned in any direction provided a strain field can be created in that direction. In this example, the strain fields are separated by an angle of 60° and are stepped sequentially to enable continuous rotation of the onion state. One way this strain field may be achieved is by patterning electrodes 60° from each other as shown in Figure 64 (right). Here, an electric field is applied between opposite pairs of electrodes which actuates the piezoelectric material under the ring structure. The piezoelectric material may be polycrystalline or a single crystal, but the reliance on PMN-PT (011) is eliminated. The piezoelectric material elongates in the direction of the electric field provided d_{33} is positive, and contracts perpendicular to this field provided d_{31} is negative. The combined action of this elongation and contraction is anisotropic strain and magnetoelastic anisotropy. If the material between the electrodes is operated in the linear piezostrain regime then low-loss and high frequency actuation and magnetization rotation may be realized.

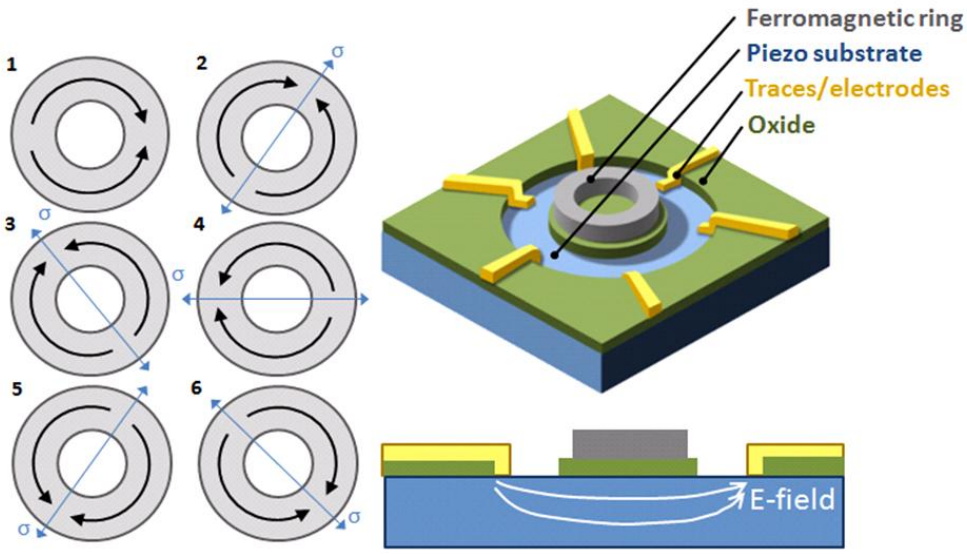

Figure 64: Schematic of stepped mechanical strains to achieve full rotation of magnetization (Left). Plausible device structure to achieve stepped mechanical strains consisting of electrical traces on piezoelectric substrate (Right).

5.3.3.2 Experimental Setup

Electrodes were patterned directly onto PMN-PT (001) by the e-beam lithography/ lift off method. Each electrode is 60° from each other, is .5mm wide and made of 35nm thick Nickel deposited by e-beam evaporation. The spacing between opposite pairs of electrodes is 1mm and an array of ring nanostructures were fabricated in the center of the electrode array which are characterized by MFM. Electric fields were applied between opposite pairs of electrodes while simultaneously measuring the polarization of the material.

5.3.3.3 Experimental Results

Photographs of these preliminary tests are shown in Figure 65. The electrodes were first poled with 20V (.2MV/m) in the 2-2 arrangement as shown in the center image of Figure 65. A light band of opaque material can be seen extending from the electrode pairs. Owing to PMN-

PT's tendency to change optical properties when polarized, we may obtain qualitative evidence of the non-ideal poling behavior between these electrodes. On close inspection of the material aberrations, the electric field between electrodes does not simply extend between opposite electrodes but instead envelopes a broad region several millimeters in all directions. We may expect the strain field to be non-uniform and extending far beyond where it is desired. Next, an electric field of .2MV/m is applied in the 3-3 arrangement as shown in the right image of Figure 65. The opaque markings on the substrate disappear and the qualitative electric field distribution becomes uncertain. Later, inspection of the substrate material by optical microscope revealed that several cracks had formed on the top surface of the substrate material, likely due to an intense strain field gradient. Future tests should focus on electrode spacing and geometry to improve strain uniformity.

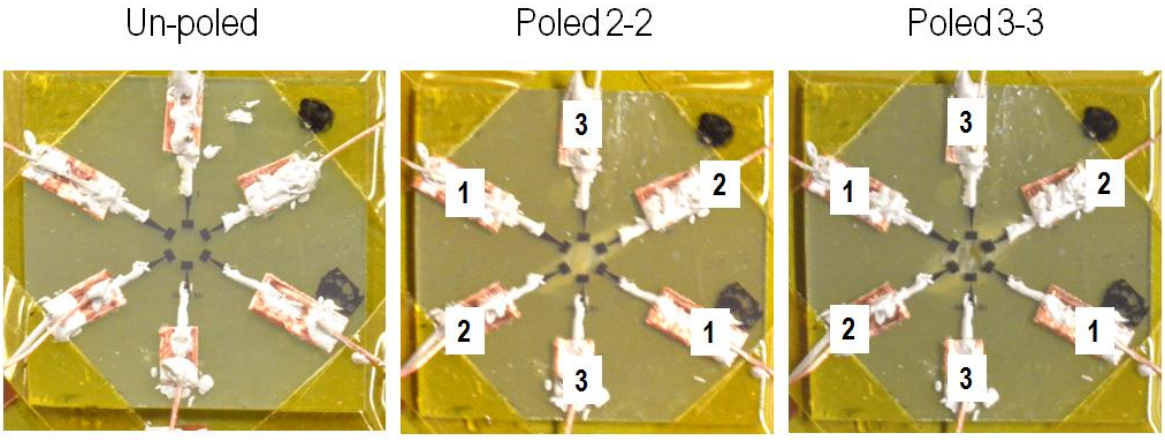

Figure 65: Visible evidence of poling-induced modification of PMN-PT transparency. Un-poled state (left). Poled diagonally between 2-2 (center), Poled vertically between 3-3 (right).

Many novel devices may be developed from the rotating ring magnetization technology. One interesting device consists of a rotating magnetic structure (i.e. a rotor) which is dipole coupled to the ring stator. The rotor follows the magnetization rotation of the ring stator,

enabling mechanical work to be done. Such a device may be used for mixing or to provide mechanical power to nanoscale devices as shown in Figure 66 (left). A slight modification of this device would enable its use as a propulsion device as shown in Figure 66 (right). Here, a set of bacteria-inspired flagellum would be fabricated on the rotor structure. As the rotor rotates, the flagella would propel through a fluid in a corkscrew-like motion. One might imagine an array of such propulsion structures on a free swimming device like that in Figure 67. This is an artist's interpretation of a self-powered nanoscale submarine which may potentially be developed with the nanomotor technology. The device would include an array of magnetic rotor/flagellum assemblies for propulsion as well as guidance, power, etc to perform tasks such as autonomous nanoscale surgery.

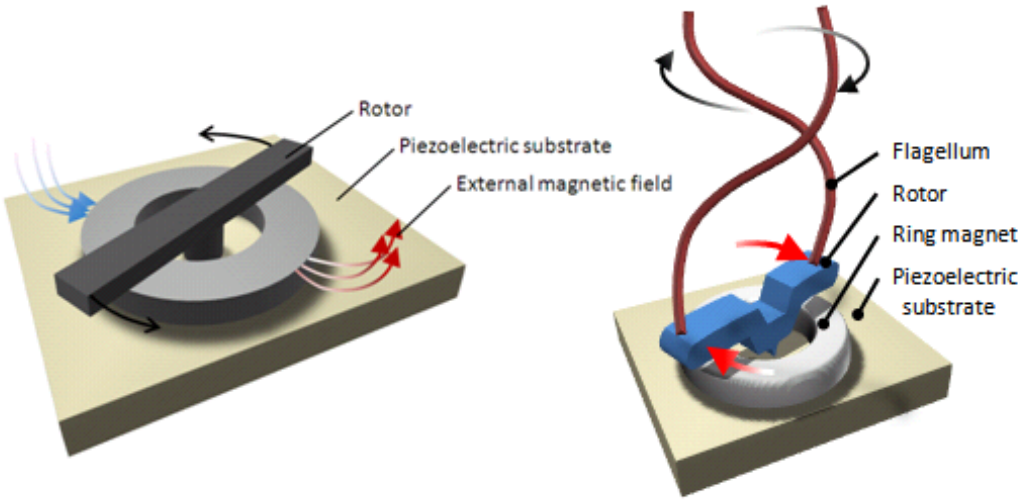

Figure 66: Artist impressions of completed nanomotor assemblies. Nanomotor with magnetic rotor showing external flux lines (Left). Nanomotor with flexible flagella attachments for propulsion applications (Right).

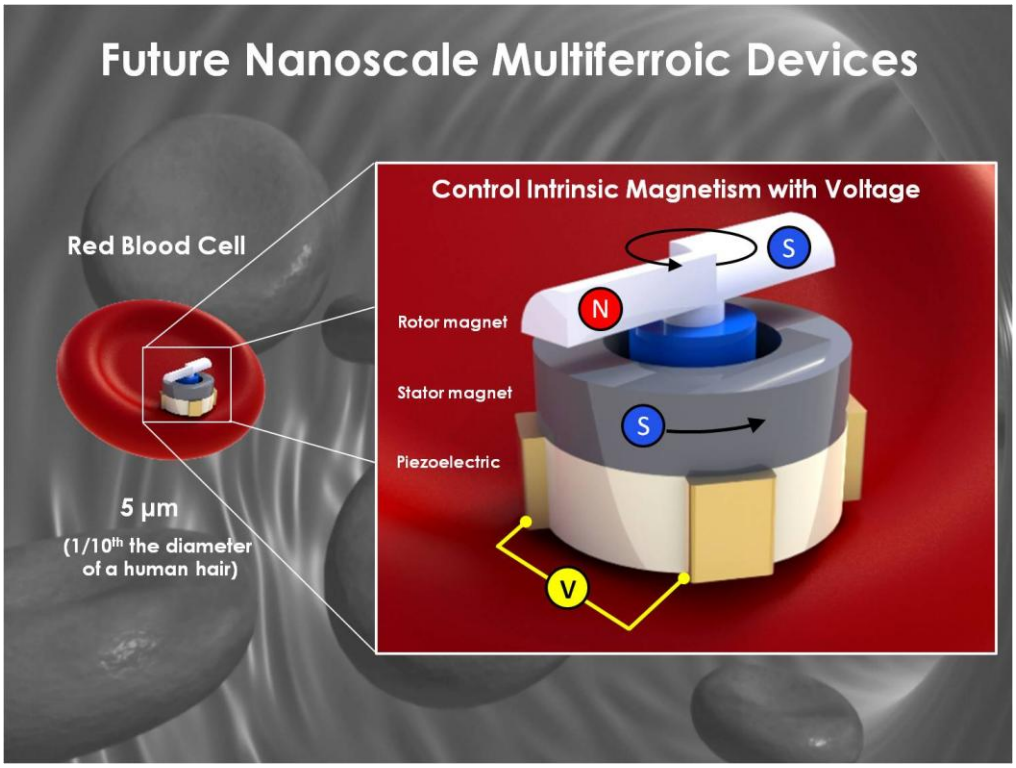

Figure 67: Artist impression of the "Fantastic Voyage" nanosubmarine for internal medicine.

5.3.3.4 Concluding Remarks

While 90° magnetization rotation on PMN-PT (011) with out-of-plane electric fields has been well established in the literature, this section aimed to accomplish rotation using in-plane electric fields and patterned electrodes. The main advantage of this approach is that the magnetization can be rotated in any arbitrary direction depending on the direction of the in-plane electric field. This approach may also enable continuous (i.e. dynamic) magnetization rotation. Experimental results demonstrated that it is possible to apply in-plane electric fields, but the exact strain state beneath the ring structures was ambiguous and worse still, the substrate suffered multiple stress fractures. Future work will focus on modeling to design electrode configurations that will improve strain output. Experimental efforts will aim to include an

insulating layer to confine the electric field within the piezoelectric substrate and thereby improve the uniformity of the electric field and strain output.

5.4 Ring Structures Concluding Remarks

This section discussed magnetization control in ring-shaped structures. Because ring structures have high in-plane symmetry and no effective shape anisotropy, the magnetization can be controlled with minimal strain input. Any arbitrary magnetization direction is a metastable energy state, so the magnetization remains when the strain is released. In the first experiment, a 90° rotation of vortex domain walls is observed in MFM when anisotropic strain is applied. In the second experiment, the evolution and rotation of Neel domain walls is observed in PEEM. In the final experiment, an attempt was made to accomplish continuous domain wall motion using radially spaced electrodes and in-plane electric fields. The ring structure when implemented in a magnetoelectric heterostructure enables the deterministic control of in-plane magnetization and this could lead to many new magnetic devices. At the close of this chapter, a nanoscale motor device was proposed which may enable rotating mechanical energy transfer at the nanoscale. The ring structure thus represents the next evolution in magnetic devices exemplifies the versatility of the magnetoelastic control approach.

Chapter 6: CONCLUSION

In the present work, the influence of magnetoelastic anisotropy (i.e. mechanical stress) on magnets of different size and scale was demonstrated. The common architecture of all devices was the magnetoelectric heterostructure, wherein electric fields applied to a piezoelectric substrate generate magnetoelastic anisotropy in the bit via interfacial strain transfer. Significant differences were observed in the magnets' response to magnetoelastic anisotropy depending on the starting magnetic morphology of the sample, and thus the scale and or geometry. While some form of magnetic perturbation is possible for all heterostructures, true deterministic control occurs for single domain and low shape anisotropy nanostructures.

In Chapter 2 the influence of magnetoelastic anisotropy in bulk laminates was investigated. A deterministic control of magnetism was difficult to accomplish in this system because bulk laminates are in the multidomain state and because the magnitude of strain was insufficient and isolated to a single mechanical interface. However, the converse magnetoelectric transduction coefficient (CME) was modulated by the strain via stress-induced modification of the piezomagnetic coefficient. Applied electric fields created isotropic planar stress which rotated the magnetization perpendicular to the applied stress and improved the magnetostriction properties of the bulk laminate. While a local modification of magnetization is likely occurring within the laminate, a net change in magnetization will require a significant reduction in magnetostatic energy and thus aspect ratio and scale.

In Chapter 3 the control of thin films was demonstrated in the out-of-plane to in-plane geometry and also in the planar rotation geometry. In 60nm Ni film the magnetization is at a transition point between in-plane and out-of-plane, thus lowering the energy barrier enough to

enable isotropic planar compression to cause an out-of-plane to in-plane magnetization rotation. The magnetization rotation is only a stochastic modification of the local Neel closure domains and thus cannot be considered a net or deterministic control of the magnetization. In 35nm Ni film, the magnetization is confined in-plane. In this case, anisotropic planar strain causes the magnetization to rotate in the plane of the film. This is seen as a growth and motion of Neel domain walls and sudden Barkhausen jumps. Again, the magnetization is not controlled deterministically and only local changes in spin morphology occur. Still, the reduction in magnetostatic energy by moving to a nanostructured thin film geometry from a bulk laminate resulted in a significant improvement in magnetic control.

In Chapter 4, two different deterministic control methods were demonstrated on single domain ellipse structures. In the first experiment, the poling strain from a piezoelectric substrate was used to rotate the magnetization of the bit by 90°. This happens because the magnetoelastic anisotropy overcomes the native shape anisotropy of the bit and establishes a new easy axis perpendicular to the long axis. While most bits rotated 90° only once, others rotated 90° then rotated back, and still others did not rotate at all. It was proposed that this is caused by differences in the local piezostrain due to random ferroelectric polarization alignment at the time of bit deposition. In the second experiment, a bistable 90° memory device was demonstrated. The magnetization can be switched between two energy wells by the mechanical stress, however this requires the application of a magnetic field perpendicular to the bit's uniaxial anisotropy. The advantage of this device is that the height of the energy barrier can be engineered by the bit's geometry and the applied magnetic field and the magnetization can be switched deterministically by voltage alone. Experimental evidence shows that although the bit does not rotate the full 90°, a unidirectional rotation of the bit towards a new easy axis occurs. In this

chapter it was shown that reducing the scale of the bit to the single domain regime lowered the magnetostatic and shape anisotropy energies and this was the key to magnetoelastic control.

In Chapter 6 the 90° rotation of a ring magnet was demonstrated. Unlike in single domain bits where only two stable magnetic configurations are possible, the ring magnetization can be rotated into an arbitrary in-plane direction. This is because the ring structure has low inherent shape anisotropy because of its radial symmetry and thus presents a lower barrier of energy for magnetoelastic rotation. The form of the domain wall depends on the annular width of the ring, with vortex domain walls forming in thicker rings and Neel walls forming in thinner rings. The mechanical strain causes vortex and Neel domain walls to rotate to align with the compressive stress direction, which is the new easy axis. The magnetization rotation is limited to 90° because this represents the largest possible angle between the initial magnetization and applied strain anisotropy. Future work will focus on achieving time-stepped magnetization rotation using patterned electrodes spaced radially around the ring structure with electric fields applied in-plane. This would enable both continuous (i.e. full 360° magnetization rotation) and also dynamic domain wall motion, a critical step toward understanding the magneto-mechanical interaction.

Chapter 7: LIST OF REFERENCES

[1] J.-M. Hu *et al*. N. Comms. **533** 1564 (2011)
[2] K.L. Wang *et al*. J. Phys. D: Appl. Phys. **46** 074003 (2013)
[3] J-G. Zhu, Proc. Of the IEEE **96**, 11 (2008)
[4] M. Liu, S. Li, O. Obi, J. Lou, S. Rand, and N. Sun, Appl. Phys. Lett. **98**, 222509 (2011)
[5] Y.-H. Chu, L. W. Martin, M.B. Holcomb, M. Gajek, S.-J. Han, Q. He, N. Balke, C.-H. Yang, D. Lee, W. Hu, P.-L. Yang, A. Fraile-Rodrigues, A. Scholl, S. X. Wang, and R. Ramesh, Nat. Mat. **7** 478-482 (2008)
[6] C. Annous and J. Gieraltowski, Euro. J. Phys. **29** 475 (2008)
[7] R. C. O'Handley, *Modern magnetic materials: principles and applications*. (John Wiley & Sons., New York, 2000)
[8] B. D. Cullity and C. D. Graham, *Introduction to Magnetic Materials*, 2nd ed. (Wiley-IEEE Press, 2008).
[9] A.E. Clark, J.P. Teter, and O.D. McMasters, J. Appl. Phys. **63**, 8 (1988)
[10] Y.M. Jia, S. W. Or, and H. L. Chan, Appl. Phys. Lett. **88**, 242902 (2006)
[11] F. Zavaliche, T. Zhao, H. Zheng, F. Straub, M.P. Cruz, P.L. Yang, D. Hao, and R. Ramesh, Nano letters, **7**, No. 6 1586-1590 (2007)
[12] H. Greve, E. Woltermann, H-J. Quenzer, B Wagner, and E. Quandt, Appl. Phys. Lett. **96**, 182501 (2010)
[13] Y. K. Fetisov, K.E. Kamentsev, D.V. Chashin, L.Y. Fetisov, and G. Srinivasan, J. Appl. Phys. **105**, 123918 (2009)
[14] S. Y. Chen, D. H. Wang, Z. D. Han, C. L. Zhang, Y. W. Du, and Z. G. Huang, Appl. Phys. Lett. **95**, 022501 (2009)
[15] G. Srinivasan, E.T. Rasmussen, J. Gallegos, R. Srinivasan, Yu. I. Bokhan, and V. M. Laletin. Phys. Rev. B. **64**, 214408 (2001)
[16] T. Wu, C.M. Chang, T.K. Chung, and G.P. Carman, IEEE Trans. Magnetics. **45**, 4333 (2009)
[17] C. Popov, H. Chang, P.M. Record, E. Abraham, R.W. Whatmore, Z. Huang, J. Electroceram. **20**, 53 (2008)
[18] Y.K. Fetisov and G. Srinivasan, Appl. Phys. Lett. **88**, 143503 (2006)
[19] J. Lou, M.Liu, D. Reed, Y. Ren, and N.X. Sun, Adv. Mat. 21, 4711 (2009)
[20] D. Pan, Y. Bai, J. Phys. D: Appl. Phys. **41**, No. 2 (2008)
[21] D. Pan, S. Zhang, J. Tian, Appl. Phys. A, **98**, 449-454 (2009)
[22] J.G. Wan, J.M. Liu, G.H. Wang, and C.W. Nan, Appl. Phys. Lett. **88**, 182502 (2006)
[23] Y.M. Jia, F.F. Wang, X.Y. Zhao, H.S Luo, S.W. Or, H.L.W. Chan, Elsevier Composites Sci. and Tech. **68**, 1440 (2007)
[24] T. Wu, T.K. Chung, C.M. Chang, S. Keller, and G.P. Carman, J. Appl. Phys. **106**, 054114 (2009)
[25] M. Moffett, J. of Amer. Soc. of Acoustics, **89,** 3 (1991)
[26] C.W. Nan. Phys. Rev. B **50**, 6082 (1994)
[27] J. Das, M. Li, S. S. Kalarickal, S. Altmannshofer, K. S. Buchanan, J. F. Li, and D. Viehland, Appl. Phys. Lett. 96, 222508 (2010).
[28] J. L. Hockel, T. Wu, and G.P. Carman, J. Appl. Phys. **109**, 064106 (2011)
[29] X. G. Zhao and D. G. Lord, J.of Appl. Phys. **83**, 7276-7278 (1998)
[30] Y.K. Fetisov and G. Srinivasan, Appl. Phys. Lett. 93, 033508 (2008)
[31] T. Wu, A. Bur, K. Wong, P. Zhao, C.S. Lynch, P.K. Amiri, K.L. Wang, and G.P. Carman, Appl. Phys. Lett. **98**, 01504 (2011)
[32] N. Tiercelin, Y. Dusch, A. Klimov, S.Giordano, V. Preobrazhensky, and P. Pernod, Appl. Phys. Lett. **99**, 192507 (2011)
[33] S. N. Piramanayagam, J. Appl. Phys. **102** (1), 011301-011322 (2007).
[34] J.-M. Hu, Z. Li, J. Wang and C. W. Nan, J. Appl. Phys. **107** (9), 093912-093910 (2010).

[35] G. Bochi, C. A. Ballentine, H. E. Inglefield, C. V. Thompson and R. C. O'Handley, PRL B **53** (4), R1729-R1732 (1996).
[36] H. J. Hug, B. Stiefel, A. Moser, I. Parashikov, A. Klicznik, D. Lipp, H. J. Guntherodt, G. Bochi, D. I. Paul and R. C. O'Handley, J. Appl. Phys.**79** (8), 5609-5614 (1996).
[37] S. Hameed, P. Talagala, R. Naik, L. E. Wenger, V. M. Naik and R. Proksch, PRL B **64** (18), 184406 (2001).
[38] M. A. Marioni, N. Pilet, T. V. Ashworth, R. C. O'Handley and H. J. Hug, PRL **97** (2), 027201 (2006).
[39] T.-K. Chung, G. P. Carman and K. P. Mohanchandra, Appl.Phys. Lett. **92** (11), 112509-112503 (2008).
[40] M. Fiebig, J. Phys. D: Appl. Phys. **38** (2005).
[41] W. Eerenstein, N. D. Mathur and J. F. Scott, Nature **442** (7104), 759-765 (2006).
[42] C.-W. Nan, M. I. Bichurin, S. Dong, D. Viehland and G. Srinivasan, J. Appl. Phys. **103** (3), 031101-031135 (2008).
[43] J. Ma, J. Hu, Z. Li and C.-W. Nan, Adv. Mat. **23** (9), 1062-1087 (2011).
[44] T. Wu, A. Bur, J. L. Hockel, W. Kin, C. Tien-Kan and G. P. Carman, Magn. Lett., IEEE **2**, 6000104-6000104 (2011).
[45] T. Wu, A. Bur, K. Wong, J. L. Hockel, C.-J. Hsu, H. K. D. Kim, K. L. Wang and G. P. Carman, J. Appl. Phys. **109** (7), 07D732 733 (2011).
[46] S. Geprags, A. Brandlmaier, M. Opel, R. Gross and S. T. B. Goennenwein, Appl. Phys. Lett. **96** (14), 142509-142503 (2010).
[47] A. Brandlmaier, S. Geprags, G. Woltersdorf, R. Gross and S. T. B. Goennenwein, J. Appl.Phys. **110** (4), 043913-043915 (2011).
[48] T. H. E. Lahtinen, J. O. Tuomi and S. van Dijken, Advanced Materials **23** (28), 3187-3191 (2011).
[49] J. J. Yang, Y. G. Zhao, H. F. Tian, L. B. Luo, H. Y. Zhang, Y. J. He and H. S. Luo, Appl. Phys.Lett. **94** (21), 212504-212503 (2009).
[50] S. Sahoo, S. Polisetty, C.-G. Duan, S. S. Jaswal, E. Y. Tsymbal and C. Binek, PRL B **76** (9), 092108 (2007).
[51] M. Liu, O. Obi, J. Lou, Y. Chen, Z. Cai, S. Stoute, M. Espanol, M. Lew, X. Situ, K. S. Ziemer, V. G. Harris and N. X. Sun, Adv. Func.Mat. **19** (11), 1826-1831 (2009).
[52] J. Lou, M. Liu, D. Reed, Y. Ren and N. X. Sun, Adv. Mat. **21** (46), 4711-4715 (2009).
[53] B. Zhang, J. Chen and G. M. Chow, Magnetics, IEEE Transactions on **47** (10), 4402-4404 (2011).
[54] C. Thiele, K. Dörr, O. Bilani, J. Rödel and L. Schultz, PRL B **75** (5), 054408 (2007).
[55] J.-M. Hu and C. W. Nan, Physical Review B **80** (22), 224416 (2009).
[56] N. A. Pertsev, Physical Review B **78** (21), 212102 (2008).
[57] T. Wu, M. Bao, A. Bur, H. K. D. Kim, K. P. Mohanchandra, C. S. Lynch and G. P. Carman, Appl. Phys. Lett. **99** (18), 182903-182903 (2011).
[58]J.-M. Hu, Z. Li, J. Wang, and C.W. Nan, J. Appl. Phys. **107**, 093912 (2010).
[59] J. Ma, J. Hu, Z. Li, and C.-E. Nan, Adv. Mater. **23**, 1062-1087 (2011).
[60] N. Lei, T. Devolder, G. Agnus, P. Aubert, L. Daniel, J.-V. Kim,W. Zhao, T. Trypiniotis, R. P. Cowburn, C. Chappert, D. Ravelosona1and P. Lecoeur, Nat. Comm. **4**, 1378 (2013).
[61]Y.-H. Chu, L. W. Martin, M. B. Holcomb, M. Gajek, S.-J. Han, Q. He, N. Balke, C.-H. Yang, D. Lee, W. Hu, Q. Zhan, P.-L. Yang, A. Fraile-Rodriguez, A. Scholl, S. X. Wang, and R. Ramesh. Nat. Mater. **7**, 478 (2008).
[62] T.-K. Chung, S. Keller, and G. P. Carman, Appl. Phys. Lett. **94**, 132501 (2009).
[63] J.M. Shaw, R. Geiss, and S. Russek, Appl. Phys. Lett. **89**, 212503 (2006).
[64] A. Chizhik, A. Stupakiewics, A. Maziewski, A. Zhukov, J. Gonzalez, and J.M. Blanco, Appl. Phys. Lett. **97**, 012502 (2010).
[65]C.-J. Hsu, J. L. Hockel, and G.P. Carman. Appl. Phys. Lett. **100**, 092902 (2012).
[66]T. H. E. Lahtinen, K. J. A. Franke, and S. van Dijkena, Sci. Rep. **2**, 258 (2012).
[67]N. Wu, Xi He, A. L. Wysocki, U. Lanke, T. Komesu, K. D. Belashchenko, C. Binek, and P. A. Dowben, Phys. Rev. Lett. **106**, 087202 (2011).

[68] S. Hameed, P. Talagala, R. Naik, L.E. Wenger, V.M. Naik, and R. Proksch, Phys. Rev. B **64**, 184406 (2001).
[69] J. N. Chapman and M. R. Scheinfein, **J**. Magn. Magn. **Mater. 200, 729 (1999)**
[70] T. Brintlinger, S.-H. Lin, K. H. Baloch, P. Alexander, Y. Qi, J. Barry, J. Melngaili, L. Salamanca-Riba, I. Takeuchi, and J. Cummings, Nano Lett. **10** 1219-1223 (2010).
[71] M.A. Schofield, M. Beleggia, Y. Zhu, G. Pozzi. Ultramicroscopy **108**, 7, 625-634 (2008).
[72] T. Wu, A. Bur, K. Wong, J. L. Hockel, C.-J. Hsu, H. K. D. Kim, K. L. Wang and G. P. Carman. J. Appl. Phys. **109**, 07D732 (2011).
[73]K.J. Harte, J. Appl. Phys.**39** 1503 (1968).
[74] R. C. Che, C. Y. Liang, X. He, H. H. Liu, and X. F. Duan, Sci. Technol. Adv. Mater. **12**, 025004 (2011)
[75] A. Aharoni, J. Appl. Phys. **83**, 6 (1998)
[76] J.A. Katine and E.E. Fullerton, J. Mag. And Mag. Mat. **320** 1217-1226 (2008)
[77]X. Chen, A. Hochstrat, P. Borisov, and W. Kleemann, Appl. Phys. Lett **89**, 202508 (2006)
[78] S. Mangin, D. Ravelosona, J.A. Katine, M.J. Carey, B.D. Terris and E.E. Fullerton, Nat. Mat. **5** 210-215 (2006)
[79] X. Liu, C. Ren, and G. Xiao, J. Appl. Phys. **92**, 8 (2002)
[80] E.C. Stoner and E.P. Wohlfarth, Philos. Trans. R. Soc. London, Ser. A **240**, 599 (1948)
[81] D. Braun, J. Mag. and Mag. Mat. **283** 1-7 (2004)
[82] Y. Zheng and J.-G. Zhu, J. Appl. Phys. **81** 8 (1997
[83] A. Bur, T. Wu, J. Hockel, C.-J. Hsu, H. K.D. Kim, T.-K. Chung, K. Wong, K.L. Wang and G.P. Carman, J. Appl. Phys. **109**, 123903 (2011)
[84] J.A. Osborn, Phys. Rev. **67**, 11 (1945)
[85] A. Aharoni, J. Appl. Phys. **30**, 4 (1959)
[86] A. Aharoni, J. Appl. Phys. **82**, 3 (1997)
[87] A. Aharoni, Phys. Rev. **119**, 1 (1960)
[88] S. Hoffman, Y. Tserkovnyak, P. K. Amiri, and K.L. Wang, Appl. Phys. Lett. **100**, 21 (2012)
[89] L.K. Lin, C.Y. Kuo, J.Y. Ou, C.C. Chang, C.R. Chang, L. Horng, and J.C. Wu, Phys. Stat. Sol. **4** 4360 (2007)
[90] M.-F. Lai, C.-R. Chang, J.C. Wu, Z.-H. Wei, J.H. Kuo, and J.-Y. Lai, IEEE Trans. on Mag. **38** 2550 (2002)
[91] Y.G. Yoo, M. Kläui, and C.A.F. Vaz, L.J. Heyderman, and J.A.C. Bland, Appl. Phys. Lett **82** 2470 (2003)
[92] K. Kondou, N. Ohshima, D. Chiba, S. Kasai, K. Kobayashi, and T. Ono, J. Phys. Condens. Matter **24** 024217 (2012)
[93] Y.-S. Choi, J.-Y. Lee, M.-W. Yoo, K.-S. Lee, K.Y. Guslienko, and S.-K. Kim, Phys. Rev. B **80,** 012402 (2009)
[94] J. Rhensius, L. Heyne, D. Backes, S. Krzyk, L. J. Heyderman, L. Joly, F. Nolting, and M. Kläui, Phys. Rev. Lett. **104**, 067201 (2010)
[95] M. Kläui J. Phys. Condens. Matter **20** 313001 (2008)
[96] J.-Y. Lee, K.-S. Lee, S. Choi, K. Y. Guslienko, and S.-K. Kim, Phys. Rev. Lett. B **76**, 184408 (2007)
[97] O. Boulle, G. Malinowski, and M. Kläui, Mat. Science and Engin. R **72** (2011)
[98] L. Heyne, J. Rhensius, A. Bising, S. Krzyk, P. Punke, M. Kläui, L.J. Heyderman, L. Le Guyader, and F. Nolting, Appl. Phys. Lett. **96**, 032504 (2010)
[99] M. Kläui, C.A.F. Vaz, J.A.C. Bland, W. Wernsdorfer, G. Faini, E. Cambril, L.J. Heyderman, F. Nolting, and U. Rüdiger, Phys. Rev. Lett. **94** 106601 (2005)
[100] M. Weisheit. S. Fähler, A. Marty, Y. Souche, C. Poinsignon, and D. Givord, Science **315**, 349 (2007)
[101] M. Kläui, J. Rothman, L. Lopez-Diaz, C.A.F Vaz, J.A.C. Bland, and Z Cui, Appl. Phys, Lett. **78,** 3268 (2001)
[102] C. Nam, B.G. Ng, F.J. Castano, M.D. Mascaro, and C.A. Ross, Appl. Phys. Lett **94**, 082501 (2009)

[103] G. Meier, M. Bolte, R. Eiselt, B. Krüger, D.H. Kim, and P. Fischer, Phys. Rev. Lett. **98**, 187202 (2007)
[104] J. Rothman, M. Kläui, L. Lopez-Diaz, C.A.F. Vaz, A. Bleloch, J.A.C. Bland, Z Cui, and R. Speaks, Phys. Rev. Lett. **86** 1098 (2001)
[105] F. Zavaliche, T. Zhao, H. Zheng, F. Straub, M. P. Cruz, P. L. Yang, D. Hao, and R. Ramesh, Nano. Lett. **7(6)**, 1586 (2007).
[106] J. Ryu, A. V. Carazo, K. Uchino, and H. Kim, J. Electroceram. **7** 24 (2001)
[107] T. Wu, A. Bur, K. Wong, J.L. Hockel, C.-J. Hsu, H. K.D. Kim, K. L. Wang, and G. P. Carman, J. Appl. Phys. **109**, 07D732 (2011)
[108] G. Liu, W. Jiang, J. Zhu, and W. Cao, Appl. Phys. Lett. **99**, 162901 (2011)
[109] M.H. Park, Y.K. Hong, B.C. Choi, M.J. Donahue, H. Han, and S.H. Gee, Phys. Rev. B **73**, 094424 (2006)
[110] J.L. Hockel, A. Bur, T. Wu, K.P. Wetzlar, and G.P. Carman, Appl. Phys. Lett. **100**, 022401 (2012)
[111] T. Wu, P. Zhao, M. Bao, A. Bur, J.L. Hockel, K. Wong, K.P. Mohanchandra, C.S. Lynch, and G.P. Carman, J. Appl. Phys. **109**, 124101 (2011)